



Universität Hamburg

DER FORSCHUNG | DER LEHRE | DER BILDUNG

**Self-assembly and topological superconductivity
in antiferromagnetic ultra-thin films
studied by SP-STM**

DISSERTATION ZUR ERLANGUNG DES DOKTORGRADES
AN DER FAKULTÄT FÜR MATHEMATIK, INFORMATIK UND NATURWISSENSCHAFTEN
FACHBEREICH PHYSIK DER UNIVERSITÄT HAMBURG

VORGELEGT VON

Arturo Rodríguez Sota

geboren am 19.04.1998

Hamburg

May 15, 2025

Gutachter/innen der Dissertation:

PD Dr. Kirsten von Bergmann Prof. Dr. Roland Wiesendanger

Zusammensetzung der Prüfungskommission:

Prof. Dr. Daniela Pfannkuche
PD Dr. Kirsten von Bergmann
Prof. Dr. Roland Wiesendanger
Prof. Dr. Roberto Lo Conte
Prof. Dr. Guido Meier

Vorsitzender der Prüfungskommission: Prof. Dr. Daniela Pfannkuche

Datum der Disputation: 09.07.2025

Vorsitzender des Fach-Promotionsausschusses PHYSIK: Prof. Dr. Wolfgang J. Parak

Leiter des Fachbereichs PHYSIK: Prof. Dr. Markus Drescher

Dekan der Fakultät MIN: Prof. Dr.-Ing. Norbert Ritter

" Caminante, son tus huellas
el camino, y nada más;
caminante, no hay camino:
se hace camino al andar.
Al andar se hace camino,
y al volver la vista atrás
se ve la senda que nunca
se ha de volver a pisar.
Caminante, no hay camino,
sino estelas en la mar."

— Antonio Machado, Proverbios y
cantares

Abstract

Antiferromagnetic (AFM) materials are a promising platform for new generations of ultra-fast, low energy, robust data storage and computing systems. Their combination with different substrate symmetries and properties leads to a plethora of interesting phenomena such as multi-Q states [1], [2], frustrated antiferromagnetism [3], [4] or topological nodal point superconductivity (TNPSC) [5], [6]. However, the atomic scale magnetic ordering makes their study challenging for most microscopic techniques.

In this thesis I use the spin-polarized scanning tunneling microscopy (SP-STM)[7] technique to characterize the properties of AFM ultra-thin layers on substrates with different structural and superconducting properties.

In the first part, the growth and magnetism of the phases in the first monolayer of Mn on Ir(111) are studied. In this system a cluster phase and reconstructed phase coexist in the sub-monolayer regime until the coverage reaches one monolayer, when the structure becomes pseudomorphic. The magnetic state of the reconstructed and pseudomorphic phases is the Néel state.

In the second part, the growth, magnetism and superconductivity of Cr/Nb(110) is studied. The first layer of Cr grows pseudomorphically, the second one goes through several phases with increasing density, and the third one reaches the Cr bulk lattice constant. Regarding magnetism, just the first layer displays magnetic properties. Its magnetic ground state is the $c(2 \times 2)$ AFM state. Small strips of the first layer and the whole second layer do not develop magnetic properties such as in-gap states or magnetic order. The study of the first Cr layer on superconducting Nb(110) results in its characterization as a TNPSC.

Zusammenfassung

Antiferromagnetische (AFM) Materialien sind eine vielversprechende Plattform für neue Generationen von ultraschnellen, energieeffizienten und robusten Datenspeicher- und Rechensystemen. Ihre Kombination mit unterschiedlichen Substratsymmetrien und -eigenschaften führt zu einer Vielzahl interessanter Phänomene, wie beispielsweise Multi-Q-Zustände [1], [2], frustrierter Antiferromagnetismus [3], [4] oder topological nodal point superconductivity (TNPSC) [5], [6]. Allerdings stellt die atomare magnetische Ordnung eine Herausforderung für die meisten mikroskopischen Techniken dar.

In dieser Arbeit verwende ich die spin-polarisierte Rastertunnelmikroskopie (SP-STM) [7], um die Eigenschaften ultradünner AFM-Schichten auf Substraten mit unterschiedlichen strukturellen und supraleitenden Eigenschaften zu charakterisieren.

Im ersten Teil werden das Wachstum und der Magnetismus der Phasen in der ersten Monolage von Mn auf Ir(111) untersucht. In diesem System koexistieren eine Clusterphase und eine rekonstruierte Phase im Submonolagenbereich, bis die Bedeckung eine Monolage erreicht; dann wird die Struktur pseudomorph. Der magnetische Zustand der rekonstruierten und pseudomorphen Phasen ist der Néel-Zustand.

Im zweiten Teil werden das Wachstum, der Magnetismus und die Supraleitung von Cr/Nb(110) untersucht. Die erste Lage von Cr wächst pseudomorph, die zweite durchläuft mit zunehmender Dichte mehrere Phasen, und die dritte erreicht die Gitterkonstante von Cr im Volumen. Bezüglich des Magnetismus zeigt nur die erste Lage magnetische Eigenschaften. Ihr magnetischer Grundzustand ist der $c(2 \times 2)$ AFM-Zustand. Kleine Streifen der ersten Lage und die gesamte zweite Lage entwickeln keine magnetischen Eigenschaften wie In-Gap-Zustände oder magnetische Ordnung. Die Untersuchung der ersten Cr Lage auf supraleitendem Nb(110) führt zu ihrer Charakterisierung als TNPSC.

Contents

1	Introduction	11
2	Theoretical background	13
2.1	Scanning Tunneling Microscopy	13
2.1.1	Spin-polarized STM	15
2.1.2	Measurement modes	16
2.2	Magnetic interactions at the atomic scale in ultra-thin layers	19
2.2.1	Heisenberg exchange	19
2.2.2	Magnetic anisotropy	22
2.3	Topology in condensed matter physics	23
2.3.1	Topological classification of gapped quantum systems: The quantum dot	24
2.4	Superconductivity	26
2.4.1	BCS theory and DOS around E_F	27
2.4.2	Type-I and type-II superconductor classification	27
2.4.3	Topological nodal-point superconductivity	29
2.4.4	Superconductivity and magnetism: Yu-Shiba-Rusinov states	29
3	Methods	31
3.1	Experimental setup	31
3.2	Sample preparation	32
3.2.1	Manganese on iridium	33
3.2.2	Chromium on niobium	33
3.3	Frequently used analysis techniques	34
3.3.1	Moiré patterns	34
3.3.2	Two dimensional fast Fourier Transforms	39
4	Growth and magnetism of first layer Mn/Ir(111)	45
4.1	Introduction	45
4.2	Mn/Ir(111): Three structural phases	46
4.3	Measurement temperature differences	47
4.4	Mn pseudomorphic phase	49
4.4.1	Structure of the pseudomorphic phase	49
4.4.2	Magnetism of the pseudomorphic phase	50
4.5	Mn reconstructed phase	51
4.5.1	Structure of the reconstructed phase	52
4.5.2	Magnetism of the reconstructed phase	53

4.6	Mn cluster phase	56
4.6.1	Cluster types and behavior	57
4.6.2	Cluster density and distribution	62
4.6.3	Cluster orientation	65
4.6.4	Cluster structure	66
4.6.5	Cluster magnetism	71
4.7	Low coverage sample: Proto-islands	72
4.8	Mn/Ir(111) conclusions	75
5	Growth, magnetism and superconductivity of Cr/Nb(110)	77
5.1	Introduction	77
5.2	Cr/Nb(110): Growth and structural analysis	78
5.2.1	Cr first layer	78
5.2.2	Cr second layer	80
5.2.3	Cr third layer	85
5.3	Cr/Nb(110): Magnetism and superconductivity	87
5.3.1	Cr extended first layer	87
5.3.2	Cr <i>worms</i>	94
5.3.3	Cr second layer	102
5.4	Cr/Nb(110) conclusions and outlook	107
6	Appendix A: Further considerations about the growth of Cr/Nb(110)	109
6.1	Cr second layer: intermediate growth phases	109
6.1.1	Train track adatom phase	109
6.1.2	Absorbed train track reconstruction	111
6.1.3	Music box adatom phase	112
6.2	Cr growth: holistic structure model	114
7	Summary and outlook	117
	Bibliography	119
	List of publications	124
	Acknowledgments	127

1 Introduction

" A PhD is a doctorate. It's literally describing a doctor. [...]
The problem here is that medical practitioners have co-opted the word "doctor". [...]
I know we live in a world where anything can mean anything, and nobody even cares about etymology!"

— Captain Raymond Holt, Brooklyn
Nine Nine

Rapid advances in modern technology have been largely fueled by enhancements in computing power, data storage, and communication systems. However, conventional electronics approach their physical limits and new paradigms are required to continue progress in information technology. One of the main challenges for traditional silicon-based computing is the increasing energy consumption. Another significant challenge is the data retention time of traditional memory storage. Magnetic-based solutions, including spintronic devices, have been proposed as alternatives. Ferromagnetic (FM) materials are already used in spintronic applications, but they face scalability issues due to their sensitivity to external magnetic fields and their stray field interactions [8]. Antiferromagnetic (AFM) materials present a promising solution to these limitations. They exhibit no macroscopic magnetization, which makes them highly resistant to external magnetic perturbations. This results in AFM-based devices not having the same limitations as the FM-based ones. Additionally, they operate in the terahertz regime, compared to the gigahertz range of FM materials, making AFM-based devices a great contestant for high-speed, low-power applications [9], [10], [11]. Another path towards low energy, non-volatile technologies is topological superconductivity. In these materials, the energy efficiency comes from the non-dissipative transport that characterize superconducting materials. The information robustness is realized via the topological protection that these systems can provide to their states. The combination of superconductivity and topology can also give rise to exotic quasiparticles known as Majorana bound states, which are considered to be key building blocks for scalable quantum computers. A way to realize these topological superconductors is via magnet-superconductor hybrid systems (MSHs) [12]. A particular case are AFM materials in proximity to superconductors, potentially obtaining both the benefits of antiferromagnets and topological superconductors [5].

The structure of the AFM materials is a key factor determining the AFM ordering at the nanoscale, and therefore its potential final applications. When an ultra-thin film of AFM material is grown on a substrate, the interplay between the layers determines the final atomic configuration. This can give rise to complex spin textures such as the 120° Néel state [13] or different multi-Q spin configurations [1]. These magnetic states can then interfere with other phenomena such as superconductivity, generating the mentioned topologically protected states. To study all these phenomena, an invaluable tool is spin-polarized scanning tunneling microscopy (SP-STM) [7], which allows the direct investigation of AFM systems with magnetic resolution at the atomic scale. Alongside this technique, scanning tunneling spectroscopy (STS) permits the study of the superconducting properties of the systems.

In this thesis I report on the structural, magnetic and superconducting (when applicable) properties of two AFM ultra-thin layer systems studied via SP-STM and STS. In both systems different structural phases are observed and characterized. The magnetic ground states have also been characterized, and their evolution through the different structural phases is also discussed. In chapter 2 I discuss briefly the main interactions present in magnetic ultra-thin films and I introduce the theoretical frame for later chapters. In chapter 3 I comment on the experimental techniques that have been used during the thesis along with some particularly recurrent analysis techniques. In chapter 4 I explore the three different structural phases exhibited by a monolayer of Mn/Ir(111) and develop atomistic models for all of them. The magnetic ground states of two of these phases are characterized, while for the third one different possibilities are proposed. In chapter 5 I report the presence of the topological nodal point superconducting (TNPSC) phase in the first layer of Cr/Nb(110). In this system, the main structures of the first, second and third layers are characterized. The system's different structures result in frustrated and non-frustrated magnetic orderings, which in turn influence the topological characteristics of the layers. In the appendix (6) I discuss in detail the intermediate growth phases of the second layer of Cr/Nb(110). Finally, in the summary and outlook (7) I summarize the results of the thesis as a whole and I propose further studies for these systems.

2 Theoretical background

"People think of education as something they can finish."

— Isaac Asimov

In this chapter I will introduce basic theoretical concepts which are necessary to interpret the experimental results in the following chapters. I will start discussing the scanning tunneling microscopy (STM) technique, and in particular spin-polarized scanning tunneling microscopy (SP-STM). I will continue discussing the magnetic interactions that play a role in the magnetism observed in the studied systems. Then I will focus on the topology in condensed matter physics as a way to characterize gapped systems. Finally, I will discuss superconductivity and magnet-superconductor hybrid systems.

2.1 Scanning Tunneling Microscopy

Scanning tunneling microscopy [14], [15] is a scanning probe microscopy technique that uses the quantum tunneling effect to characterize electrically conducting surfaces in real space with sub-nanometer resolution. In an STM, the electron tunneling takes place between two electrodes called *tip* and *sample* separated by a potential barrier consisting of a vacuum gap of a few hundreds of picometers. When a bias voltage V on the order of mV to several V is applied between tip and sample, a current on the order of pA to nA flows through the vacuum barrier. The tunnelling current between electrodes decays exponentially with the distance between them, allowing for a precise measurement of the tip-sample distance [7]. This decay has the form of:

$$I \propto e^{-2\kappa d} \quad (2.1)$$

where d is the distance between tip and sample and κ is the inverse decay length.

The movement of the tip through piezoelectric elements in three dimensions allows for the topographic characterization of the sample in a scanning fashion thanks to the high sensitivity of the tunneling current on the tip-sample distance. This can be achieved using different measurement modes such as the ones explained in section 2.1.2. The resolution in the XY plane is given by the sharpness of the apex of the tip. Ideally, it is

a single atom tip, allowing for sub-atomic resolution due to the fast decay of the wave function.

To model the current between tip and sample when a voltage is applied, it is assumed that the eigenstates of both electrodes are solutions of the Schrödinger equations for the non-interacting case. It is also assumed that these eigenstates are coupled at the tunneling junction. Then, the probability for an electron to go from a tip state to a sample state can be calculated with Fermi's golden rule, and the matrix elements via the perturbative approach [16]. If we then model the tip as an s-orbital [17], the tunneling current is given by:

$$I(V, T) = \frac{4\pi e}{\hbar} \int_{-\infty}^{\infty} \rho_s(E - E_F) \rho_t(E - E_F + eV) \cdot [f(E - E_F + eV, T) - f(E - E_F, T)] dE \quad (2.2)$$

Here ρ_t is the density of states of the tip at the apex, and ρ_s is the local density of states (LDOS) at the tip location. V is the bias voltage and f is the Fermi-Dirac distribution that describes the population of states due to thermal excitations:

$$f(E, T) = \frac{1}{1 + e^{E/kT}} \quad (2.3)$$

The tunneling process is represented schematically in Fig. 2.1.

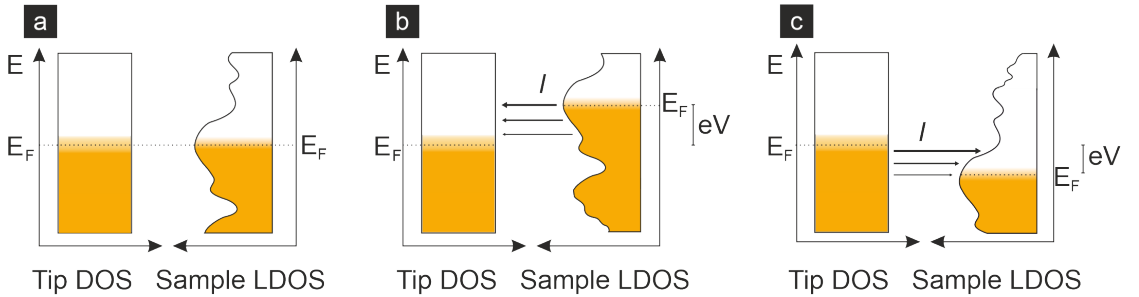


Figure 2.1: Schematic tip-sample tunneling junction. (a) Tip-sample DOS with $V = 0$. Both Fermi levels are aligned. (b) Tip-sample DOS with $V < 0$. The sample's Fermi level has now been shifted up with respect to the tip's. The electrons can now tunnel to the unoccupied states in the tip. (c) Tip-sample DOS with $V > 0$. The sample's Fermi level has now been shifted down with respect to the tip's. The electrons can now tunnel to the unoccupied states in the sample.

If ρ_t is independent of the energy around E_F , at very low temperatures ($T \approx 0K$) equa-

tion 2.2 can be written as:

$$I(V) \propto \int_{E_F}^{E_F+eV} \rho_s(E) dE \quad (2.4)$$

This reveals that the tunneling current is approximately proportional to the integrated vacuum density of states of the sample at the tip's location.

2.1.1 Spin-polarized STM

SP-STM [18] is a STM technique that enables the study of magnetic structures at the atomic scale. The technique uses magnetic electrodes for both tip and sample. The tunneling magnetoresistance (TMR) effect [19], allow us to obtain information about the magnetic structure of the sample.

The TMR effect distinguishes between differently polarized electrons when tunneling. This can be modeled as an extra component in the tunneling current: I_{SP} , the spin polarized component. This component is dependent on both tip and sample polarizations, P_t and P_s , and the angle between their magnetizations θ like [20]:

$$I_{SP} = I_0 P_t P_s \cos(\theta) \quad (2.5)$$

where the polarization of the tip and the sample are:

$$P_t = \frac{n_t^\uparrow - n_t^\downarrow}{n_t^\uparrow + n_t^\downarrow} \quad (2.6)$$

$$P_s = \frac{n_s^\uparrow - n_s^\downarrow}{n_s^\uparrow + n_s^\downarrow} \quad (2.7)$$

Here $n_{s,t}^{\uparrow\downarrow}$ are the spin-resolved densities of states. In other words, P_t and P_s are proportional to the difference between n^\uparrow and n^\downarrow states in a given electrode. When n^\uparrow and n^\downarrow are equal, i.e. in a non-magnetic material, the polarization is zero.

Then, the overall tunneling current can be modeled as the sum of a spin-averaged and a spin-polarized component [20]:

$$I = I_0 + I_{SP} = I_0(1 + P_t P_s \cos(\theta)) \quad (2.8)$$

This shows how the maximum and minimum values for I_{SP} occur when $\theta = 0^\circ$, and $\theta = 180^\circ$. Depending on the signs of the polarization of tip P_t and sample P_s , the maximum I_{SP} can appear for both $\theta = 0^\circ$ or $\theta = 180^\circ$: When the polarizations are both positive or negative, the maximum spin polarized current occurs for parallel magnetic moments. When the polarizations have different signs, the maximum current occurs when the magnetic moments are antiparallel.

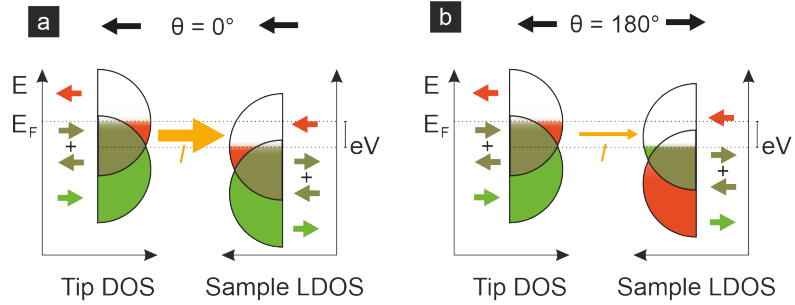


Figure 2.2: Schematic spin polarized current tunneling for different magnetization angles between electrodes. (a) DOS of tip and sample when $\theta = 0^\circ$. The yellow arrow represents the current flowing between electrodes. **(b)** DOS of tip and sample when $\theta = 180^\circ$.

In Fig. 2.2 a schematic representation of the spin polarized tunneling is represented for different θ values. The current is represented by the yellow lines always flowing from tip to sample. The decrease in current I when θ is 180° is represented by the smaller thickness of the yellow arrow.

This results in a way to use the TMR to image magnetic textures.

2.1.2 Measurement modes

STM is a versatile technique with which different types of experiments can be performed. The most characteristic ones used in this work are explained next.

Constant-current mode

This is the main stabilization mode of the STM, and the one used for recording most of the images presented in this work. In this mode, scanning with the tip over the surface is done while keeping a constant current flow between electrodes. The current is dependent on the distance between electrodes and the LDOS at the tip position, as shown in eq. 2.1 and eq. 2.4 respectively. This means that when the tip is moved from a position to another one in the XY plane, if the tip-sample distance or the LDOS change, the STM will have to modify a parameter to keep the same current flow. This parameter is the tip height, which is regulated through a feedback loop to keep the current constant. So for example, if the tip is moved from one location to another one where the current is reduced, the tip will approach the sample to increase the measured current to the setpoint value. In this mode, the topographic maps are generated by the movement of the tip in the three-dimensional space. Constant-current images contain structural, electronic and magnetic information.

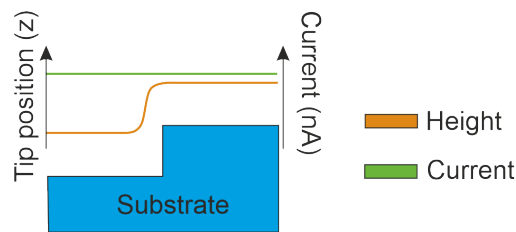


Figure 2.3: Constant-current measurement schematic. When the tip-sample distance changes, the tip follows the contour keeping the current constant.

Constant-height mode

In this mode the tip is scanned at constant-height while the tunnel current is recorded. This leads to current changes when moving along the XY plane depending on the topography of the sample and the LDOS. This measurement mode is particularly useful when studying atomically flat surfaces to avoid artifacts created by the feedback loop of the constant-current mode. On the other hand, it becomes unreliable when working with step edges, as the resolution is lost in the lower layers when the tip-sample distance increases. Furthermore, there is a possibility of crashing the tip against the surface if there are higher step edges, or due to thermal drift.

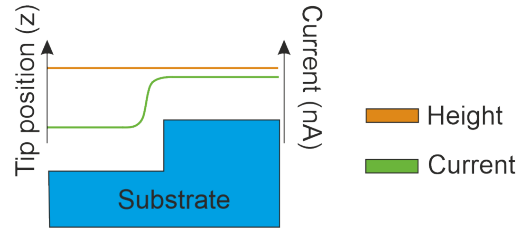


Figure 2.4: Constant-height schematic. The tip is not moved in the out-of-plane direction, so when the tip-sample distance changes, the current changes with it.

Differential conductance maps

With the help of a lock-in amplifier it is possible to obtain differential conductance (dI/dU) maps of the surface while scanning the sample. This is achieved adding an alternating current (AC) modulation on the order of kHz to the DC bias voltage between tip and sample. The typical amplitude of said modulation is around 10% of the bias voltage. The dI/dU signal can be interpreted as the LDOS of the system around the selected bias voltage energy (this can be seen in eq. 2.3). The spatial LDOS variations on the surface of the sample can be caused by structural, electronic or magnetic phenomena. The dI/dU maps allow us to characterize these different regions in real space in a fast and precise way.

Multipass mode

In multipass mode lines are scanned more than once with different parameters to obtain different information. The first scan is in constant-current mode, recording the topography of the surface. After that, the measurement parameters are changed, and the tip follows the previously recorded topographic profile with the new parameters. This is useful to measure with very low energies, including $U = 0$ mV, without crashing the tip into the sample. This measurement mode can be used to obtain data at low bias voltages for different structures or terraces. On the other hand, the recorded path in the first pass may lead to artifacts in the second pass that are not supposed to be there at the new applied parameters.

Scanning tunnelling spectroscopy and spatially resolved spectroscopy maps

In the same way that a differential conductance map obtains information of the sample at a given energy for different locations, the scanning tunnelling spectroscopy (STS)

mode obtains information at a given location for different energies. During these measurements the tip is kept at the same position and the applied voltage between tip and sample is swept while recording the current. That way, a $I(u)$ spectrum is acquired. These spectra are proportional to the energy resolved LDOS of the sample at the tip position. The comparison of different spectra at different positions can reveal characteristic features of the sample in those positions.

If STS data are taken along a two-dimensional grid in real space, a spatially resolved spectroscopy map is obtained. This map is the combination of a differential conductance map and STS, and includes the information of both of these measurements together, providing a complete set of data. Some of the problems with these measurements are the long time they take and their lack of high resolution in either space or energy to make them affordable time-wise. Usually they are substituted by high spatial resolution images and high energy resolution STS measurements on the interesting points. Still, the spatially resolved spectroscopy maps can be useful to identify places on a surface to study in more detail if time is available. A particular case is the line-spectroscopy map. Here the STS measurements are taken along a line instead of taking them on a two-dimensional grid.

2.2 Magnetic interactions at the atomic scale in ultra-thin layers

In this section I will discuss the magnetic interactions at the atomic scale that play a role in determining the magnetic ground state of the studied ultra-thin layers. These are mainly two: Heisenberg exchange and magnetic anisotropy.

The Heisenberg exchange interaction determines if neighboring atoms are oriented parallel or antiparallel to each other, but does not give information about this direction with respect to the crystal. Magnetic anisotropy, on the other hand, describes how different directions along a crystal may be preferred for the spins of the atoms to align with, but does not depend on their relative orientation.

I will start discussing the Heisenberg exchange.

2.2.1 Heisenberg exchange

The Heisenberg exchange interaction mediates between magnetic atoms determining the resulting magnetic order. It has its roots in the Coulomb interactions between charges and Pauli's exclusion principle. If we consider a two electron system, Pauli's

principle dictates that the overall wave function has to be antisymmetric. This means that in the case of a symmetric spatial part of the wave function, the spin wave function must be an antisymmetric singlet state ($S = 0$) or vice versa. If the spatial wave function is antisymmetric, the spin wave function must be a symmetric triplet state ($S = 1$). The difference in energy between the singlet state and the triplet state determines the strength and direction of the exchange interaction. This is encompassed in the exchange coefficient [21]:

$$J = \frac{E_S - E_T}{2} \quad (2.9)$$

where E_S is the energy of the singlet state and E_T is the energy of the triplet state. For $J \geq 0$, the energy of the singlet state is higher than the energy of the triplet state. This means that the triplet state is the ground state, and therefore the spin wave function is symmetric, i.e. the magnetic moments are aligned in a parallel (ferromagnetic) fashion. For $J \leq 0$ this is reversed, and the singlet state is the ground state. In this case the spin wave function is antisymmetric, i.e. the magnetic moments are aligned in an antiparallel (antiferromagnetic) fashion.

With J , the Hamiltonian of the Heisenberg model can be written like [21]:

$$\mathcal{H}_{exchange} = - \sum_{ij} J_{ij} \mathbf{S}_i \cdot \mathbf{S}_j \quad (2.10)$$

Here, J_{ij} is the exchange coefficient for two particular atoms in lattice sites i and j . The value of J decays rapidly with the distance, and usually nearest-neighbor interactions are enough to describe a system. These nearest-neighbor exchange coefficient is known as J_1 . The exchange coefficient for next-nearest-neighbors is called J_2 , then J_3 , etc. (see Fig. 2.6 (a)). The ratio between different J s gives rise to different magnetic ground states.

The Néel state: an SP-STM perspective

If we just consider an AFM J_1 for a system (this is $J_1 < 0$), the resulting state is known as the Néel state. This is a simple ground state in systems with square symmetry, as it gives rise to a checkerboard pattern of spins with nearest-neighbor-spins rotated 180° forming a $c(2 \times 2)$ AFM structure (Fig. 2.5 (a)). The Néel state has a different appearance in a hexagonal lattice though. In that case, a given spin cannot be antiparallel to all

its nearest-neighbors due to the symmetry of the system. This creates a magnetic frustration that is resolved by 120° spin rotations between adjacent spins, as can be seen in Fig. 2.5 (b). In that case, the Néel state is a magnetically frustrated state [3] [22] [23] [24].

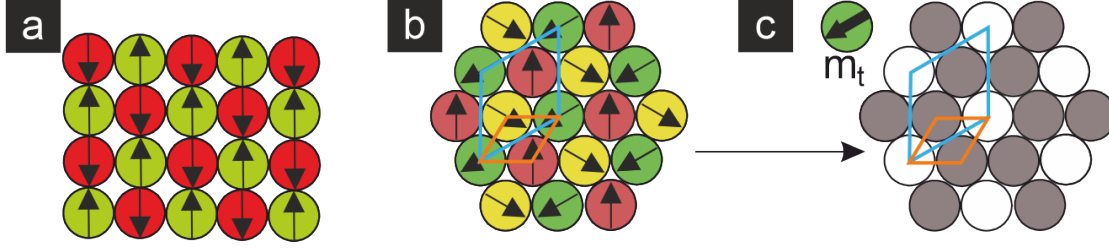


Figure 2.5: Néel state schematic. (a) Schematic showing the Néel state on a square lattice. The spins are all antiparallel to their nearest-neighbors. (b) Schematics showing the Néel state on a hexagonal lattice. The symmetry of the lattice makes it impossible for a spin to be antiparallel to all its nearest-neighbors. In orange the atomic unit cell is indicated, while in blue the Néel state magnetic unit cell is indicated. (c) Schematic representation of the appearance of (b) when measured by SP-STM with a tip magnetization oriented along the direction shown in the schematic. In this representation, white represents more current and black represents less current.

In Fig. 2.5 (b) it is shown how the hexagonal Néel state is formed by three hexagonal magnetic sublattices aligned in different directions (yellow, green and red). If an SP-STM measurement is done with a tip magnetized in the easy-plane of the surface, the differently aligned atoms will render different contrasts, such as in panel (c). This would result in a hexagonal lattice with a period larger than the atomic one, and rotated with respect to this one. Calculating the sizes and angles of the relative unit cells displayed in Fig. 2.5 (b) and (c), we can identify that the magnetic superstructure would be a $(\sqrt{3} \times \sqrt{3})R30^\circ$ structure.

The AFM row-wise state

If we include J_2 in a hexagonal antiferromagnetic system, the resulting state can be the antiferromagnetic row-wise (AFM-RW) state (see Fig. 2.6 (b)) depending on the ratio between J_1 and J_2 [1]. The AFM-RW state consists of rows of atoms with the spins oriented in an antiparallel way to each other. In this state most of the nearest-neighboring and the next-nearest-neighboring spins are antiparallel to the reference atom's spin.

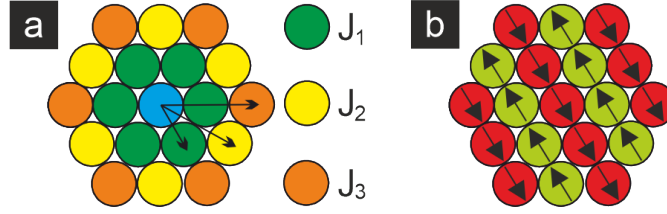


Figure 2.6: Different neighbor's exchange coefficients and AFM-RW state. (a) Schematic showing the first, second and third nearest-neighbors of an atom in a hexagonal lattice. Different colors indicate different neighbors and their exchange constants. (b) Schematics of the AFM-RW state.

2.2.2 Magnetic anisotropy

In solid state physics not all directions are equivalent, i.e. the space is not isotropic. The energy of the magnetization is dependent on its direction relative to the atomic lattice. This gives rise to directions along which it is energetically favorable for the magnetization to be aligned. These are called easy axes. There are several types of magnetic anisotropies, but for ultra-thin layers the most important is the surface anisotropy. This section will be mostly based on the book *Fundamentals of magnetism* by M. Getzlaff [25].

Surface anisotropy

The magneto-crystalline anisotropy is created by the spin-orbit coupling of the electrons. As the electrons live in orbitals that are dependent on the crystallographic structure, their spins align with these crystallographic axes or planes. This energy term tends to be smaller than the Heisenberg exchange term. Nevertheless, they do not usually compete with each other. This is because the Heisenberg term determines the relative (parallel or antiparallel) orientation of spins with respect to each other, while the magneto-crystalline anisotropy energy determines the easy axes for that orientation.

The surface anisotropy takes into account also the broken symmetry at interfaces. The absence of neighboring atoms on a surface can induce an easy-axis perpendicular to the surface. In this case, the effective anisotropy constant K_{eff} has a component representing the volume dependent magneto-crystalline anisotropy (K_V) and surface dependent magneto-crystalline anisotropy (K_S):

$$K_{eff} = K_V + 2K_S/d \quad (2.11)$$

Here d is the thickness of the system, and the factor two represents the existence of two surfaces. It is clear that when d grows, the surface contribution decreases, so this term will only be significant for (ultra-) thin layers, like the ones studied here.

The Hamiltonian for the energy has the form [21], [25]:

$$\mathcal{H}_{SMAE} = - \sum_i K_{eff} S_{i,z}^2 \quad (2.12)$$

Where K_{eff} is the effective anisotropy constant, $S_{i,z}^2$ represents the spin component along the surface normal. When K_{eff} is negative, the system displays an easy-plane anisotropy.

2.3 Topology in condensed matter physics

Topology is a branch of mathematics that studies the invariance of certain properties in a system under continuous deformations [26]. A classical example of one of these properties is the number of holes of a certain object. This number cannot be changed under continuous deformations, i.e. cannot be changed without cutting the object, piercing it, making it go through itself, etc. It is a topological invariant. The most well known example for this topological invariant is the donut/mug. These two objects are topologically equivalent regarding the number of holes, as they both have one. It is possible to say that they have a topological number of one, where the topological number is the topological invariant equal to the number of holes. This also makes them topologically distinct from a football, which has zero holes, i.e. its topological number is zero.

In condensed matter physics, topology has become a useful concept to understand and classify properties of the studied systems for some years [27]. This is applied to whole types of materials like the so called topological insulators [28], [29] and topological superconductors [30], [31]. But it can also be applied to particular structures such as magnetic skyrmions, which are said to be topologically protected [32]. In all these cases, the concept of *topological* usually refers to objects with different topological invariants. This topological difference gives rise to the concept of "*topological protection*", which means that mathematically it would be impossible to smoothly transform one into the other state and vice versa. What is understood as "smoothly" varies from case to case. Based on this definition, we can say that the donut/mug is topologically protected from becoming a football.

In condensed matter physics, the topological invariants are no longer the number of holes, but other quantities such as *topological quantum numbers* or *topological charge*. One subtype of topological quantum numbers in particular for two dimensional systems is the Chern number [27].

In real systems, objects such as skyrmions are not *absolutely* topologically protected. This occurs because the mathematical description is just a continuum approximation to these real systems [32].

I will now introduce the most general concept regarding the classification of gapped systems topologically as an example of the role of topology in condensed matter systems.

2.3.1 Topological classification of gapped quantum systems: The quantum dot

To distinguish two topologically distinct Hamiltonians, we must first define a topological quantum number, i.e. a topological invariant \mathcal{M} . We will consider that two Hamiltonians with an energy gap are topologically equivalent if they can be continuously transformed in each other without closing said gap during the transformation (this we consider a smooth transformation). Therefore, the topological invariant \mathcal{M} must be preserved while the gap remains, and change when the gap closes [28], [30]. The following discussion about the quantum dot is mostly based on [33].

The most simple example to discuss this classification is the case of a finite quantum system with discrete states. For that we consider a quantum dot described by a Hamiltonian H_1 . To transform H_1 into a second Hamiltonian H_2 we can model the transformation as [33]:

$$H(\alpha) = \alpha H_2 + (1 - \alpha) H_1 \quad (2.13)$$

So when $\alpha = 0$ we obtain the Hamiltonian H_1 , and when $\alpha = 1$ we get H_2 . This parameter α could represent an applied voltage in the sample.

A good invariant for this system is the number of completely full energy levels, \mathcal{N} . This occurs because the eigenvalues of gapped Hamiltonians can be freely moved as long as they do not cross zero energy, i.e. continuous transformations exist between Hamiltonians with the exact number of full energy levels below zero. When an energy level crosses zero energy, \mathcal{N} changes in the parameter space [31]. This is known as

a topological phase transition. When two Hamiltonians have different \mathcal{N} , they are separated by such transition, which means that it is necessary to close the gap to go from one to the other. This is shown in Fig. 2.7 (a) by the green-red line. This line aims to go from $(E = 0, \alpha = 0)$ to $(E = 0, \alpha = 1)$ without crossing any band. The color change represents a topological phase transition in the chosen path from one point to another. On the other hand, if the topological invariant \mathcal{N} does not change from the original Hamiltonian H_1 to the final one H_2 , there has to be a continuous transformation from one to the other one (Fig. 2.7 (b)). This occurs even if the invariant changes for certain intermediate α . In this case the path may need to vary from a straight line, like displayed in Fig. 2.7 (c).

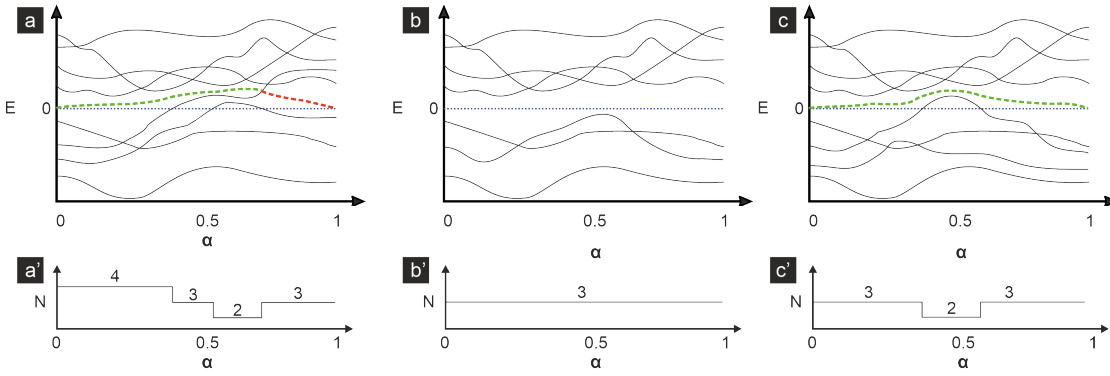


Figure 2.7: Schematic representation of invariant changes during Hamiltonian transformations. (a) Schematic representation of band structure in parameter space. The green-red line represents a path to go from $(0,0)$ to $(1,0)$. **a'** Invariant \mathcal{N} counter for panel (a). (b) Schematic representation of band structure in parameter space. **b'** Invariant \mathcal{N} counter for panel (b). (c) Schematic representation of band structure in parameter space. The green line represents a path to go from $(0,0)$ to $(1,0)$ without crossing any band. **c'** Invariant \mathcal{N} counter for panel (c).

This same concept can be applied for any system, but the invariant can be any other number. For example, for two dimensional systems, a possible invariant is the Chern number. A way to find out some characteristics of the invariant is using the Tenfold way [34]. This is a process that determines if the invariant of a Hamiltonian can just have one value ($\mathcal{N} \in 0$), a binary result ($\mathcal{N} \in \mathbb{Z}_2$), or an infinite amount of results ($\mathcal{N} \in \mathbb{Z}$). To do so, the method just requires the symmetries of the Hamiltonian and the spatial dimensions of the system. The Tenfold way is summarized in the following table 2.1 for systems with dimensions one to four.

Conventional superconducting materials (such as niobium) have time-reversal symmetry and particle-hole symmetry. This means that when combined with a magnetic material (no time-reversal symmetry), the system belongs to class D. In two dimensions, the invariant of the hybrid system also has an infinite amount of possible values.

Class	T	C	S	d=1	d=2	d=3	d=4
A	0	0	0	0	\mathbb{Z}	0	\mathbb{Z}
AIII	0	0	+1	\mathbb{Z}	0	\mathbb{Z}	0
AI	+1	0	0	0	0	0	\mathbb{Z}
BDI	+1	+1	+1	\mathbb{Z}	0	0	0
D	0	+1	0	\mathbb{Z}_2	\mathbb{Z}	0	0
DIII	-1	+1	+1	\mathbb{Z}_2	\mathbb{Z}_2	\mathbb{Z}	0
AII	-1	0	0	0	\mathbb{Z}_2	\mathbb{Z}_2	\mathbb{Z}
CII	-1	-1	+1	\mathbb{Z}	0	\mathbb{Z}_2	\mathbb{Z}_2
C	0	-1	0	0	\mathbb{Z}	0	\mathbb{Z}_2
CI	+1	-1	+1	0	0	\mathbb{Z}	0

Table 2.1: The Tenfold way classification with Time-Reversal (T), Particle-Hole (C), Chiral (S) symmetries for one-dimensional, two-dimensional, three-dimensional and four-dimensional systems. A value of +1 or -1 indicate the existence of the symmetry, while a value of 0 represents its absence.

In general, if two Hamiltonians \mathcal{H}_1 and \mathcal{H}_2 with different invariants \mathcal{M} and \mathcal{N} are put in contact, the gap *must* close at their interface. This indicates that boundary states exist inside the bulk gap, which is known as bulk-boundary correspondence. These boundary states are topologically protected, as they exist due to the interaction between two topological invariants, \mathcal{M} and \mathcal{N} , which are topologically protected themselves.

2.4 Superconductivity

Superconductivity is a phenomenon in which the electric resistance of a material drops to zero below a certain critical temperature T_c . Below this temperature, magnetic flux is expelled from the material in the so-called Meissner phase [35].

The energy gap opening in the superconducting state permits the topological characterization of superconducting systems via invariants, as discussed in 2.3.1. This makes superconducting systems an interesting platform for the appearance of topologically non-trivial phases and protected states.

2.4.1 BCS theory and DOS around E_F

The first fundamental superconductivity theory is the one proposed by J. Bardeen, L. N. Cooper and J. R. Schrieffer, the BCS theory [36]. In this theory, the charge carriers in the system are no longer individual electrons, but pairs of them, the so-called Cooper pairs. These electrons have opposite spins and momenta, and their mutual attraction is created by electron-phonon interactions. The existence of Cooper pairs leads to the appearance of a gap 2Δ in the density of states around the Fermi energy, where Δ is the minimal required energy to break a Cooper pair.

In the BCS theory, the ideal DOS of a sample around E_F can be described by [37]:

$$\frac{N(E)}{N_0} = \begin{cases} \frac{|E|}{\sqrt{E^2 - \Delta^2}} & \text{for } |E| > \Delta \\ 0 & \text{for } |E| < \Delta \end{cases} \quad (2.14)$$

where E is the energy, N_0 is the value of the DOS outside the gap, used to normalize the function, and Δ is half the gap width. The absence of states around E_F ($-\Delta < E < \Delta$) happens because of the necessity of a minimum energy (Δ) to break a Cooper pair. Also it is possible to see how sharp peaks appear at $E = \pm\Delta$, due to the equation's singularities. In real systems, these features are broadened. To describe this, a broadening parameter Γ is introduced. This allows us to re-write eq. 2.14 as [37]:

$$\frac{N(E)}{N_0} = \text{Re} \left[\frac{E - i\Gamma}{\sqrt{(E - i\Gamma)^2 - \Delta^2}} \right] \quad (2.15)$$

This equation is known as the Dynes function. Here, Γ broadens the peaks, reducing their height and filling the gap with states as shown in Fig. 2.8. This density of states around the Fermi energy can be measured by STS when sampling the LDOS.

2.4.2 Type-I and type-II superconductor classification

Before the BCS theory, the first phenomenological model describing superconductivity was proposed by Fritz and Heinz London [38]. From their model the penetration depth of a magnetic field in a superconductor can be obtained:

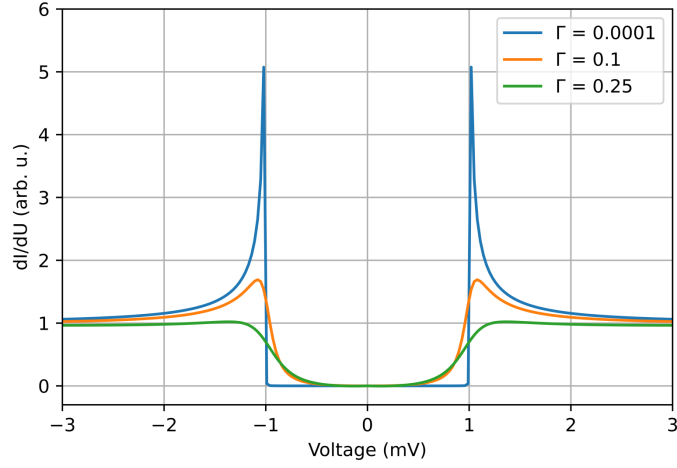


Figure 2.8: Normalized Dynes function for different Γ parameters and gap $\Delta = 1$.

$$\lambda_L = \sqrt{\frac{\mathbf{B}}{\nabla^2 \mathbf{B}}} = \sqrt{\frac{m}{\mu_0 n_s e^2}} \quad (2.16)$$

where \mathbf{B} is the magnetic field inside the superconductor, m is the mass of the electron, e is the electron charge, and n_s is related to the charge carrier density phenomenologically. This tells us that, in the scale of λ_L , magnetic fields are exponentially screened inside of superconductors.

If we consider ξ_0 as the coherence length in a superconductor, also viewed as the extension of a Cooper pair, we can characterize superconductors depending on which length, λ_L or ξ_0 dominates the system. It was found that the change in the properties of the superconductors occurs when the ratio $\kappa = \frac{\lambda_L}{\xi_0} = \frac{1}{\sqrt{2}}$ [39]. This ratio, which is roughly temperature-independent, allows distinguishing between type-I and type-II superconductors. Type-I superconductors are those with $\kappa < \frac{1}{\sqrt{2}}$, while type-II superconductors are those with $\kappa > \frac{1}{\sqrt{2}}$. In the case of type-I superconductors, when a critical field B_c is applied, the superconducting properties vanish. In contrast, type-II superconductors have two critical fields, B_{c1} and B_{c2} . When $B_{c1} < \mathbf{B} < B_{c2}$ normal-metallic regions in the shape of tubes known as vortices are able to cross the superconductor. These vortices arrange themselves in a hexagonal lattice called Abrikosov lattice with a lattice constant $d = 1.075 \sqrt{\frac{\phi_0}{B}}$, where B is the applied magnetic field, and ϕ is a single magnetic flux quantum. This phase occurs because for a certain range of applied fields, the formation of normal-superconducting interfaces is energetically favourable. Then, type-II

superconductors exhibit a second critical field, B_{c2} above which the superconducting properties completely disappear [40], [39].

In this thesis I used niobium, for which $\lambda_L = 39$ nm and $\xi_0 = 38$ nm, so $\kappa \approx 1.03$, i.e. Nb is a type-II superconductor. In fact, Nb is one of the only three elemental type-II superconductors along with vanadium and technetium [41], [42].

2.4.3 Topological nodal-point superconductivity

A particular type of superconductivity is topological nodal-point superconductivity (TNPS) [43]. This superconducting state occurs when the energy gap closes at certain k-vectors, but not along the whole k-space. This is a possible state for magnet-superconductor hybrid systems (MSHs). In these systems, the nodal-points have a topological charge that can be calculated. This can be used as a topological invariant to characterize the system. Low energy modes appear between nodal-points with different topological charges along certain directions (depending on the nodal-points). When the system is cut along these directions, for example with a step edge, the low energy modes can be observed via STM as edge states, i.e. available tunneling states appear along some edges at low energies, inside the gap. These low energy edge modes are topologically protected [5].

2.4.4 Superconductivity and magnetism: Yu-Shiba-Rusinov states

The theoretical study of single-atom magnetic impurities in proximity to s-wave superconductors was done by L. Yu, H. Shiba and A. Rusinov in the 1960s [44], [45], [46]. Their results revealed the existence of states inside the superconducting gap, $|E| < \Delta$, when magnetic impurities are present. These states are located at energies:

$$E(A,B) = \pm \Delta \frac{1 - A^2 + B^2}{\sqrt{(1 - A^2 + B^2)^2 + 4A^2}} \quad (2.17)$$

with particle weight

$$P(A,B) = \pm \Delta \frac{1 + (A + B)^2}{\sqrt{2 + (A + B)^2 + (A - B)^2}}. \quad (2.18)$$

where $A = \pi N_0 G$ and $B = \pi N_0 K$ are dimensionless parameters dependent on G , a magnetic scattering potential, K a nonmagnetic scattering term, and N_0 , the value of the DOS outside the gap.

These in-gap states are known as Yu-Shiba-Rusinov (YSR) states, and they appear when the Cooper pairs interact with the impurities via the magnetic exchange coupling, reducing the energy needed to break the pairs. Due to the particle-hole symmetry, these states appear in symmetric pairs around E_F . When $B = 0$, both positive and negative states exhibit the same weight. However, for a finite B , their intensity can be asymmetric. When A is strong, then the YSR states appear close to E_F . A can be so strong, that the YSR states are inverted, i.e. they change sign with each other. When this is the case the system is said to have experienced a quantum phase transition.

The spatial localization of the YSR states can be probed via STS. They are exponentially localized around the magnetic atom on the scale of the superconductor's coherence length ξ_0 . For short distances, the spatial localization is governed by a $(k_F \cdot r)^{-1}$ decay, where k_F is the isotropic Fermi wavevector. This has been proven experimentally, with a localization of YSR states within close distances from the magnetic atoms (~ 1 nm) [47],[48].

The symmetry of more complex orbitals, such as d-orbitals, can generate the appearance of different pairs of YSR states instead of just one even for a single magnetic impurity [49], [50]. In the case presented here the states arise from the existence of magnetic layers on the superconductor. This leads to the formation of YSR bands [51], [52].

3 Methods

"Longum iter est per praecepta, breve
et efficax per exempla"

— Seneca

In this section I will first describe the experimental setup used in this work. This will be continued by the preparation processes for the studied samples. I will finish discussing in more detail some repeatedly used analysis techniques in the work.

3.1 Experimental setup

The STM results displayed in this work were taken in two different ultra-high-vacuum (UHV) systems. All measurements above 100 K were done with a home-made variable-temperature (VT) STM, while the measurements at 80 K or lower were performed in a system with two home-made low-temperature (LT) microscopes equipped with superconducting magnets. Every microscope occupies one chamber in multi-chamber UHV systems. In the other chambers the sample preparation is done via Ar-ion-sputtering, annealing, and molecular beam epitaxy. Further analysis such as low energy electron diffraction (LEED) or Auger spectroscopy can also be done in these chambers. More detailed explanations of the sample preparations are given in the specific chapters.

A series of pumps and a bake-out are used to bring the systems to pressures on the order of $5 \cdot 10^{-11}$ mbar. This base pressure is required to obtain clean ultra-thin films via molecular beam epitaxy and to keep them clean for extended periods of time while the measurements are performed.

The two LT microscopes are able to achieve different lowest temperatures and to apply different out-of-plane magnetic fields. The first one can operate at 8 K with a liquid He cryostat and with an out-of-plane field up to 2.5 T via a superconducting magnet. The second microscope can operate at 4 K with a liquid He cryostat, and can be cooled down further to a temperature of roughly 1.3 K via a Joule-Thomson cycle. The upper limit for the applied out-of-plane magnetic field in this microscope is 9 T.

For the SP-STM and STS measurements, three different types of tips were used:

- Cr bulk tips.
- Fe coated W tips.

- Cr bulk tips with Nb clusters at the apex.

Cr bulk tips (Fig. 3.1 (a)) are antiferromagnetic tips with a varying spin orientation at the apex. The antiferromagnetic nature of Cr prevents the existence of a significant stray field. Gentle contact of the tip with the sample allows for the reorientation of the apex spin [53]. This makes this tip a polyvalent choice, as it can probe the spin orientation both out-of-plane and in-plane. It is also not affected by applied magnetic fields (up to the spin-flip transition, which is not accessible with this range of magnetic fields), which makes it particularly useful to probe ferromagnetic materials that can react to applied magnetic fields while the tip is magnetically stable. Still, this type of tip was used in this work also to study AFM materials.

The Fe coated W tips (Fig. 3.1 (b)) are used in the opposite cases. These tips are expected to have an in-plane magnetization due to shape anisotropy. The ferromagnetic properties of the Fe makes it to align with applied magnetic fields [54], in the case of our systems, out-of-plane. This makes Fe-coated W tips useful for probing antiferromagnetic materials that do not react to the applied field.

Cr bulk tips with Nb clusters at the apex (Fig. 3.1 (c)) are useful for STS measurements on superconductors [5],[55]. When performing STS with these tips, the convolution of the tip's DOS and the sample DOS widens the observed superconducting gap:

$$\Delta_{measured} = \Delta_{tip} + \Delta_{sample} \quad (3.1)$$

Increasing the size of the energy gap increases the energy resolution, which is beneficial for the characterization of in-gap features. However, this also creates a region inside the gap belonging to the tip gap, where thermal artifacts can appear.

3.2 Sample preparation

Here I will describe the sample preparation of the two main studied systems: Mn/Ir(111) and Cr/Nb(110). All these preparations are done inside the UHV systems described in section 3.1.

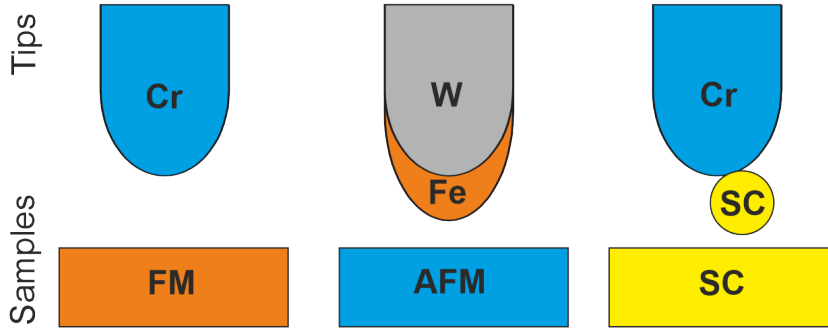


Figure 3.1: Schematic showing the STM tip types used in this thesis and the samples for which they are usually most useful. The colors represent different properties of the materials: Blue represents antiferromagnetic (AFM), orange represents ferromagnetic (FM), grey represents non magnetic, and yellow represents superconducting (SC) states.

3.2.1 Manganese on iridium

The Ir single crystal is first cleaned of any surface impurities or previously deposited layers via Ar-ion sputtering. To prepare an atomically-flat surface of the crystal, the sample is then annealed three times to about $T = 900$ K. Afterwards, the Mn is evaporated on the Ir crystal via molecular beam epitaxy (MBE). To do so, we use a Knudsen cell evaporator with a pyrolytic boron nitride crucible heated up to a temperature of $T = 963$ K. Different sample preparations were done regarding the temperature of the substrate when depositing Mn (from $T \approx 450$ K to $T = 300$ K) and the amount of Mn deposited (from 0.05 atomic layers to 1.2).

3.2.2 Chromium on niobium

Similar to the Ir single crystal, the Nb single crystal is first cleaned via Ar-ion sputtering. After that, the annealing is performed at a temperature of $T \approx 2700$ K, slightly below its melting point. The parameters to achieve this temperature are found following the work by Odobesko *et al* [56]. After obtaining a clean Nb surface, the Cr layer is deposited. For that we use a Knudsen cell evaporator with a pyrolytic boron nitride crucible heated up to a temperature of $T = 1398$ K. The different coverages studied range from 0.15 atomic layers to roughly 2 atomic layers. The Cr deposition is always done at substrate temperatures from $T \approx 450$ K to $T = 300$ K.

3.3 Frequently used analysis techniques

3.3.1 Moiré patterns

Moiré patterns are interference patterns generated when two or more gratings are superimposed. The Moiré pattern arises when the gratings are rotated, transposed, distorted or otherwise non-identical in general among themselves. Rotated Moiré patterns are often studied in solid state physics for well known systems like graphene double layers [57]. But the structures that I will discuss here are the Moiré patterns arising from lattice mismatches in metal-metal systems i.e. when one layer grows over another one with different lattice constant [58]. This nano-scale characterization can help to understand better these systems as a whole when atomic resolution is not available.

Here I will briefly discuss three types of lattice-mismatch Moiré patterns that are found in the systems studied in this work. I will also explain how to characterize mathematically the patterns and even obtain atomic information from them. The cases that I will describe here are:

- Anisotropic strain Moiré patterns
 - One-dimensional Moiré patterns
 - Bi- dimensional arbitrary strain Moiré patterns
- Isotropic strain Moiré patterns

Anisotropic strain Moiré patterns

Anisotropic strain Moiré patterns are those in which the distortion of the top layer with respect to the bottom one occurs differently along different crystallographic axes.

One-dimensional Moiré patterns

These Moiré patterns occur when the top layer is expanded or compressed with respect to the bottom layer in just one of the crystallographic directions. This leads to a beating pattern with a modulation along that direction. In essence, the atoms move from bridge sites to on-top sites and then back to bridge sites, as shown in Fig. 3.2 (a). The Moiré characterization of such a reconstruction uses the following formula:

$$d = \frac{p^2}{\delta p} \pm p \quad (3.2)$$

where d is the distance between two equivalent positions, p is the lattice constant of the first layer along the reconstruction direction, and δp is the difference between said distance and the lattice constant of the second layer along the same direction. If we solve for δp we can obtain the lattice constant of the top layer ($p \pm \delta p$) by measuring the Moiré pattern period (d) and knowing the atomic distance of the bottom layer in that direction (p):

$$\delta p = \frac{p^2}{d \pm p} \quad (3.3)$$

So for example, if we take two equal layers and compress the top one by 10%, like in Fig. 3.2 (a), we can apply the formula to recover the compression of said layer. In this case $p = 1$ if we normalize the distance of the bottom layer atoms along the horizontal direction. Now, if we count the atoms along the direction in which we have to move to recover the original position, we obtain $d = 9$. As the top layer is compressed, we have to add p to the denominator, which leads to $\delta p = 1/10$. Then, as it is a compression, the lattice constant in that direction is $p - \delta p = 1 - 0.1 = 0.9$, which is exactly the original 10% compression of the top layer.

Normally, the on-top positions are not preferred, and the top layer shifts along the direction perpendicular to the strain. This results in the atoms alternating between one three-fold hollow site to bridge sites to the other three-fold hollow site. The structural periodicity in this case is the same as for the non-shifted one (Fig. 3.2 (b) black lines). However, via STM, when the three-fold hollow sites are equivalent, they cannot be distinguished, effectively doubling the observed periodicity (Fig. 3.2 (b) black lines and dotted line). To account for that, eq. 3.3 becomes:

$$\delta p = \frac{p^2}{2d_m \pm p} \quad (3.4)$$

where d_m is the measured periodicity of the Moiré, which is half the value of d . This avoidance of the on-top positions is not possible in bi-dimensional Moiré patterns, so

just eq. 3.3 is needed.

Bi-dimensional arbitrary strain Moiré patterns

These Moiré patterns occur when the top layer is expanded or compressed with respect to the bottom layer along more than one crystallographic directions. This can be modeled as the superposition of two one-dimensional Moiré patterns propagating in perpendicular directions (see figure 3.2, where the top layer has been compressed by 20% along the vertical direction and 10% along the horizontal one). The one-dimensional Moiré patterns are just a particular case of those in which one of the strains is zero.

To characterize these systems, one just needs to perform the analysis shown for one-dimensional Moiré patterns but along perpendicular directions using eq. 3.3. It is interesting that another potentially useful quantity appears in these Moirés, and that is the angle between the reconstruction unit cell vectors θ_M :

$$\theta_M = \arctg\left(r \frac{c_x}{c_y}\right) \quad (3.5)$$

where c_y is the compression of the top layer along the Y axis and c_x along the X axis [59]; r is the ratio between bottom layer atomic distances along the X and Y directions. In the example of Fig. 3.2 (b), the structure refers to a hexagonal layer. This means that the distance between atoms in the Y ($[11\bar{2}]$) direction is $\sqrt{3}$ times larger than the distance along the X ($[1\bar{1}0]$) direction (so $r = \sqrt{3}$). Then $c_y = 0.2$ and $c_x = 0.1$. So finally $\theta_M \approx 41^\circ$ which is what we can see in Fig. 3.2 (b).

Isotropic strain Moiré patterns

Isotropic strain Moiré patterns are those in which the distortion of the top layer with respect to the bottom one is equivalent along different crystallographic axes. This means that the top layer is either compressed or expanded homogeneously. These Moiré patterns are a specific case of the bi-dimensional arbitrary strain Moiré patterns, in which the compression/expansion is the same for both axes. As such, they can be characterized again as a superposition of two one-dimensional Moiré patterns. In this particular case, the angle θ_M is the same along the different crystallographic directions, which means, that eq. 3.5 becomes:

$$\theta_{M_{iso}} = \arctg(r) \quad (3.6)$$

In the case of a hexagonal lattice, like in Fig. 3.2 (c), the ratio between atomic distances along the X and Y direction is $r = \sqrt{3}$. This gives $\theta_{M_{iso}} = 60^\circ$. So, as these Moiré patterns are just dependent on the bottom layer symmetry, the symmetry of the reconstruction will always be the same.

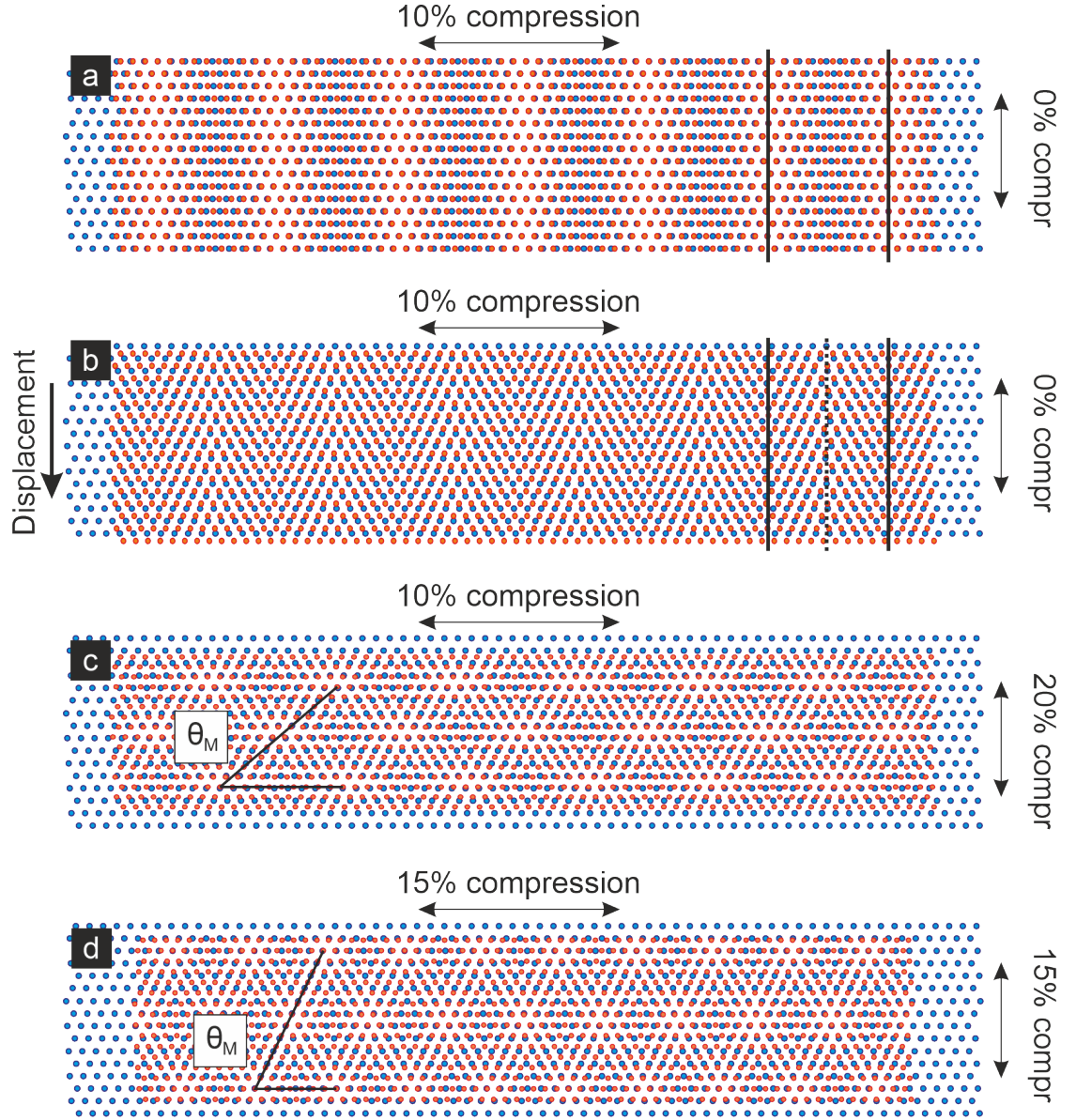


Figure 3.2: Different lattice-mismatch Moiré patterns. (a) Schematic showing a one-dimensional Moiré pattern over a hexagonal lattice created by a 10% compression along the X axis. (b) Schematic showing a one-dimensional Moiré pattern over a hexagonal lattice created by a 10% compression along the X axis and a shift of the layer along the Y axis. (c) Schematic showing an anisotropic bi-dimensional Moiré pattern over a hexagonal lattice created by a 10% compression along the X axis and a 20% compression along the Y axis. (d) Schematic showing an isotropic Moiré pattern over a hexagonal lattice created by a 15% compression along both X and Y axes.

3.3.2 Two dimensional fast Fourier Transforms

Two dimensional fast Fourier transforms (2D-FFT) are a versatile and useful analysis tool when analyzing 2D periodic structures. They are the two dimensional generalization of the fast Fourier transform algorithm.

Solving the discrete Fourier transform can be a time demanding problem that is circumvented via FFTs. FFTs are algorithms allowing for the fast computation of discrete Fourier transforms [60].

Once the problem can be solved in one dimension (one array of data), the generalization to two dimensions is the simple repetition of the one dimensional case along the different directions of an image.

We can understand an STM image as a matrix of points where each pixel is an element in the matrix with a value. In that case, it is possible to perform 1D-FFTs along each of the rows and columns of the matrix. This way we obtain information of the frequencies present at said row or column. If we do this along the x and y axes, we obtain a two dimensional map revealing the frequencies present in the original image (see Fig. 3.3). In this map, low frequencies ($k = 0$) are located in the center of the frame, and the furthest a point is from the center, the higher the frequency it represents (compare Fig. 3.3 (a) and (b)). As frequencies are the same from left to right and right to left, peaks are symmetric with respect to the center of the image, and the line crossing through both peaks and the center is perpendicular to the real-space direction of the lines.

STM analysis via 2D-FFT

The 2D-FFT peaks' distance to the center and their relative orientation with respect to the crystallographic directions of the sample deliver information about the studied structure. To obtain the real space distances between lines, i.e. the period, from the 2D-FFT, the following equation is used:

$$p = \frac{2}{k_{p2p}} \quad (3.7)$$

where p is the period between lines in real space, and k_{p2p} is the measured distance between the two peaks in the 2D-FFT in units of $distance^{-1}$. The factor of two results from taking the peak-to-peak value for k .

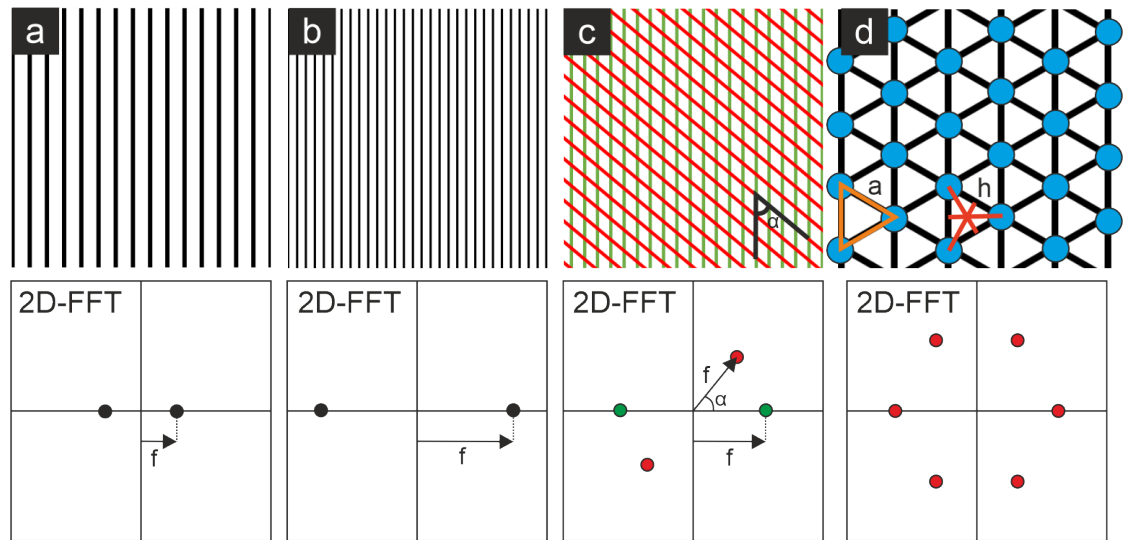


Figure 3.3: Schematics showing 2D-FFT properties. (a) Schematic representation of an image with a periodic structure with a certain frequency and its schematic 2D-FFT below. (b) Schematic representation of an image with a periodic structure with higher frequency than (a) and its schematic 2D-FFT below. (c) Schematic representation of an image with two periodic structures with different frequencies and along different directions, and its schematic 2D-FFT below. (d) Schematic representation of a hexagonal atomic lattice indicating the atom-atom distances in orange and the line-line distance in red. The 2D-FFT displays the peaks between lines, not atoms.

The peaks of the 2D-FFT appear perpendicular to the lines we observe in real space. This means that also the angles these k vectors form, are oriented perpendicularly to the ones in real space.

Depending on the symmetry of the system and the studied structure, the 2D-FFT plots may still require some post-processing to get the desired values. For example, in atomic resolution images, the periodicities indicated by 2D-FFTs do not always corresponds to inter-atomic distances (Fig. 3.3 (d) orange lines). Instead, they may be distances between lines of atoms (Fig. 3.3 (d) red lines). This can be different depending on the symmetry of the system. The measured distances can be used to solve simple trigonometric problems that lead to the real inter-atomic distances. For example, in the case of a hexagonal lattice like in Fig. 3.3 (d), the relation between the inter-atomic distance a and the line-line distance h is $a = \frac{2h}{\sqrt{3}}$.

Obtaining structural information via 2D-FFTs has its benefits and problems compared to obtaining it via real space measurements. The benefits include the averaging over the entire image, reducing noise and spatial variations of the patterns. 2D-FFTs can also reveal periodicities that are hard to identify in real space, such as similar periods which could appear as two close but distinct peaks. Finally, 2D-FFTs also give us information about how periodic a structure is. Depending on how localized the peaks in the 2D-FFT are, we get an understanding about how disperse the structure's period and direction are. On the other hand, 2D-FFTs also have certain drawbacks. First, it is necessary to have large images with high resolution of the structure to obtain good resolution in frequency space. Scanning artifacts such as thermal drift and creep of the piezoelectric scanner can directly modify the angles and distances between peaks in the 2D-FFTs. This makes angle and distance measurements not very reliable for large images. In particular, the slow-scan-direction peaks cannot precisely be determined. To diminish the impact of these artifacts it is always better to obtain quantitative values from the fast-scan-direction.

In conclusion, 2D-FFTs are a useful tool to characterize certain types of nanoscale structures. However, they should be complemented with real space analysis methods.

Inverse 2D-FFT filtering as a tool

Inverse two dimensional fast Fourier transform (I2D-FFT) filtering is a data processing technique that takes advantage of the Fourier transform bijection. The same way it is possible to perform a 2D-FFT, it is possible to obtain the original real space image from a 2D-FFT map when the phase is known. This opens the possibility to perform operations

in the 2D-FFT map before transforming it back to real space. These operations mainly consist of erasing or smoothing out peaks in the map before performing the I2D-FFT.

It is important to note that I2D-FFT filtering is a data processing technique, not a data analysis technique. As such, it modifies the original data and can introduce artifacts. For that reason it is recommendable to use it in a conservative way and avoid processed images as the only source for an argument. Here I discuss three ways to use it as a data-quality enhancing technique, just to better understand an already existing observation.

Noise reduction

This technique consists of erasing the 2D-FFT peaks created by noise during the measurement. This is only useful with periodic noise, such as electronic or vibration noise. After that, the I2D-FFT is performed and an improved real space image is obtained.

Structure identification

Sometimes, several different patterns may be superimposed on top of each other. This makes it extremely hard to discern which line or peak belongs to which pattern in real space. In this case just one set of peaks is selected in the FFT, and the other peaks are erased. When the I2D-FFT is performed, just one of the patterns remains. This procedure is followed for all the sets of peaks in the FFT so all patterns are identified. This permits the correlation between real space structures and their FFT peaks, where they may be easier to analyze and compare.

Structure location in real space

This is a particular application of the structure identification case. In this case, the different patterns are not located everywhere, but located in different parts of the image. This could be the case for a STM image with islands exhibiting different superstructures, such as in Fig. 3.4 (a). In this situation, one set of peaks is selected in the FFT and the others are erased (Fig. 3.4 (b)). When the I2D-FFT is performed we can identify the real space location of the structure where the corrugation of the remaining periodicity is larger (Fig. 3.4 (c)). The case of Fig. 3.4 is just a simple illustrative example of this technique.

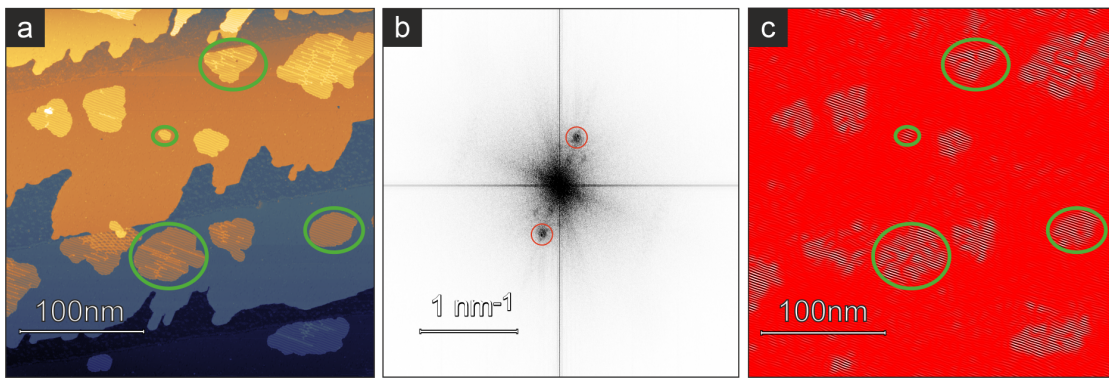


Figure 3.4: Structure location in real space. (a) Constant-height STM image of Cr first layer and second layer patches on Nb (110). The second layer exhibits a one-dimensional Moiré-like reconstruction. Some of these islands are indicated by green ellipses. (b) FFT of panel (a). Red circles indicate the frequencies corresponding to the Moiré-like reconstruction. (c) Image obtained as a result of performing a I2D-FFT of panel (b) using only the circled spots. The regions with high corrugation are the ones in which the spatial frequency is localized. The green ellipses indicate the same locations as in panel (a).

4 Growth and magnetism of first layer Mn/Ir(111)

"- Where'd you get the coconuts?
- We found them.
- Found them? [...] The coconut's tropical! [...] this is a temperate zone.
- The swallow may fly south with the sun or the house martin or the plover may seek warmer climes in winter, yet these are not strangers to our land?
- Are you suggesting coconuts migrate?"

— Monty Python, Monty Python and the Holy Grail

In this chapter I will discuss the results of the publication "*Phase Coexistence of Mn Trimer Clusters and Antiferromagnetic Mn Islands on Ir(111)*" [3].

I will start presenting the three structural phases that appear in the system. Afterwards I will comment on the differences observed at different measurement temperatures. Then I will focus on the three phases in detail, characterizing them structurally and magnetically. In the end I will discuss a low coverage sample preparation that helps understanding the relation between two of the studied phases.

4.1 Introduction

Antiferromagnetic (AFM) materials have recently gained notoriety due to their potential benefits in transport and spin dynamics with respect to the more studied ferromagnetic materials [9], [10], [11]. But the properties of AFM materials are also tailored by the substrate on which they are grown. For example hexagonal substrates create an interesting canvas for materials with AFM nearest-neighbor exchange. This substrate symmetry forces non-collinear frustrated AFM configurations when just nearest-neighbor exchange interactions intervene [61].

The growth modes of the materials on the substrate also play a role when determining the properties of the system. Classical metal-on-metal growth through MBE is heavily

dependent on deposition rate, diffusion coefficient and thermal energy, and thus determine the structure of the system. Generally, at sufficiently high temperature, deposited atoms are able to diffuse until they find a nucleation site, i.e. a step edge or a pinning defect, for example. The now immobile particles can work as nucleation centers for further incoming atoms enabling the film growth [62], [63]. Evaporated atoms can also be arranged into cluster superstructures. This is usually achieved when the superstructure's skeleton is already preexisting in the substrate in either a structural or electronic way, i.e. structural reconstructions or electron standing waves of noble metal surface states [64], [65], [66]. In these cases, the substrate's preceding pattern propitiates the growth of the clusters in certain points of the surface and inhibits it in others, thus generating the superstructure. Non-organized heterogeneous clusters have also been obtained due to charge transfer between the substrate and the clusters. The charge transfer generates out-of-plane electric dipole moments in the clusters that create a repulsive force among them [67]. However, this growth mechanism is not expected to occur regularly for metal-on-metal systems. For clusters, self assembly and homogeneity are two highly important characteristics. These properties allow their fabrication in large numbers and ensure reproducible behavior in fields related to catalysis [68], [69].

Here I report on the finding of three structural phases in the submonolayer regime of Mn/Ir(111). Two of these phases consist of extended films with different structural properties. The third one is a phase formed by monodisperse self-assembled clusters.

I will start introducing the three observed structural phases and talking about their temperature dependence to later discuss each of them in detail.

4.2 Mn/Ir(111): Three structural phases

Figure 4.1 shows the three phases observed in the first layer Mn/Ir(111) from lower to higher Mn coverage at $T = 4$ K. Figure 4.1 (a) shows the least dense Mn phase consisting of self-assembled monodisperse Mn clusters. This phase is also observed in Figure 4.1 (b) coexisting with the second phase, which consists of triangularly reconstructed Mn monolayer islands. Figure 4.1 (c) shows the third phase characterized as a pseudomorphic layer of Mn. This phase appears when the coverage of Mn approaches and reaches one atomic layer.

It is worth highlighting the phase coexistence at intermediate coverages as an unusual behavior for a metal-on-metal system. The typical metal-on-metal growth discussed in section 4.1 allows for either one or another growth mode, i.e. film growth or cluster growth, but not both. Whereas a similar coexistence was found in a non metal-on-

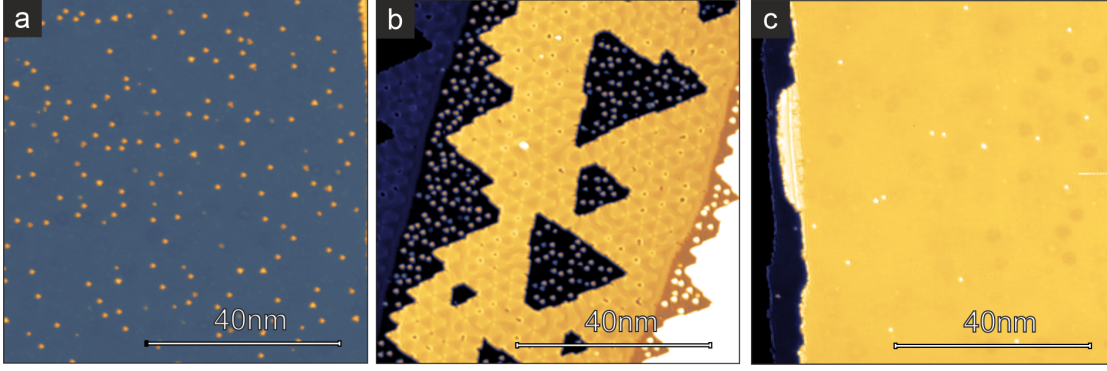


Figure 4.1: Overview of the three Mn on Ir(111) growth phases. (a) Overview constant-current STM image of a sample with extremely low Mn coverage with just the cluster phase visible. (b) Overview constant-current STM image of a sample with a coverage of around 0.7 atomic layers of Mn. In this regime of coverage, the cluster phase and the reconstructed phase coexist. (c) Overview constant-current STM image of a sample with a coverage of just above 1 atomic layer of Mn. The Mn monolayer now displays a pseudomorphic structure. (Measurement parameters: (a) $U = +10$ mV, $I = 1$ nA, $T = 4$ K, (b) $U = +100$ mV, $I = 500$ pA, $T = 4$ K, (c) $U = +30$ mV, $I = 1$ nA, $T = 4$ K, (all) Cr bulk tip)

metal system [67], I present the case of Mn/Ir(111) with such a phase coexistence in a metal-on-metal system.

4.3 Measurement temperature differences

To better understand the cluster phase we performed measurements at five different temperatures: 4 K, 80 K, 115 K, 150 K, and 300 K. The higher four temperature preparations are shown in Fig. 4.2 to highlight the differences between them.

In Fig. 4.2 the cluster phase appearance at different temperatures can be compared. In panel (a) we see the individual clusters of the cluster phase along with the island phase. In panel (b) and (c) we can see how the clusters appear less defined as they gain thermal kinetic energy and lose stability. Finally, in panel (d) the cluster phase cannot be observed. The structural characteristics of the reconstructed phase remain the same at all temperatures. A closer inspection of the vacancy islands at 300 K, i.e. the areas with no reconstructed Mn phase, reveals the existence of fast-moving particles below the tip when scanning. These particles appear as random spikes of current over the Ir, and never over the Mn, effectively reducing the apparent height of the Mn islands. The increasing movement of the clusters with temperature in panels (a-c) help us identify these particles as the clusters and relate this movement to temperature and not just interactions with the tip. The fact that STM is a slow data acquisition technique stops

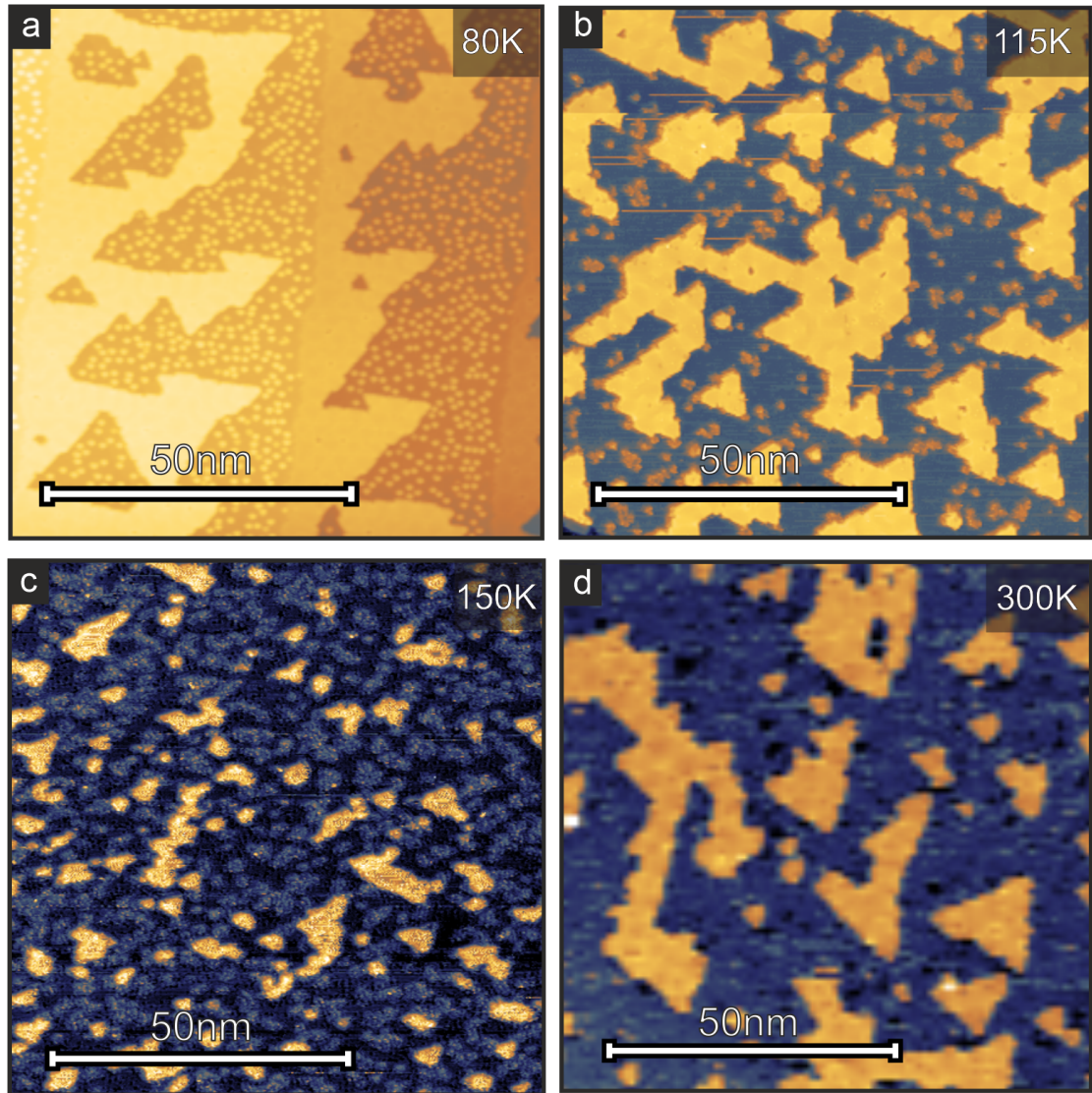


Figure 4.2: Measurements at different temperatures. (a-d) Constant-current STM measurements of Mn/Ir with submonolayer coverages ranging from 0.3 ML to 0.6 ML. (Measurement parameters: (a) $U = +50$ mV, $I = 100$ pA, $T = 80$ K, (b) $U = +650$ mV, $I = 600$ pA, $T = 115$ K, (c) $U = +6$ mV, $I = 50$ pA, $T = 150$ K, (d) $U = +650$ mV, $I = 800$ pA, $T = 300$ K, (all) Cr bulk tip.)

us from imaging these clusters while they move. From this data it is concluded that Mn clusters must also be mobile during deposition at room temperature or higher. On the other hand, when decreasing the temperature, clusters slow down to the point of freezing. The following study of the three structural phases was performed at either 4 K or 80 K, where the clusters do not move.

4.4 Mn pseudomorphic phase

4.4.1 Structure of the pseudomorphic phase

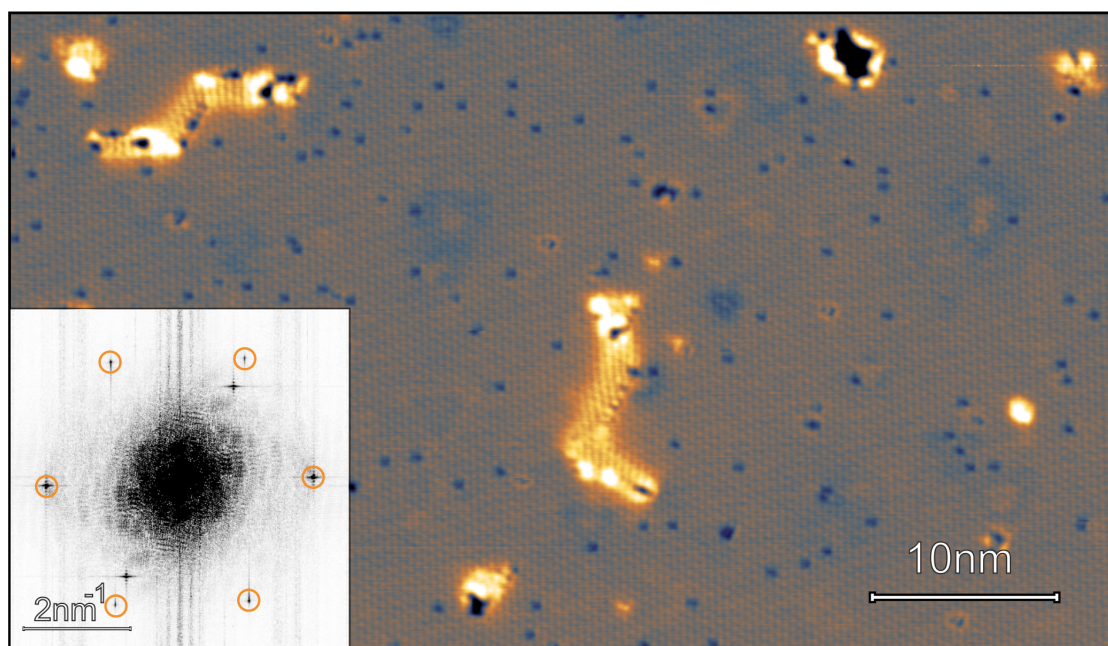


Figure 4.3: Atomic resolution of pseudomorphic phase. Constant-current STM image of an almost closed first layer of Mn on Ir(111) with atomic resolution. Inset: FFT of the real space image with orange circles indicating the peaks representing the atomic resolution. The two other main peaks observed correspond to noise in the image. (Measurement parameters: $U = +30$ mV, $I = 1$ nA, $T = 4$ K, Cr bulk tip)

Fig. 4.3 shows an atomic-resolution image of the almost complete first layer of Mn on Ir(111). The bright isolated structures on the surface are residuals of the reconstructed phase, and completely disappear when the coverage reaches the full first layer. The analysis of both the real space image and its fast Fourier transform (inset of figure 4.3) help determine the atomic structure of the layer to be the same one as the structure of the underlying Ir, i.e. hexagonal symmetry with a nearest neighbor distance of 272

pm. The structure being the same means that the first monolayer of Mn on Ir(111) is pseudomorphic when the coverage approaches, reaches and surpasses one atomic layer.

4.4.2 Magnetism of the pseudomorphic phase

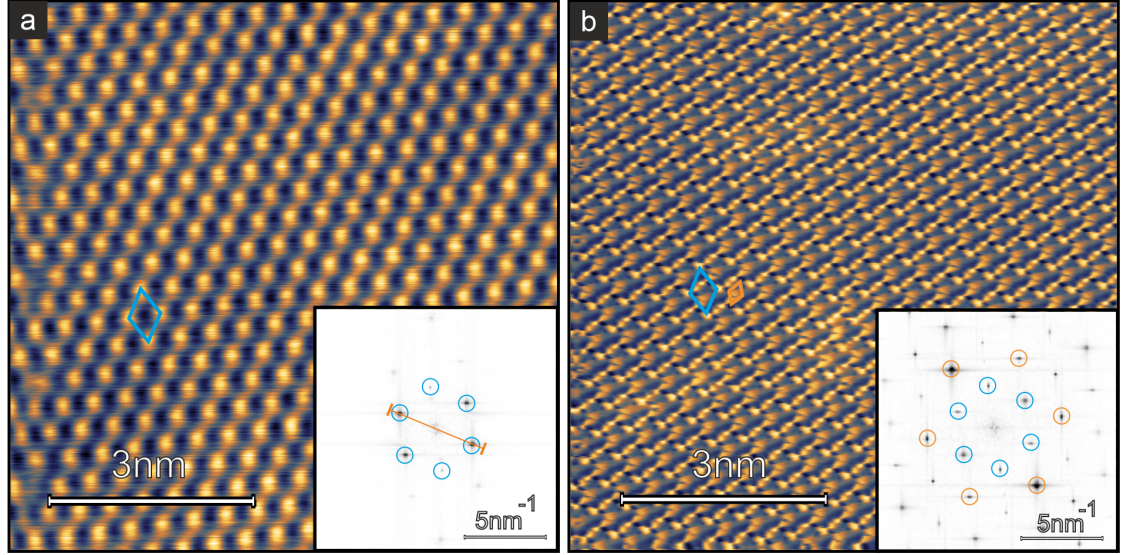


Figure 4.4: Magnetic resolution images of the Mn pseudomorphic layer. (a) Constant-current STM image of a fully closed first layer of Mn on Ir(111) with magnetic resolution. Inset: FFT of the real space image with cyan circles indicating the peaks representing the magnetic lattice. Orange line indicates the line profile displayed in Fig. 4.8. (b) SP-STM atom manipulation image of a fully closed first layer of Mn on Ir(111) with atomic and magnetic resolution. Inset: FFT of the real space image with orange circles indicating the peaks representing the atomic structure and blue circles indicating the peaks representing the magnetic superstructure. (Measurement parameters: (a) $U = +3$ mV, $I = 870$ pA, $T = 4$ K, (b) $U = +10$ mV, $I = 5$ nA, $T = 4$ K, (all) Cr bulk tip)

To study the magnetism of the pseudomorphic layer an antiferromagnetic Cr tip was used. In Fig. 4.4 (a) the observed magnetic structure is displayed. We identify this magnetic ground state as the Néel state (section 2.2.1). The Néel state observed via SP-STM appears as a hexagonal superstructure with a unit cell $\sqrt{3}$ times larger than the atomic one and rotated by 30° with respect to this one. This occurs as the tip spin is always more parallel (or antiparallel) to one of the three spin orientations of the sample than to the other two ones. The inset in Fig. 4.4 (a) is the FFT of the real space image where the magnetic peaks have been highlighted with cyan circles. The lattice constant of the magnetic unit cell is 468 pm, also indicated in cyan. This is, as expected, $\sqrt{3}$ times

larger than the atomic lattice constant of the Mn pseudomorphic phase. The magnetic superstructure is therefore characterized as a $(\sqrt{3} \times \sqrt{3})R30^\circ$ structure, i.e. the Néel state.

Fig. 4.4 (b) shows a spin polarized atom manipulation image where simultaneous structural and magnetic data have been measured. Atom manipulation images are obtained when an atom is dragged along with the tip while scanning. During this procedure the STM current goes always through the dragged atom. This atom is measured again and again over the different adsorption sites. The different electronic properties of each adsorption sites give rise to different contrasts. This gives us information about the crystal structure. In this case, the measurement is also spin-polarized, i.e. a spin polarized atom manipulation image. This means that in addition to the topographic information it also contains magnetic information. This type of images is notably difficult to interpret in real space due to the superposition of data with different physical origins. FFT analysis is the ideal tool to identify the different sets of information in the data. The distinct orientations, symmetries and sizes appear much more clearly and become easier to characterize in the FFTs. Performing inverse FFT filtering also allows us to individually correlate spots in the real space image to the magnetic or electronic structures. In the inset of Fig. 4.4 (b) the FFT of the real space image exhibits two main sets of peaks. The cyan circles highlight the peaks corresponding to the magnetic superstructure. The orange circles highlight the peaks corresponding to the topographic structure. It is easy to see in the FFT how both structures, although having the same hexagonal symmetry, exhibit different periods and relative orientation (30° difference). The corresponding unit cells are demarcated in the real space image with their respective colors. Their sizes and orientations are the expected ones for the atomic structure and Néel state.

4.5 Mn reconstructed phase

The Mn reconstructed phase coexists always with the Mn cluster phase discussed in section 4.6. This reconstructed phase forms extended Mn islands while the cluster phase inhabits the vacancy islands left by the reconstructed phase. In this section I will discuss the Mn reconstructed phase.

4.5.1 Structure of the reconstructed phase

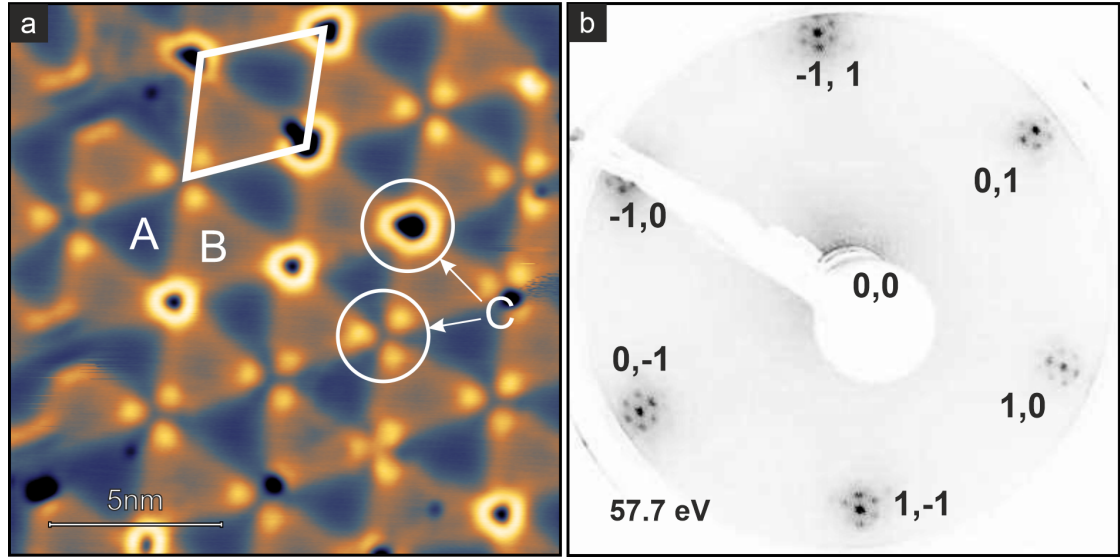


Figure 4.5: STM and LEED observation of the Mn reconstruction. (a) Constant-current STM image of a submonolayer patch of Mn on Ir(111). (b) LEED image obtained from a sample exhibiting the reconstructed Mn phase. (Measurement parameters: (a) $U = +10$ mV, $I = 1$ nA, $T = 4$ K, Cr bulk tip (b) $E = 57.7$ eV).

When the Mn reconstructed phase is studied with a non-magnetic tip such as in Fig. 4.5 (a) a triangular reconstruction with three different regions is observed. These regions are: darker triangles (A), brighter triangles (B) and the connection among six triangles (C). The lattice constant of the reconstruction (indicated by the white diamond in Fig. 4.5 (a)) is 3.8 nm, i.e. around 14 nearest neighbor distances of the Ir substrate. This type of structure can be understood as a Moiré reconstruction where the different triangles (A & B) happen to be atoms in different lattice sites (stackings) and the meeting points of six triangles (C) are where the Mn atoms are positioned on top of Ir atoms. The (C) positions appear in two different ways (see Fig. 4.5 (a)). One of them is the absence of atoms in the on top positions, the other case is when the hole is closed and three bright spots take its place. This type of Moiré is created by a lattice mismatch between the Mn top layer and the Ir bottom layer. The symmetry of the reconstruction along with the symmetry of the substrate implies an isotropic change of the lattice constant of the Mn. The modeling of the reconstruction as a Moiré structure using eq. 3.3 reveals a roughly 7% mismatch between both layers.

In Fig. 4.5 (b) the LEED pattern generated by a sample exhibiting the reconstructed phase is shown. In this image one can observe the six main spots on the LEED screen

generated by the hexagonal atomic structure of the Ir (111) crystal. Surrounding these spots, smaller sets of six spots created by the triangular reconstruction appear. The ratio between the reciprocal lattice vectors of the main spots and the smaller spots is roughly $1/15$, confirming a lattice mismatch of around 7%.

The difficulty to obtain atomic resolution on the Mn reconstructed phase made harder to determine if the lattice mismatch that generates the Moiré superstructure corresponds to an expansion or a compression of the Mn layer. The way to determine this is comparing the magnetic state of the pseudomorphic layer with the magnetic state of the reconstructed one. This is discussed in section 4.5.2.

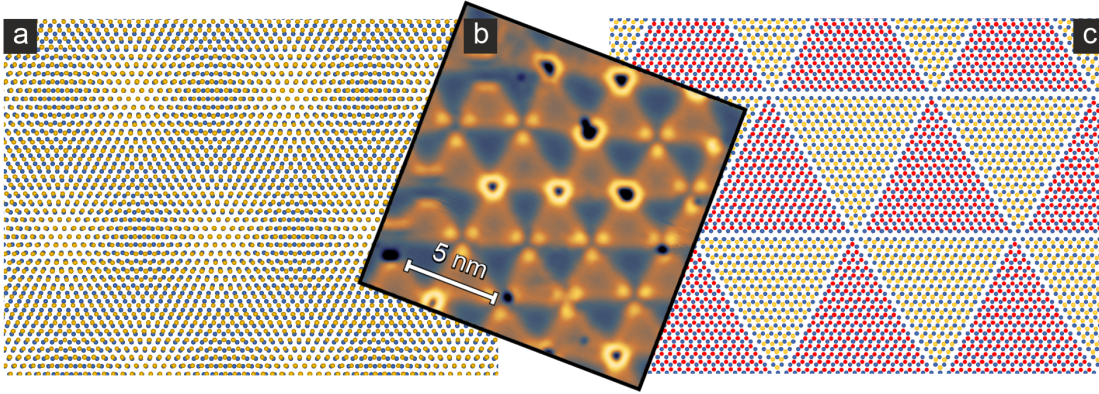


Figure 4.6: Model of the Mn reconstruction. (a) Ideal Moiré model created by two hexagonal layers in which the top one is expanded by 7% with respect to the bottom one. (b) Constant current STM image showing the reconstructed monolayer of Mn on Ir(111). (c) Tiling pattern generated by triangular patches in different stackings. (Measurement parameters: (b) $U = +10$ mV, $I = 1$ nA, $T = 4$ K, Cr bulk tip)

The well defined border between the different stackings of the Mn layer give rise to the idea of a distorted Moiré formed by homogeneous patches of alternating stackings. This can still be understood as a Moiré-like structure. The proposed model of the reconstruction is therefore a distorted Moiré where the transition between stackings is sharper than in the ideal Moiré. The ideal Moiré and the discrete patches with different stackings are shown in Fig. 4.6 (a) and (c) as the extreme cases between which the observed reconstruction (b) occurs.

4.5.2 Magnetism of the reconstructed phase

The observed magnetic state for the Mn reconstructed phase is the Néel state. In Fig. 4.7 (a) and (b) it is possible to see the magnetic hexagonal superstructure as well as the structural triangular superstructure. Once again, its analysis through FFTs and real

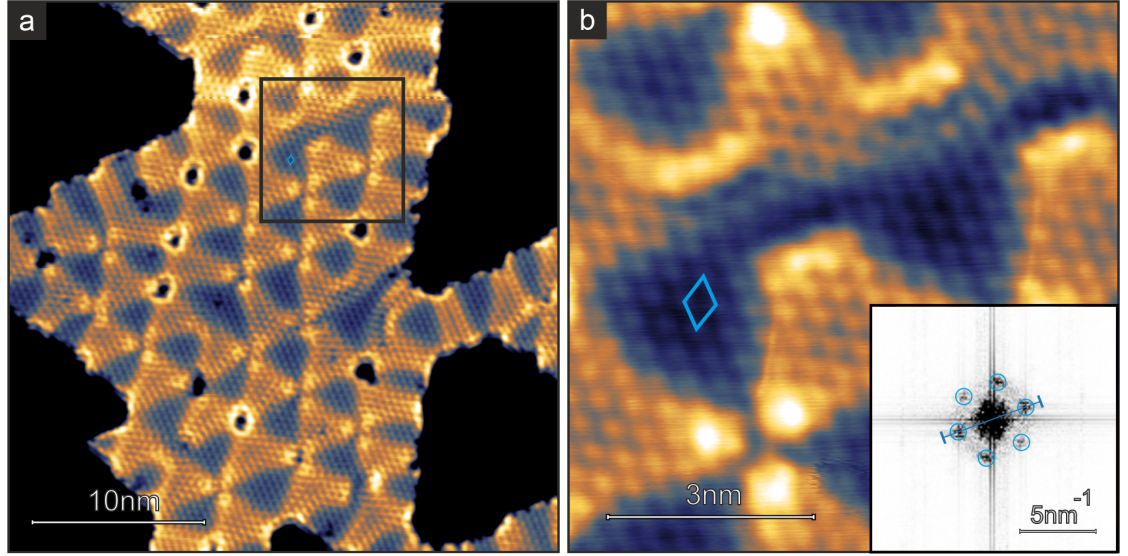


Figure 4.7: Magnetic resolution images of the Mn reconstructed phase. (a) Constant-current SP-STM overview image of a Mn reconstructed island with magnetic resolution. (b) Constant current SP-STM close-up image showing the magnetic superstructure in more detail. Inset: FFT of the real space image with cyan circles indicating the peaks representing the magnetic resolution, the blue line indicates the line profile displayed in Fig. 4.8. (Measurement parameters: (a) $U = +10$ mV, $I = 1$ nA, $T = 4$ K (b) $U = +5$ mV, $I = 900$ pA, $T = 4$ K), (all) Cr bulk tip

space, i.e. its size and orientation with respect to the main crystallographic directions, help us identify it as the Néel state.

The size of the pseudomorphic and the reconstructed magnetic unit cells were compared through line profiles in their FFTs. This is shown in Fig.4.8 confirming roughly a 7% mismatch between the pseudomorphic and the reconstructed layers. In particular, it determines the mismatch to be an expansion of the Mn reconstructed layer over the Ir below. As the comparison is done in reciprocal space, the peaks of the reconstructed phase (blue) are closer together than the ones of the pseudomorphic phase (orange). The line profiles of the FFTs are the ones indicated in Fig.4.4 (a) inset and Fig.4.7 (b) inset. The reconstruction being expanded means that there is a smaller amount of Mn atoms in the top layer than Ir atoms below. The density of Mn atoms is 87% the density of Ir atoms below, i.e. the Mn layer has 0.87 times the number of atoms of the Ir layer below in a given area.

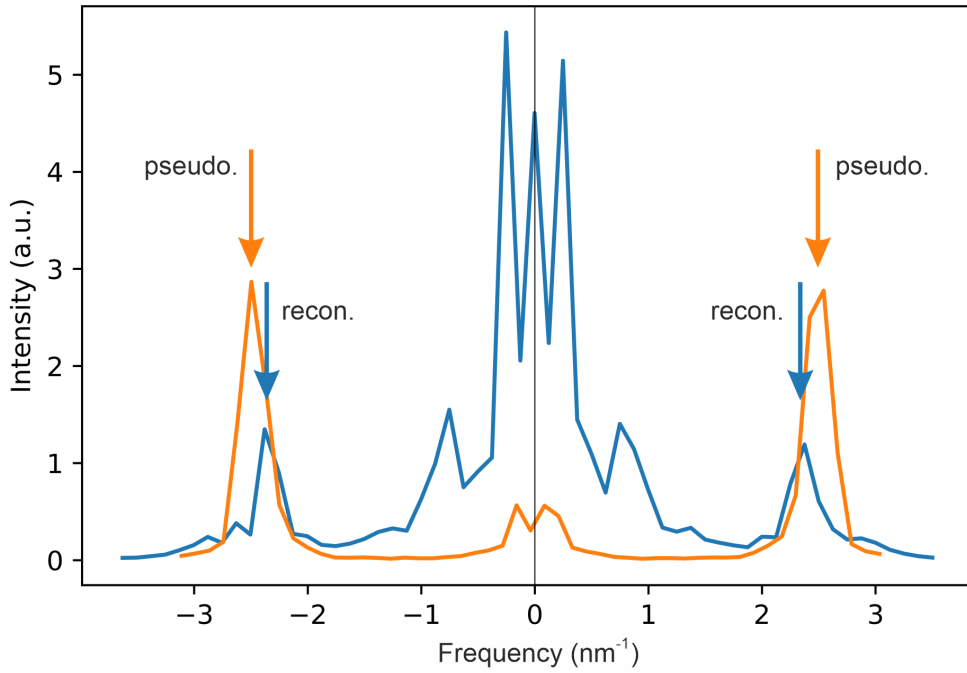


Figure 4.8: FFT comparison of the pseudomorphic and reconstructed Néel states through line profiles of Fig.4.4 (a) inset and Fig.4.7 (b) inset.

For the Néel state of the reconstructed layer extra measurements were performed with an Fe-coated W tip. The goal of these measurements was to study the system with known tip magnetization direction to determine the orientation of the Néel state. It has been shown before that Fe-coated W tips tend to have an in-plane magnetization axis at 0 T applied field [54]. When a magnetic field on the order of a few Teslas is applied, the tip aligns its magnetization axis with the field due to its ferromagnetic nature. As Mn is an antiferromagnetic material, this kind of interaction between the sample and the field is not expected for the available field strengths, i.e. the sample magnetic ground state is unaffected by the field.

The performed experiment consists of the three steps shown in Fig.4.9 (a-c). First, an extended reconstructed layer was measured with the Fe-coated W tip with no applied magnetic field, obtaining the image 4.9 (a). After this data was taken, a -2T magnetic field was applied perpendicular to the surface of the sample. As represented in the sketch in Fig.4.9 (b), the magnetization direction of the tip almost aligns with the applied field, while the sample remains unchanged. Finally, in Fig.4.9 (c), the magnetic field is switched off and another image is taken to confirm that we recover the original state. All these measurements are taken avoiding any structural tip changes to make

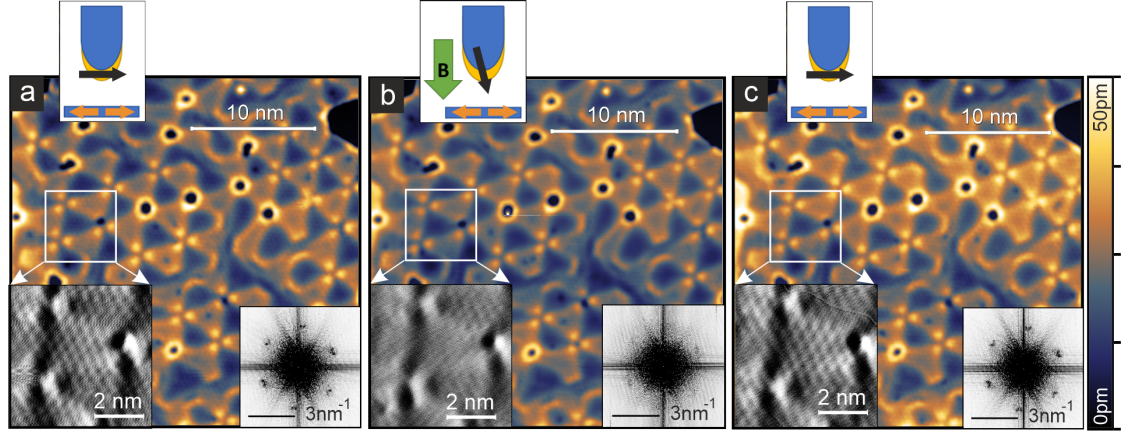


Figure 4.9: Out-of-plane magnetic measurements of the Néel state in the reconstructed Mn phase. (a-c) Constant-current spin polarized STM measurements of the same region of the sample with different tip magnetization directions indicated by the sketches. The FFTs are obtained from the respective real space images. Insets are close-up current images of the indicated areas. (Measurement parameters: (a) $B = 0$ T, (b) $B = -2$ T, (c) $B = 0$ T, (all) $U = +9$ mV, $I = 1.5$ nA, $T = 8$ K, (all) Fe-coated W tip)

the images comparable.

Through the series of data in Fig. 4.9 one can see how the magnetic contrast of the Néel state is present both in Fig. 4.9 (a) and (c), while it is diminished in (b). This is easier to appreciate in the insets where the magnetic corrugation is more obvious. It becomes very clear in the FFTs, where the Néel state appears as well defined points forming an hexagon in (a) and (c) but it is significantly fainter in (b). This experiment allows us to identify the orientation of the Néel state in our sample. The absence of contrast occurs when the magnetization of the tip is perpendicular to the plane in which the spins are contained. In the present case, the contrast is diminished when the out-of-plane direction for the tip is approached, i.e. the Néel state in the Mn reconstructed phase has its spins in the surface plane.

4.6 Mn cluster phase

The Mn cluster phase appears as soon as Mn is deposited onto the Ir substrate and remains present until the vacancy islands disappear. This means that the Mn cluster phase coexists with the reconstructed phase for most of the Mn coverage range. In this section I will focus independently on the Mn cluster phase, as the Mn reconstructed phase has already been discussed in the previous section.

4.6.1 Cluster types and behavior

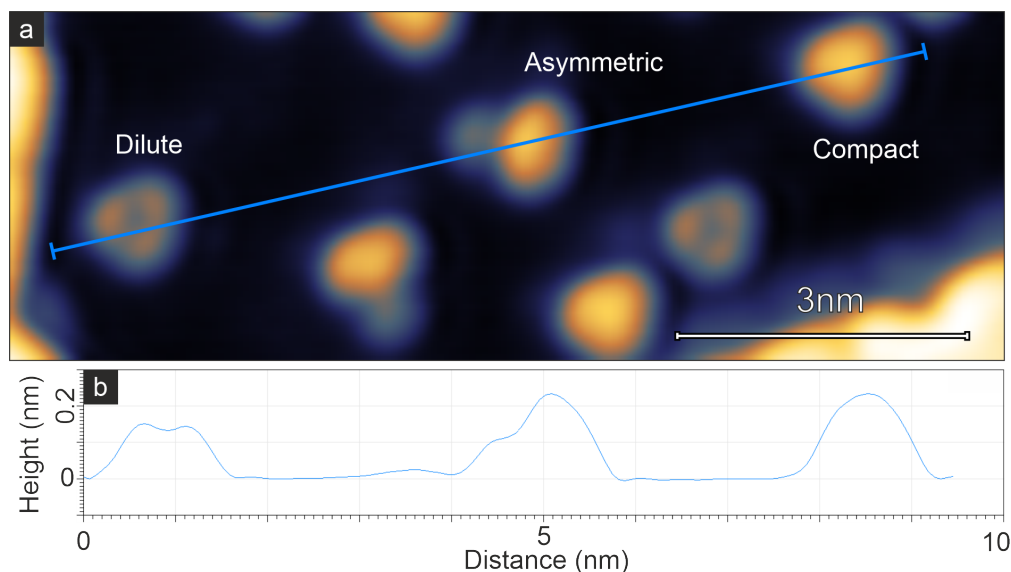


Figure 4.10: Types of clusters (a) Constant-current STM measurement displaying a vacancy island populated by the three different types of clusters. (b) Line profile obtained along the path indicated in the real space image. (Measurement parameters: (a) $U = +10$ mV, $I = 1$ nA, $T = 4$ K, Cr bulk tip)

When observing the Mn cluster phase, it is possible to identify mainly three types of clusters. In Fig. 4.10 they are indicated as *Dilute*, the smallest in height of the clusters, *Compact*, the biggest of them, and *Asymmetric*, the one lacking three-fold symmetry. When measured with standard parameters (around $U = +10$ to $+100$ mV, $I = +1$ to $+5$ nA), Compact and Asymmetric clusters have an apparent height of around 0.25 nm, or around 80% the height of the reconstructed phase. Dilute clusters on the other hand have an apparent height of around 0.15 nm, or around 50% the height of the reconstructed phase. The ratios between these configurations depend on the exact preparation and vary considerably.

It was found that the clusters can change between their different types. In Fig. 4.11 (a-c) it is shown how the clusters in a vacancy island change when scanned at 1 V. For better comparison of these images, the z scale and origin are adjusted to be the same in every panel. Fig. 4.11 (a) and (c) are measured at the same voltage to show the differences between before and after the 1 V measurement, which is displayed in Fig. 4.11 (b). In panel (b) it can be seen how the clusters become shorter when the tip scans over them (see inset in Fig. 4.11 (b)). This change was found to be not reversible. Fig. 4.11 (d) shows how this newly formed Dilute clusters behave under more extreme voltages, in

this case -2 V. The image reveals how some of the Dilute clusters are quite unstable and appear noisy in the measurement while others remain stable in their configuration. This instability moves the individual atoms inside the cluster, but it does not move the cluster as a whole. The circles placed through the series of images highlight model-type clusters for the three main behaviors observed. The behavior classification takes into account the original cluster, the final cluster, and the apparent stability of the final cluster:

- Red circle: Asymmetric clusters that evolve to **unstable** Dilute clusters.
- Green circle: Compact clusters that evolve to **unstable** Dilute clusters.
- White circle: Compact clusters that evolve to **stable** Dilute clusters.
- Cyan circle: Dilute clusters that remain **stable** Dilute clusters.

The rectangles in Fig. 4.11 (a) and (c) indicate the cut-outs later used in Fig. 4.19 (b) and (c).

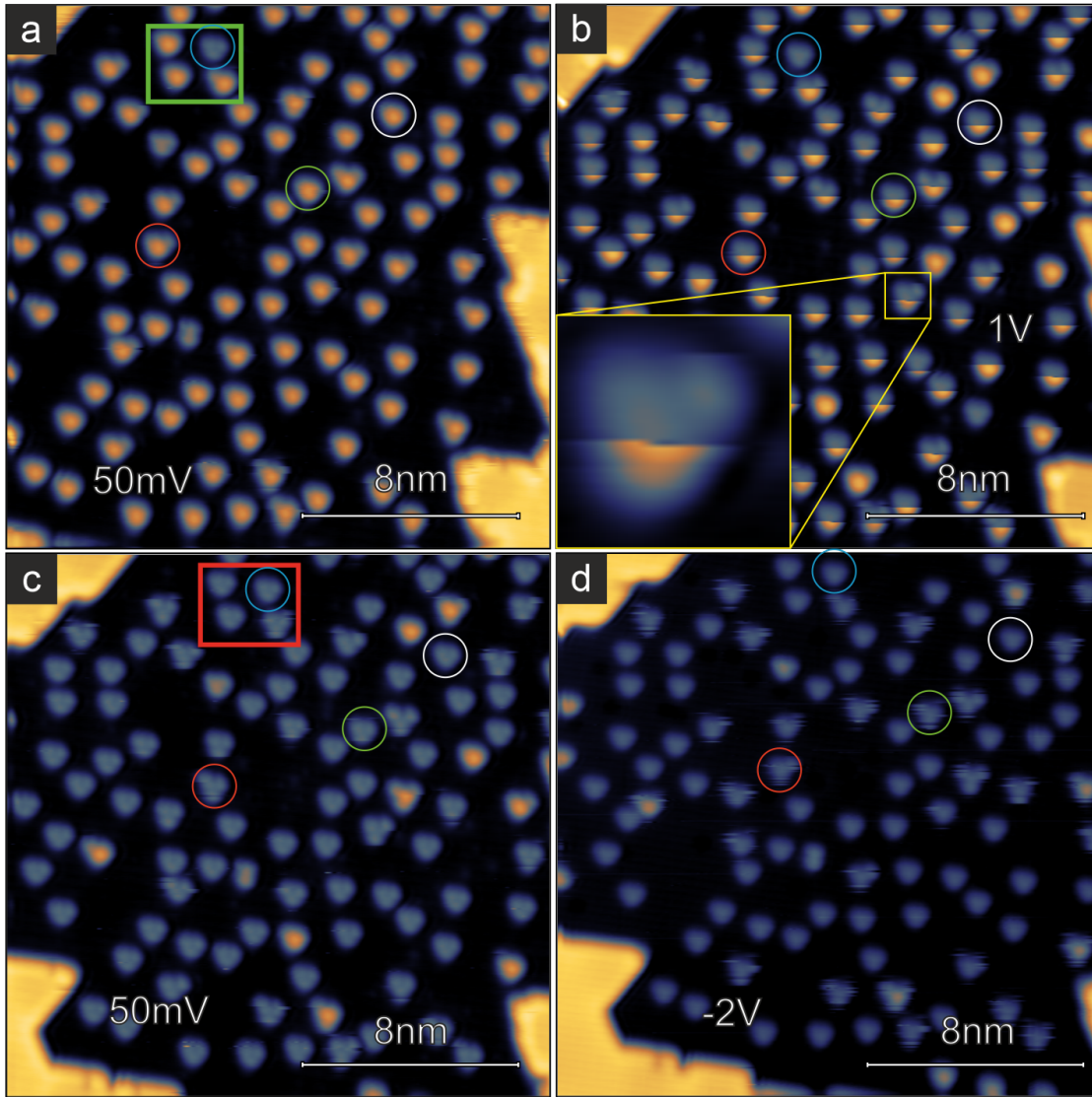


Figure 4.11: Cluster change and stability via imaging. (a-d) Constant-current STM series of measurements showing how the clusters evolve and their behavior at high voltages while measured via STM. (Measurement parameters: (a) $U = +50$ mV, $I = 100$ pA, $T = 80$ K, (b) $U = +1$ V, $I = 4$ nA, $T = 80$ K, (c) $U = +50$ mV, $I = 100$ pA, $T = 80$ K, (d) $U = -2$ V, $I = 4$ nA, $T = 80$ K, (all) Cr bulk tip)

To further study the cluster change and stability via their interaction with the tip, a different type of experiment was performed. In this case, the experiment consisted of identifying either Compact clusters or Asymmetric ones. After that, the tip was positioned just on top of the cluster to study using atom tracking software. This software detects the curvature of the surface below the tip and moves the tip towards higher positions,

finding in this way local maxima. Once the tip was stabilized over the cluster (measuring around half an hour in the area plus around one minute over the cluster), the parameters to perform a bias sweep were selected and the bias sweep was performed. This consisted of stopping the feedback loop and gradually changing the applied voltage between tip and sample while recording the current. With this technique, clusters can be changed individually, as shown in Fig. 4.12.

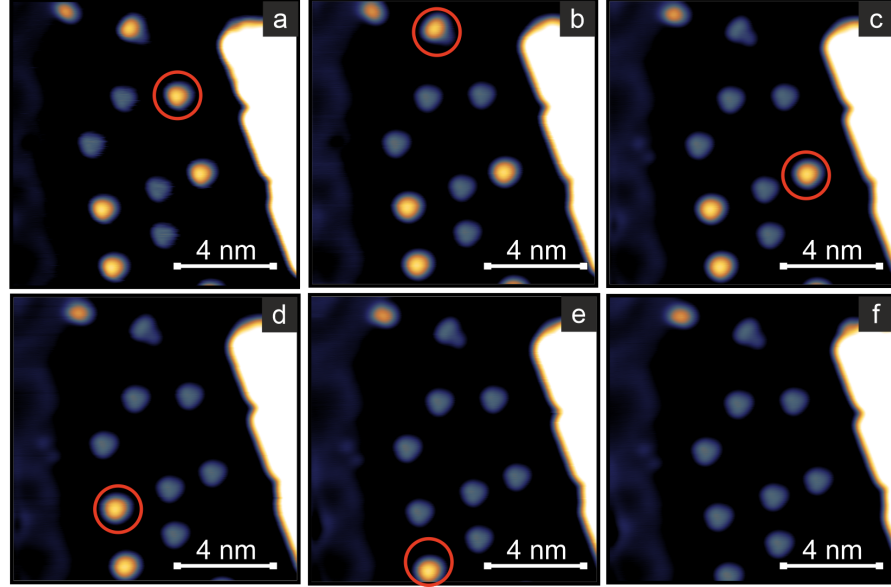


Figure 4.12: Cluster change via bias sweeps. (a-f) Constant-current STM series of measurements showing how different Compact and Asymmetric clusters were transformed into Dilute ones individually with local tunnel currents. The clusters highlighted in red are the ones changed before the next image. (Measurement parameters: (all) $U = +10$ mV, $I = 1$ nA, $T = 80$ K, Cr bulk tip)

Repeating this experiment over many clusters, we obtain the curves in Fig. 4.13. Each curve in each panel is done over a different cluster and when cluster changes happen the current drops occur. In Fig. 4.13 (b) it is shown how the clusters change approximately at 1.1 V when the tip has been stabilized at $U = +110$ mV and $I = 200$ pA. This contrasts with the unchanged status of the clusters for negative voltages with the same tip stabilization parameters as shown in panel (a). When performing the experiment again with a smaller tip-cluster distance, different results are obtained. The voltage needed in Fig. 4.13 (d) to change the clusters is smaller than in Fig. 4.13 (b). With these different stabilization parameters it is possible to see in panel (c) how the negative voltages also switch the clusters.

Here we observe that the absolute value of the voltage needed for the switching to occur is higher than in the positive case. From these experiments it is inferred that the abso-

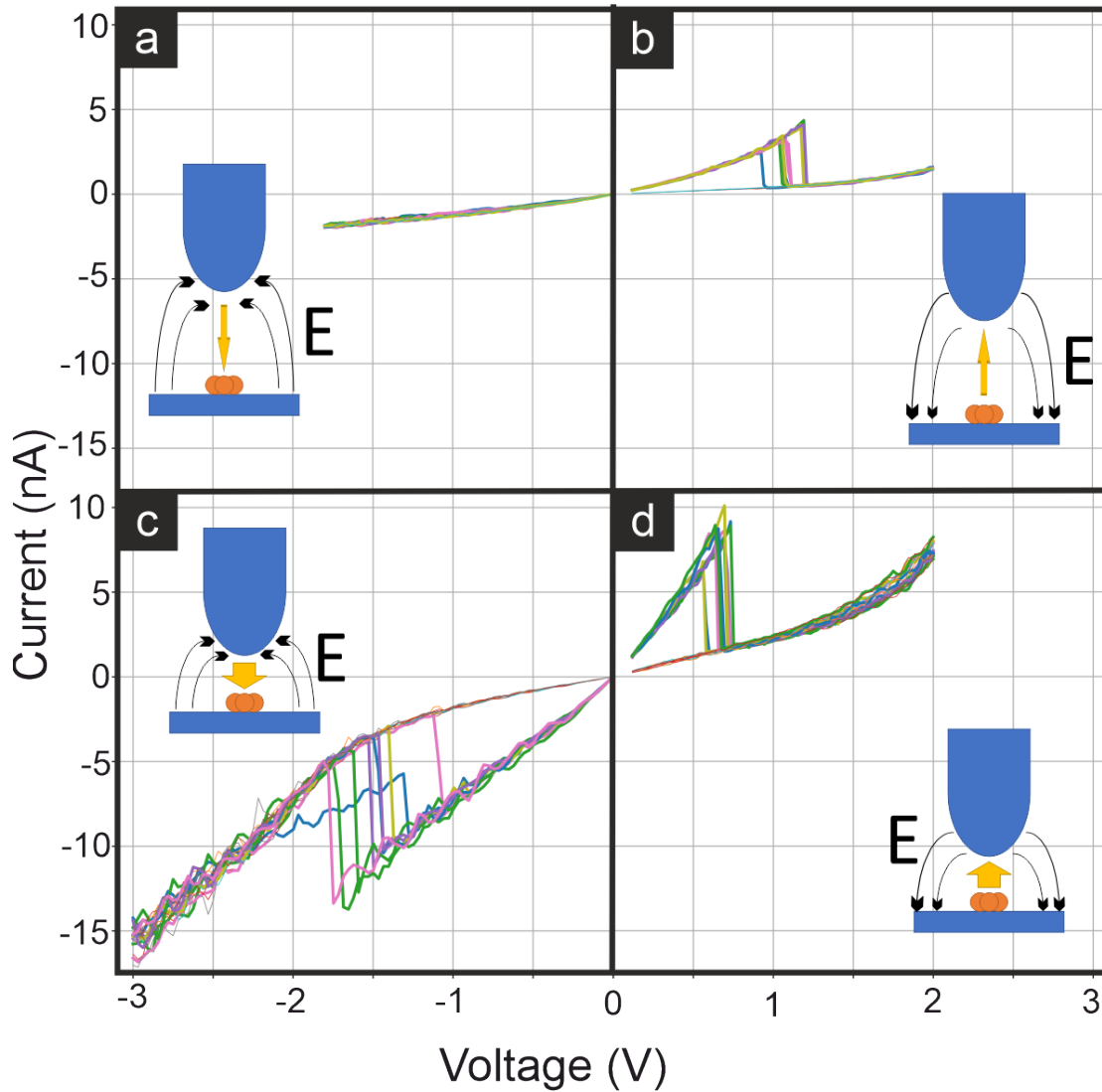


Figure 4.13: Obtained curves via bias sweeps. (a-d) Series of bias voltage sweeps from small to large voltage over different clusters with same tip-sample distances: (a) and (b) are done with larger tip-sample distance while (c) and (d) are done with smaller tip-sample distance. The abrupt current drops indicate the clusters switching to Dilute ones. (Measurement parameters: Stabilization parameters before bias voltage sweeps: **(all)** $U = +110$ mV, **(a,b)** $I = 200$ pA, **(c,d)** $I = 1$ nA, **all** $T = 80$ K, **(all)** Cr bulk tip)

lute value of the voltage is not the only parameter responsible for the cluster change. We also determine that the current alone is not responsible for the change either, as the currents at which the switching happens are 3.5 nA and 8.4 nA for the two positive cases. Finally, the switching power is also not the determining factor, as it is on average 3.9 nW and 5.9 nW for positive voltages in panels (b) and (d). The different sign offset in the required voltage to generate the switching is not fully understood. A possibility to explain it could be the electric field generated by the tip. If the clusters have a dipole moment, as it has been seen in [67], an electric field could favor the integrity of the clusters for a particular polarity while facilitating their structural change with the opposite one. However, even if this is the case regarding the observed asymmetry, the mechanism that strictly generates the switching at both positive and negative bias voltage is not yet understood.

Some possible explanations for the clusters being metastable include their magnetic state (further discussed in section 4.6.5) and the expansion of the Mn layer. The magnetic explanation considers that the clusters lose their mobility before they reach their Néel temperature while cooling the system. This could result in the Dilute clusters being energetically favorable when magnetism is present, but not when they are formed at room temperature. In this scenario, the energy received during the voltage sweeps could let them overcome the barrier between the two configurations and go to the lower energy state. The expanded Mn explains the behavior because the strain in between the expanded Mn atoms of a cluster could propitiate their movement to a more stable position where the atoms are further away in perfect three-fold hollow site positions.

4.6.2 Cluster density and distribution

Another aspect studied was the clusters' density and relative position to each other. This is shown in Fig. 4.14. In Fig. 4.14 (a) we can see a vacancy island in which the positions of the clusters have been marked. With these data we obtain the graph of Fig. 4.14 (b). This graph is a pair correlation between each of the clusters with all the other ones in this vacancy island. No spatial ordering among clusters is found except a minimum distance between clusters of around 1.35 nm, i.e. 5 atomic distances (indicated by the red circles). This can be understood as a short distance repulsion. This analysis was repeated with another data set and the results were equivalent.

If we ideally fill the Ir surface with clusters respecting the minimum cluster distance we would obtain an idealized hexagonal cluster phase superstructure. In that case, the cluster density would be maximized. The cluster density for those conditions would be 0.63 clusters/nm². This value contrasts with the observed cluster densities shown

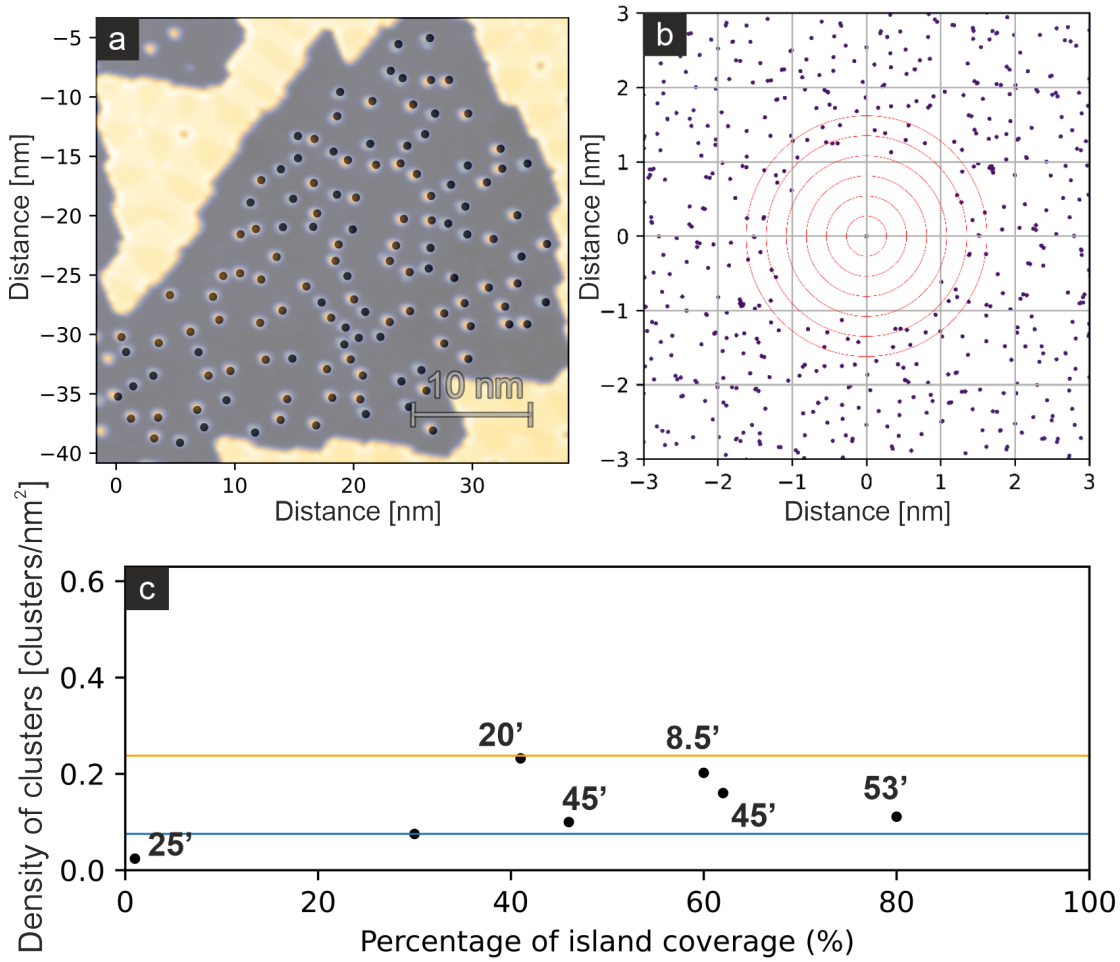


Figure 4.14: Cluster pair correlation and density (a) Constant-current STM image centered in a vacancy island with the exported cluster positions superimposed. (b) Pair correlation of the cluster positions in panel (a). (c) Cluster density as a function of reconstructed phase coverage. Each data point represents a different sample preparation. The numbers next to the points represent the time between last flash and Mn deposition. (Measurement parameters: (a) $U = +50$ mV, $I = 1$ nA, $T = 4$ K, Cr bulk tip)

in Fig. 4.14 (c). The observed cluster densities remain around significantly lower values (0.08-0.24 clusters/nm²) independent of the temperature of the sample during the evaporation or the Mn coverage. To explain this phenomenon I propose that a local increase of the cluster density above the 0.24 clusters/nm² could result in the spontaneous formation of reconstructed phase sections. This growth would happen at the expenses of the cluster phase, which is mobile at room temperature when the growth occurs, as already discussed in section 4.3. This idea is represented schematically in Fig. 4.15. The decrease of cluster density combined with the increase of the reconstructed phase surface would explain the roughly constant cluster density for different Mn coverage preparations. The cluster density obtained in a certain preparation would then be determined by the moment in which the Mn evaporation is stopped. The agglomeration of data-points between 0.08 clusters/nm² and 0.24 clusters/nm² hints to a narrow range of densities for the cluster phase, see Fig. 4.14. Note that the reconstructed phase growth occurs in complete sections of the reconstruction. This can be seen at the edges of the reconstructed phase, which always include full triangles of the reconstruction.

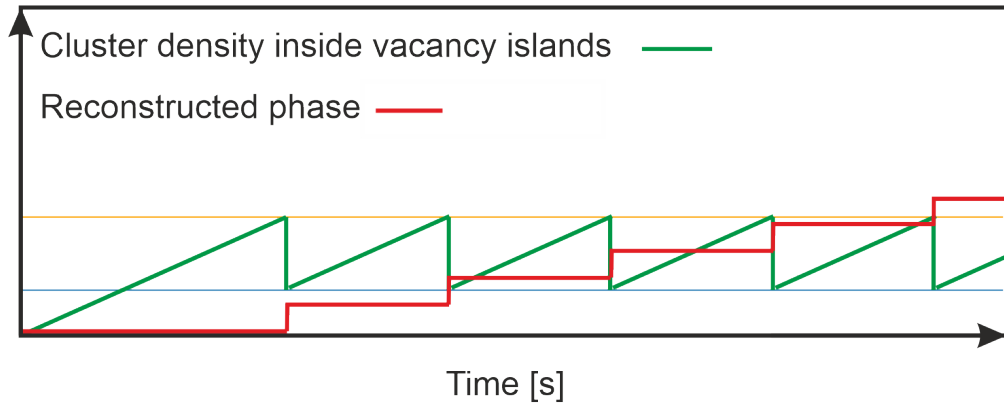


Figure 4.15: Schematic representation of the growth relation between the cluster phase and the reconstructed phase. The orange and blue lines represent the maximum and minimum values between which the cluster density oscillates.

Adding this knowledge to the cluster movement at room temperature, we can understand the cluster phase as a 2D cluster gas frozen in place when the temperature is decreased. Its relative distribution being only governed by a small repulsive force, while its density being confined around 0.16 clusters/nm². The density is constantly increasing due to the evaporation, and suddenly decreasing when sufficiently high to form the reconstructed phase.

A potential explanation of the cluster-cluster repulsion can be the dipole moments of the clusters that could also give rise to the asymmetry in the switching mechanism. If every cluster had an equal out-of-plane dipole moment, electrostatic repulsion could be

the force behind their distancing. Another possible explanation for this repulsion could be the expansion of the Mn atoms discussed in section 4.5.2. In that case, the Mn atoms forming a cluster would be forced outwards from the perfect hollow sites. That could make the addition of more atoms to the cluster difficult, as they would be forced to reside in unfavorable positions far away from hollow sites. One last explanation for the cluster-cluster repulsion could be the existence of standing electron waves determining stable areas around the clusters. This is not a possibility since there is no surface state crossing the Fermi energy in Ir(111) [70].

4.6.3 Cluster orientation

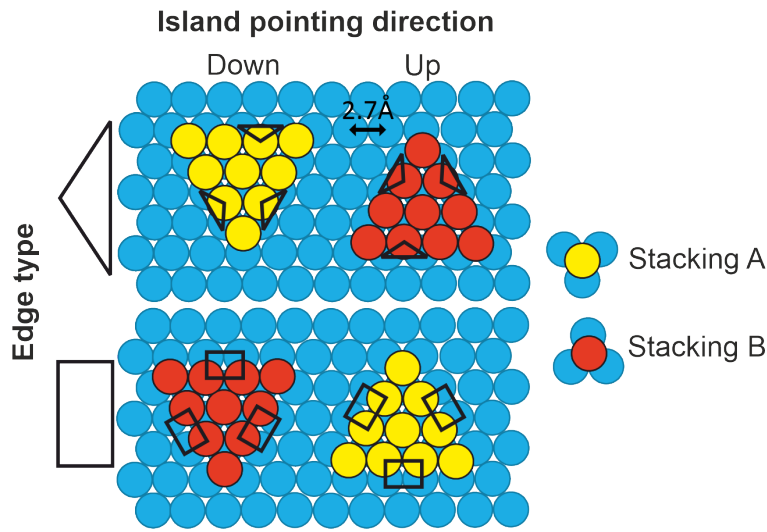


Figure 4.16: Schematic relations between edge type, stacking and island pointing direction. Different colors of the top atoms represent different stackings. The edge types are represented by black triangles and rectangles joining the bottom layer atoms with the top layer ones.

The clusters (almost) always show the same orientation. This means that their triangular shapes are (almost) always found pointing in the same directions with respect to each other along the whole crystal, i.e. the clusters exhibit C3 symmetry. Other systems with hexagonal top layer symmetry sometimes exhibit C6 symmetry as islands in two different stackings with triangular shapes pointing in opposite directions [71], [72] [73]. In these systems, a particular type of edge (triangle or square, see Fig. 4.16) is more energetically favored than the other one. If both atomic stackings are similar in energy, then both of them will occur, but they will give rise to islands pointing in different directions. This way, the favored edge type is preserved, as shown in Fig. 4.16. This means that the edge type is fixed, and then for each stacking, a particular island orientation

tation is allowed. This contrasts with our cluster observations. In the case of the Mn clusters, the fixed parameter is their pointing direction, and then for each stacking, a particular cluster edge is chosen. This reveals the possibility of two identically looking objects with different stackings and edges, which could lead to two different behaviors, just as observed in section 4.6.1.

4.6.4 Cluster structure

To fully characterize the clusters the aim is to create a cluster model that describes them structurally while explaining the three observed behaviors in Fig. 4.11.

The first unknown to tackle is the amount of atoms forming the clusters. For this, I performed atom manipulation experiments with different clusters such as the one displayed in Fig. 4.17. In these experiments I consistently found that all clusters are formed by three atoms, making them trimers. Clusters changing from one to another type would just require structural changes and not the addition or subtraction of atoms. The last two panels in Fig. 4.17 show two artificially built cluster structures that more or less resemble the other clusters observed with the same tip in the top part of the images.

Once clusters are known to be trimers, a series of constant-height STM simulations were performed to identify the atom configurations that give rise to the three observed cluster types, i.e. Compact, Dilute and Asymmetric clusters. The simulations displayed in Fig. 4.18 (a) coincide with the three known cluster types shown in Fig. 4.18 (b). The structural models of these configurations are shown in Fig. 4.18 (c). The Compact Trimer (CT) model comes from packing three Mn atoms as nearest neighbors. The Dilute Trimer (DT) model comes from packing three Mn atoms at the distance of two lattice constants. The Asymmetric Trimer (AT) model comes from packing two Mn atoms as nearest neighbors and adding the third one as represented in Fig. 4.18. Other configurations for the third atom of the AT do not reproduce the observations with the simulations.

The structural model in Fig. 4.18 (c) reproduces our imaging observations, but it also reveals how CT and DT clusters could appear in two different stackings in which their atomic distances are the same. This means that even though two clusters could appear to be the same type of trimer in an STM image, they could have different stackings and therefore different properties. I relate this to the observations in Fig. 4.11 where two different final behaviors (panel (d)) occurred for two identically looking DTs (panel (c)) coming from two identically looking CTs (panel (a)).

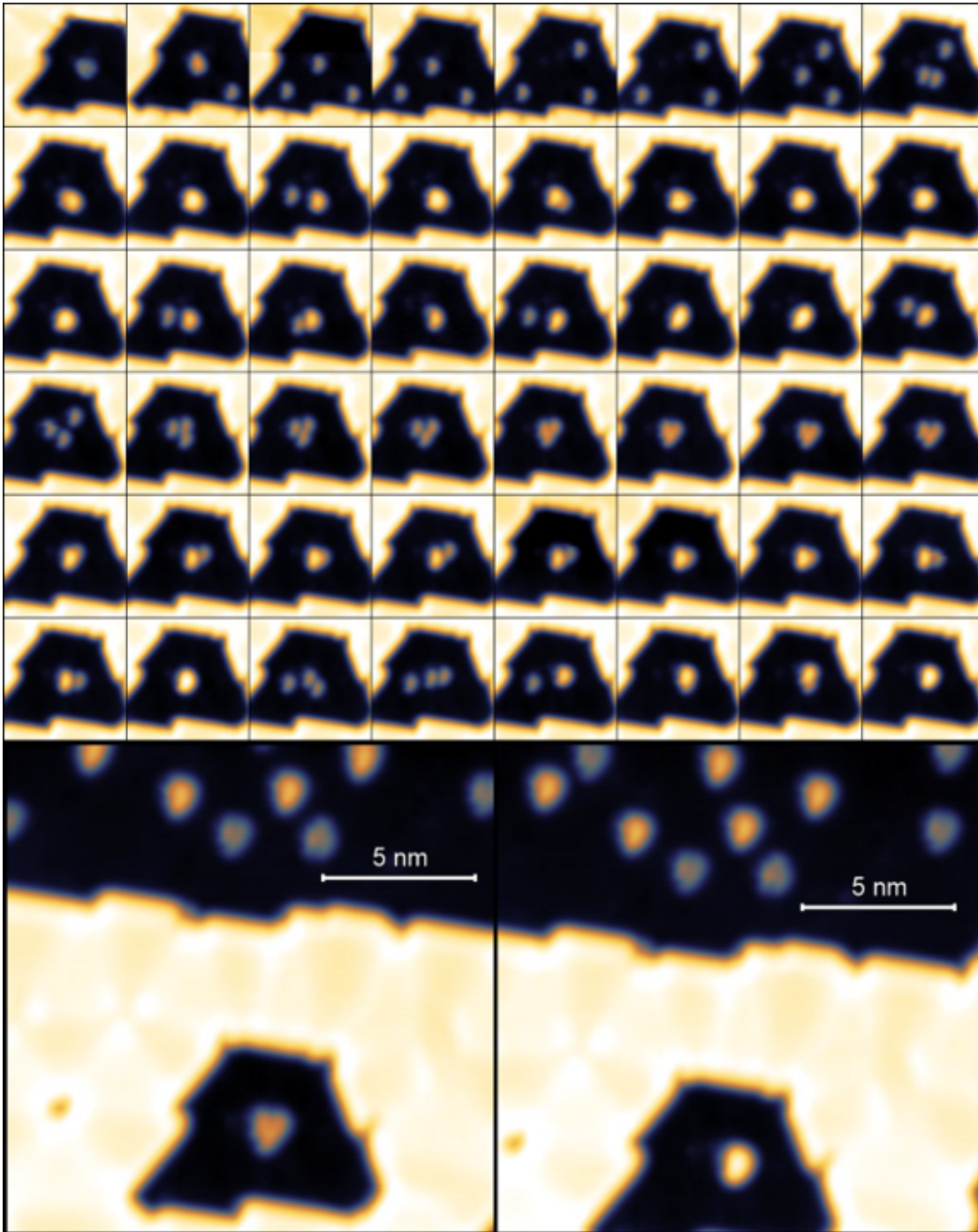


Figure 4.17: Disassembling a cluster via atom manipulation. Series of constant-current STM measurements taken between atom manipulation experiments disassembling a cluster inside a vacancy island. The last two panels show a larger view to compare the artificially created trimers with natural ones. (General measurement parameters: $U = +5$ mV, $I = 2$ nA, $T = 4$ K, **(all)** Cr bulk tip. General atom manipulation parameters between images: $U = +1 - +5$ mV, $I = 70 - 90$ nA)

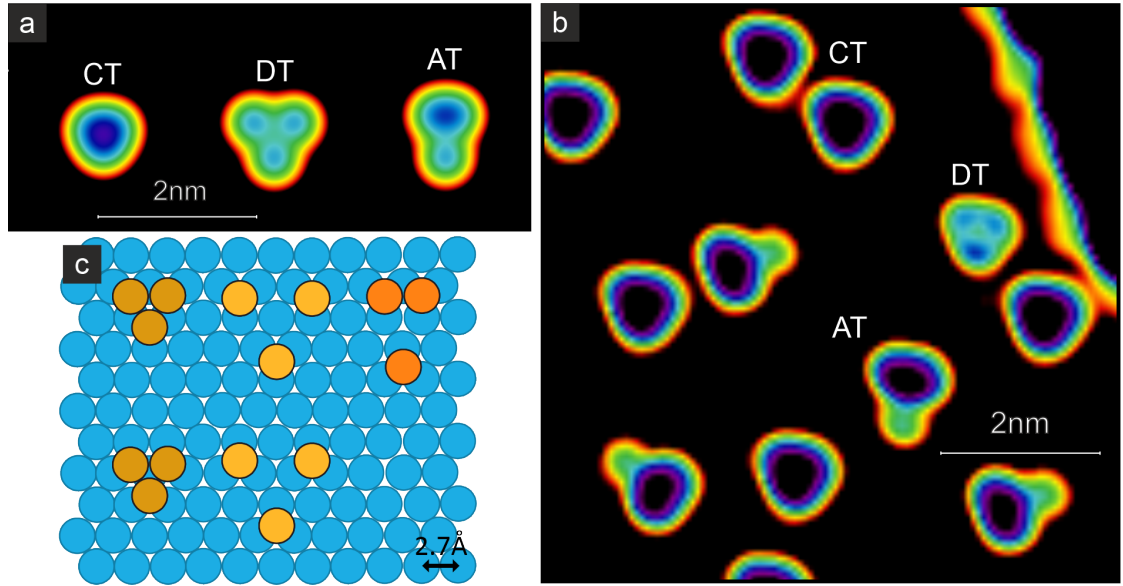


Figure 4.18: Trimer simulations and structural model. (a) Constant-height S-orbital STM simulation of the atomic structures in panel (c). (b) Constant-current STM image displaying the three different types of trimers for comparison. (c) Structural atomic arrangement of the simulations in panel (a). (Measurement parameters: (b) $U = +10$ mV, $I = 1$ nA, $T = 4$ K, Cr bulk tip)

To include the cluster stacking and behavior into the structural model, I analyzed in more detail the switching behavior itself. In Fig. 4.19 (a) it can be seen how differently stacked CTs (CT and CT*) would travel different paths (indicated by roman numerals) to arrive to differently stacked DTs (DT and DT*). All these paths except number I would create a measurable center of mass movement when switching. This center of mass movement is represented by green and red dots in Fig. 4.19 (a); green dots indicate the starting center of mass of the trimer and red dots indicate the final center of mass of the trimer after the switching. The suggested paths in this figure are just exemplary routes for the atoms to move and are not suggested to occur exactly like that.

Fig. 4.19 (b) and (c) show close-ups from Fig. 4.11 (a) and (c) in which two clusters switch from Compact Trimers to stable Dilute Trimers, one Asymmetric Trimer switches to an unstable Dilute Trimer, and a stable Dilute trimer remains stable. If we use the original stable DT in Fig. 4.19 (b) as a system of reference placing a triangle over it, we can place another triangle over one of the CTs and see if the cluster moves with respect to its original position in Fig. 4.19 (b). What we observe is that there is no change in position for the trimer during the switching. This means that the observed switching is the one described by path I, i.e. CT→DT. That also means that the other CT stacking (CT*) must give rise to the other DT stacking (DT*), i.e. path IV, CT*→DT*. We observe that the lower left DT in panel (c) is stable while measuring, while the one

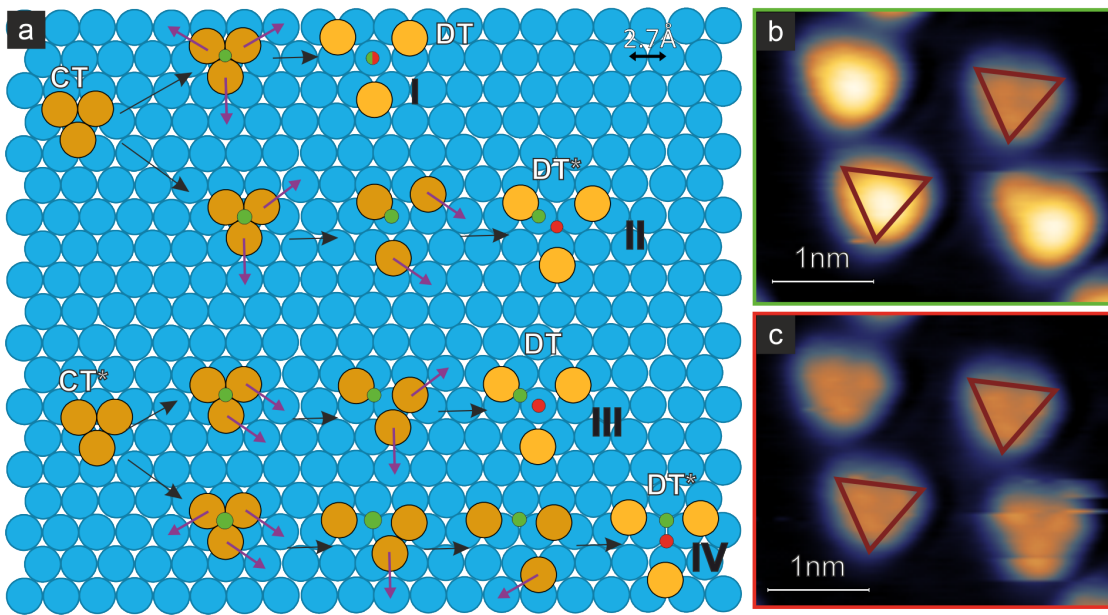


Figure 4.19: Trimer potential switching paths and center of mass analysis. (a) Possible paths for both CT stackings to become both DT types indicating atom movements over bridge sites. (b) Constant-current STM close-up from Fig. 4.11 (a). (c) Constant-current STM close-up from Fig. 4.11 (c). (Measurement parameters: (b and c) $U = +50$ mV, $I = 100$ pA, $T = 80$ K, Cr bulk tip.)

to its right is unstable (its atoms move while being scanned). This allows us to identify DTs as stable trimers, and DTs* as unstable ones, so we can characterize them based on their behavior. Finally, as all ATs become unstable DTs, that means they all become DT*.

To crosscheck this result I analyzed in detail the movement of the atoms forming the unstable dilute clusters. Assuming that the atom movement happens over bridge sites and away from the center to avoid forming CTs again, the directions in which the atoms could jump in the different dilute clusters depend on the stacking, as shown in Fig. 4.20 (a). In this panel it is also possible to see that the DT has two equivalent jumping possibilities for each atom, while the DT* has just one. In Fig. 4.20 (b) a stable dilute cluster and an unstable one are shown. The arrows superimposed over the unstable one indicate the directions in which its atoms move. Comparing with Fig. 4.20 (a) we see that the unstable dilute cluster must be the DT*. This is exactly what is expected after the previous "center of mass" analysis.

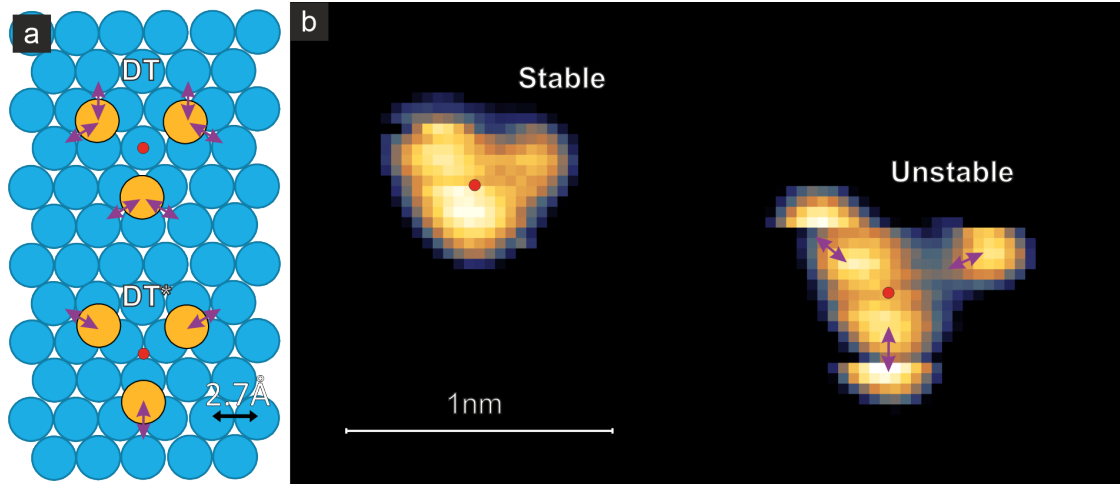


Figure 4.20: Unstable DT atomic movement analysis. (a) Possible atomic jumps away from the cluster center through bridge sites for both DT stackings. (b) Constant-current STM image exhibiting a stable DT and an unstable DT with the observed atomic jumps marked with purple arrows. (Measurement parameters: (b) $U = +50$ mV, $I = 1$ nA, $T = 80$ K, Cr bulk tip.)

With this information the proposed model in Fig. 4.18 can be improved to include the clusters' edge type, switching and stability. This final structural-behavioral model is shown in Fig. 4.21.

As discussed at the end of section 4.6.1, the existence of two stackings for the clusters manifests the leading role of the island-pointing-direction in the system. We know that certain trimer-pointing-direction is more stable than the other one. Then, as both

stackings are observed, it means that both edge types occur (see Fig. 4.16). This is contrary to previously observed systems, where the edge type is the fixed parameter and the other ones vary.

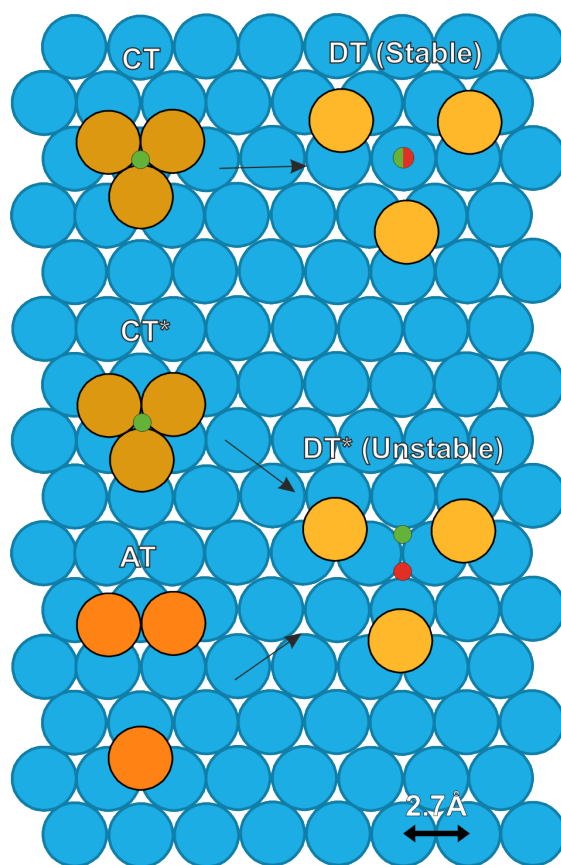


Figure 4.21: Complete structural-behavioral cluster model.

4.6.5 Cluster magnetism

To complete the cluster characterization I attempted to obtain magnetic information about them. I did this by two different experiments and none of them yielded results. Still, the absence of results is the foundation for the proposed magnetic state for the clusters that I will discuss at the end of this section.

The experiments performed were:

- SP-STM imaging
- Spin polarized telegraph noise measurements

SP-STM imaging is utilized the same way it is used in sections 4.4.2 and 4.5.2. The idea being that if clusters had differently oriented spins for each of their atoms, they should give rise to different contrasts while imaging with SP-STM. This is similar to the Néel state discussed in the above-mentioned sections. Different magnetic contrasts were not observed between atoms in the same cluster.

When a constant spin orientation can not be imaged, the possibility of a super-paramagnetic state in which the spins of the individual atoms change between different orientations is proposed [74]. I studied that possibility trying to measure the current changes that would appear from the spin configuration changes. The working principle behind this experiment is that if the SP-STM tip is positioned over a magnetic atom, the height at which the tip remains is dependent on the relative tip-sample spin orientation. If the spin orientation of the atom in the cluster is changing between different orientations, the tip should move up and down when the change happens depending on the projection of the sample spin on the tip spin. Additionally, the number of levels observed in the fluctuations could give us information about the amount of possible spin orientations. Again, the experiment yielded no results, i.e. no height jumps were observed while stabilized over the atoms. This could be related to the jumps happening at a higher rate than the electronics could measure (several times per ms), or not happening at all.

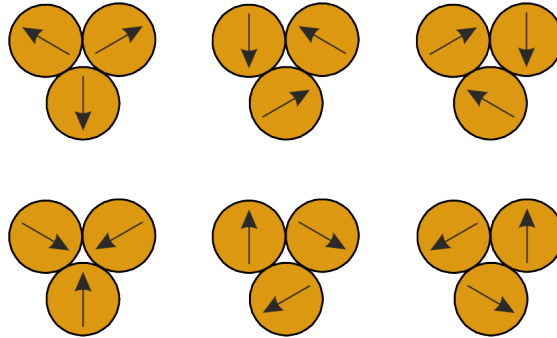


Figure 4.22: Proposed spin configurations for a Mn trimer. At the measured temperatures, the magnetic state is understood to be constantly fluctuating between these states.

4.7 Low coverage sample: Proto-islands

To better understand the cluster phase and its relation with the reconstructed phase, a sample with a coverage of 0.05 monolayers was prepared. This preparation reveals the existence of the cluster phase at these low densities, in contrast to a possible single atom phase at low coverages.

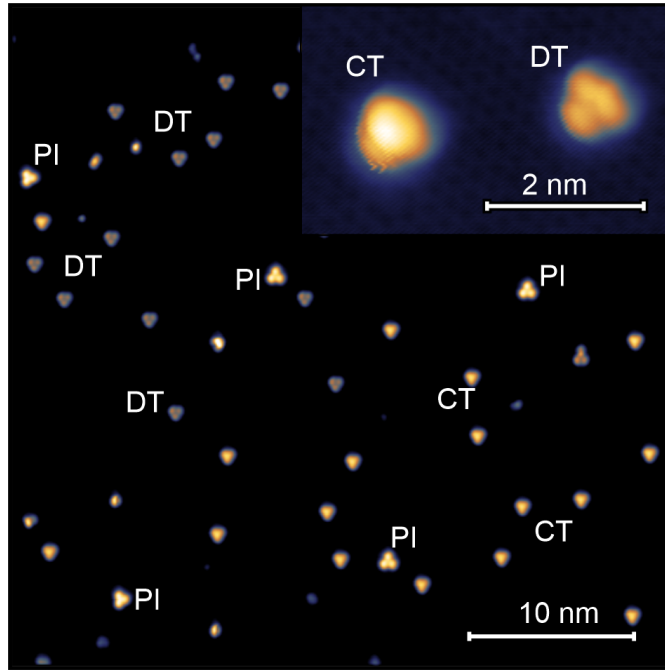


Figure 4.23: Low coverage sample. (Measurement parameters: $U = +3$ mV, $I = 1$ nA, $T = 4$ K, inset: $U = +20$ mV, $I = 1$ nA, $T = 4$ K, **(all)** Cr bulk tip)

Fig. 4.23 shows the cluster phase existing without any extended Mn layer present. In the figure it is also possible to see objects not previously found that I call Proto-Islands (PI). These objects are triangular three-lobed structures apparently similar to DTs but bigger, seemingly higher, and rotated with respect to the common cluster orientation. If we consider the CTs and DTs to be 0° rotated, some of these objects appear to be 30° rotated while others are 60° rotated.

Based on this rotational distinction, I identify two main types of Proto-Islands. In Fig. 4.24 (a) and (b) a closer look to these PIs is shown. If we take into account that clusters move at room temperature as discussed in section 4.3, we can imagine the PIs to be formed by three clusters each, the same way three atoms give rise to a cluster. Combining three trimers in different ways panels (c) and (d) in Fig. 4.24 can be obtained. These atomic configurations keep the triangular symmetries of the PIs and make them point in the observed directions.

To check this model constant-height STM simulations were performed (Fig. 4.24 (e) and (f)) and compared with the observed structures. Experimentally it is found that the area occupied by the Proto-Island in panel (b) is larger than the area of the Proto-Island in panel (a). The areal ratio between them is $b/a = 1.15$. If this same comparison is done for the simulated proto-islands in (e) and (f), it is found that $f/e = 1.11$. In the magni-

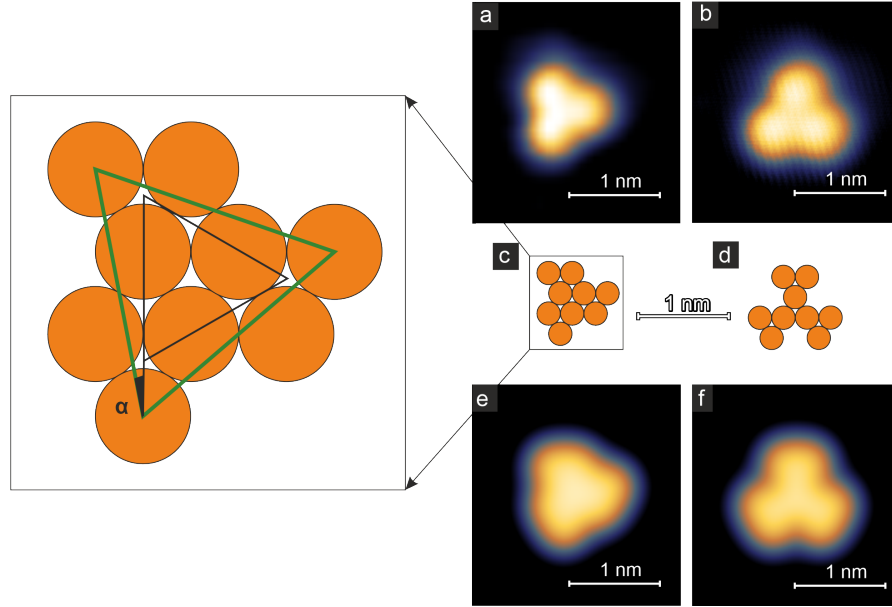


Figure 4.24: Proto-Islands analysis and model. **a,b** Constant-current STM image of the two different types of Proto-Islands. **c,d** Atomic structure models for the Proto-Islands in **a** and **b**. **e, f** Constant-height STM simulations of the atomic structures in **c** and **d**. (Measurement parameters: **(a)** $U = +3$ mV, $I = 1$ nA, $T = 4$ K, **(b)** $U = +5$ mV, $I = 1$ nA, $T = 4$ K (**all**) Cr bulk tip)

fication of panel (c) in 4.24 we see that if we join the centers of the three trimers used to create the PI, a black triangle with sides running perpendicular to the close-packed rows is obtained. On the other hand, if we join the outermost atoms of each trimer, i.e. the ones further apart from the center, a green triangle slightly rotated by 13.26° with respect to the first one is obtained. In STM we observe the edges of the PIs, but no atomic resolution of their insides was acquired. It is reasonable to understand that the green triangle in the enlarged view of Fig. 4.24 (c) would be the one measured. When characterizing this rotation experimentally, an angle of 13.5° is obtained reinforcing the proposed model.

After analyzing the Proto-Islands I propose that they are the starting stage of the reconstructed-phase, hence their chosen name. They would nucleate at defects to later act as nucleation points themselves for the reconstructed phase. That would also explain why they are not observed once the reconstructed phase has appeared, as they are already surrounded by other Mn atoms

4.8 Mn/Ir(111) conclusions

Mn/Ir(111) is a complex system that exhibits three structural phases with distinct properties. These are: the pseudomorphic phase, that appears when the first monolayer is completed. The reconstructed phase, that is present at sub-monolayer coverages. And the cluster phase, that coexists with the reconstructed phase and also appears alone at extremely low coverages. The Mn pseudomorphic phase keeps the atomic structure of the underlying Ir and exhibits the Néel state as its ground state. The Mn reconstructed phase displays a Moiré-like triangular reconstruction generated by a 6% to 7% expansion of the Mn layer with respect to the Ir below. Its magnetic ground state is the Néel state, as in the pseudomorphic case. The Mn cluster phase is formed by monodisperse self-assembled Mn trimers. These trimers are mobile at room temperature. When their density increases above a certain threshold they form the reconstructed phase. At temperatures between 4 K and 80 K the trimers become immobile and appear in three different apparent configurations: Compact Trimers (CTs), Dilute Trimers (DTs) and Asymmetric Trimers (ATs). CTs and ATs can be switched unidirectionally to DTs when interacting with the STM tip. The clusters' behavior allowed to identify a stacking difference between different types of clusters and permitted the creation of a full structural-behavioral cluster model. The magnetic ground state of the clusters has not been observed but I propose it to be a super-paramagnetic antiferromagnetic configuration where the spins are in plane 120° rotated between atoms and fluctuate coherently between their different possible orientations.

The existence of the clusters is proposed to have its origin in the structural expansion of the Mn atoms found in the reconstructed Mn layer phase. This would make trimer configurations more stable in contrast to configurations with more atoms that would be forced further away from hollow sites. The cluster-cluster repulsion is not completely understood, and three possibilities are proposed: The first one is again the structural expansion of the Mn atoms. The second one is the existence of dipolar moments in the clusters that could result in repelling each other. The third one is the presence of electron standing waves that could generate a potential barrier around the clusters. Finally, the coexistence of the cluster phase and the reconstructed phase seems to arise from the maximum permitted cluster density. When the cluster density grows locally above a certain threshold, the reconstructed phase becomes energetically more favorable. Then a section of the reconstructed phase is grown, decreasing the density of the cluster phase in the process and generating the coexistence.

5 Growth, magnetism and superconductivity of Cr/Nb(110)

"[...] But the basic fact is that all of these theories are likely correct at some degree, and each played off each other in a synergistic orgy of destruction."

— Mike Duncan, The History of Rome

In this chapter I will discuss about the first, the second and briefly the third layer of Cr on Nb(110). I will start by analyzing the structure of the layers. Then I will continue with the analysis of their magnetic and superconducting properties.

5.1 Introduction

Topological superconductivity has been investigated in the last years by focusing on hybrid systems consisting of semiconductor-superconductor [75], topological insulator-superconductor [76], magnet-superconductor [77], [78], [79] and in particular, antiferromagnet-superconductor [5], [80]. In the case of the magnet-superconductor hybrid systems (MSHs), the magnetic moments provided by the magnetic layer break the time-reversal symmetry, which along with the particle-hole symmetry of the system let us classify them topologically as class D materials (see table 2.1). The publication by Bazarnik *et al.* [5] predicts theoretically the existence of a gapless topological superconducting phase, the topological nodal-point superconducting (TNPSC) phase [81], [82], [83], [84], [85] for MSHs with AFM ordering. This topological phase is realized in the same publication by a monolayer of Mn on Nb(110).

The atomic structure of the magnetic layer on the substrate is known to play a role for the magnetic ground state of the system, as discussed in Chapter 4, section 4.1. Furthermore, the magnetic ground state can be modified by effects such as edge anisotropy or different adsorption sites. These magnetic changes can lead in certain cases to a quenching of the magnetic moments [86].

Here I report on the presence of a TNPSC phase in the first layer of Cr on Nb(110). Lateral variations of the structure lead to topological phase transitions, in and out of

the topologically trivial phase.

5.2 Cr/Nb(110): Growth and structural analysis

The growth of different Cr layers on Nb(110) can be seen as the discrete transformation of the Nb(110) structure into the Cr(110) one. Both materials are bcc crystals, and when Cr is evaporated on Nb(110) it grows following the (110) facet. The 12% difference between the unit cell sizes ($a_{[001]} = 330$ pm and $b_{[1\bar{1}0]} = 467$ pm for Nb(110) versus $a_{[001]} = 291$ pm and $b_{[1\bar{1}0]} = 411$ pm) leads to strain within the evaporated layers. This difference also results in different surface atom densities: 12.98 atoms/nm² for the Nb surface and 16.7 atoms/nm² for the Cr one. The strain is relaxed forming different types of atomic structures bridging the gap between the Nb unit cell and the Cr(110) bulk unit cell. All observed structural phases of the first three layers will be discussed in the following.

5.2.1 Cr first layer

When Cr is deposited onto a Nb crystal in the $T \approx 450$ K to $T = 300$ K range, the Cr monolayer grows in a step-flow growth fashion, as shown in Fig. 5.1 (a). When the size of the terraces is large enough, isolated islands can also be found, such as the one in Fig. 5.1 (c). These islands are characterized by elongated edges along the [001] direction (see Fig. 5.1 (c)).

Fig. 5.1 (b) shows an atomic resolution image of the first layer of Cr. The analysis of the atomic structure reveals the same unit cell as the Nb below, i.e. bcc (110) with 330 pm lattice constant. This means that the first layer of Cr on Nb(110) grows pseudomorphically. This is shown again in more detail in Fig. 5.1 (d). Here, the atom manipulation image reveals the structure of the first Cr layer. The symmetries and periods revealed by the measurement confirm the pseudomorphic growth.

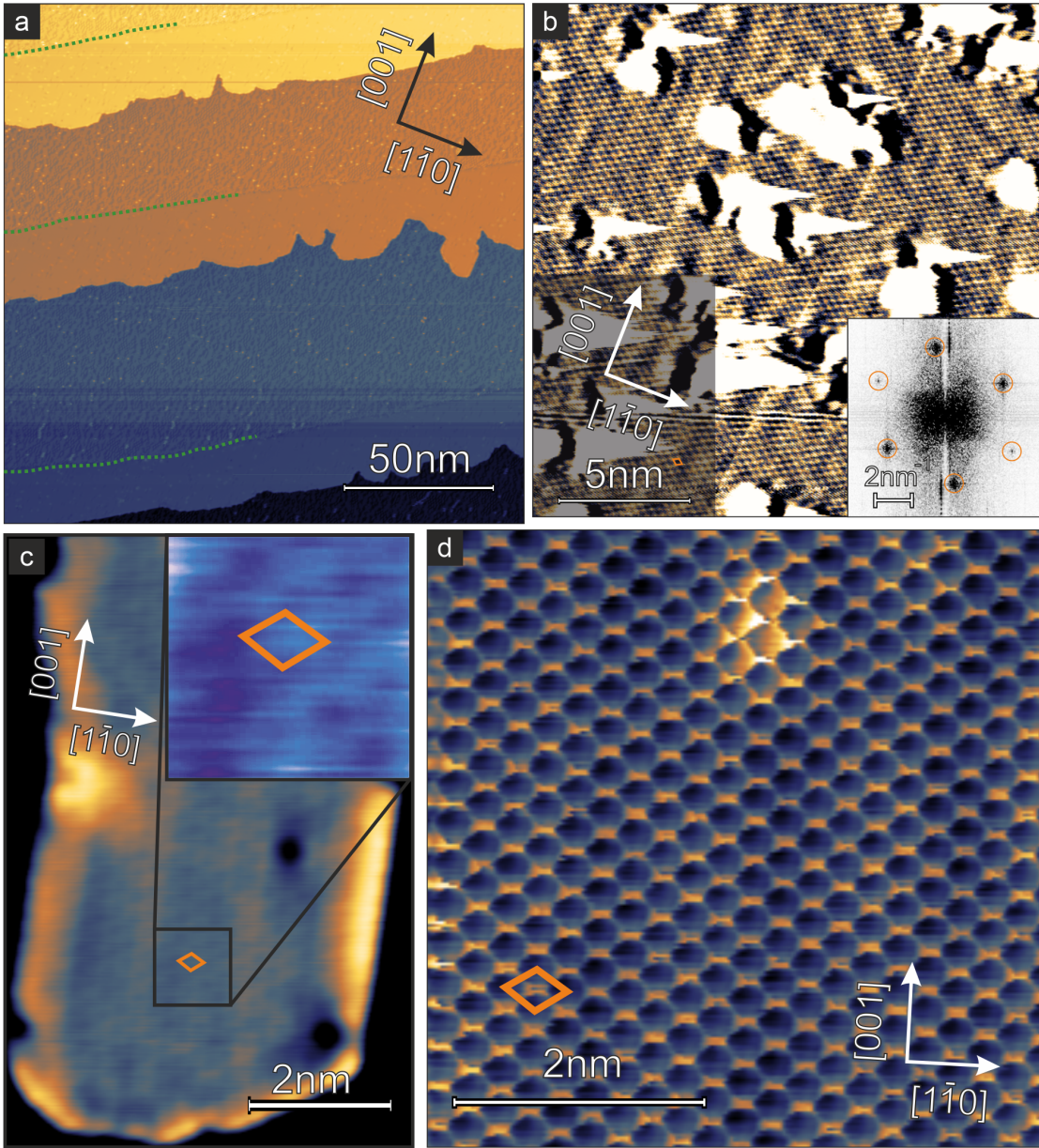


Figure 5.1: First layer growth and atomic structure. (a) Constant-current STM image of a sub-monolayer Cr/Nb(110) preparation exhibiting step-flow growth. Green dotted lines indicate the location of the buried step edges. (b) Current channel of a constant-current STM measurement showing an extended patch of first layer Cr with atomic resolution. Inset: FFT of panel b. (c) Constant-current STM close-up of a first layer Cr island with atomic resolution (better seen in inset). (d) Constant-current STM atom manipulation image of Cr first layer showing the bcc (110) symmetry. (Measurement parameters: (a) $U = +5$ mV, $I = 7$ nA, (b) $U = +1$ mV, $I = 9.8$ nA, (c) $U = +5$ mV, $I = 1.1$ nA, (d) $U = +1$ mV, $I = 90.8$ nA, (all) $T = 4$ K).

5.2.2 Cr second layer

The second layer Cr on Nb(110) starts growing before the first layer fully covers the Nb substrate. The second layer grows in islands with no clearly defined shape. This layer often reaches the edges of the first layer film. In these cases, the second layer's growth is just limited by the absence of first layer to grow over. This results in steps from second layer to Nb as marked with cyan ellipses in Fig. 5.2 (a).

The second layer Cr islands grow in a reconstructed fashion. Three different *reconstruction* types and two intermediate adatom *phases* are identified depending on the structure of the Cr atoms. These are named:

- 1D *Reconstruction* (1DR) (Fig. 5.2(b)).
- Train Track adatom *Phase* (TTP) (Fig. 5.2(c)).
- Absorbed Train Track *Reconstruction* (ATTR) (Fig. 5.2(d)).
- Music Box adatom *Phase* (MBP) (Fig. 5.2(e)).
- 2D *Reconstruction* (2DR) (Fig. 5.2(f)).

The most prominent and well understood structures are the 1DR and the 2DR. Both of them can be modeled as Moiré patterns. In particular, the 1DR can be modeled as a *one-dimensional Moiré pattern*, and the 2DR as a *bi-dimensional arbitrary strain Moiré pattern*, following the nomenclature in 3.3.1. These two reconstructions will be discussed next, while the intermediate ones are explained in detail in the Appendix. All phases have been observed in sample preparations with warm substrates, i.e. when Cr was evaporated from eight to fifteen minutes after the last flash. All of them can coexist in the same sample. These reconstructions and phases occur as the Cr second layer increases its surface atom density approaching the Cr(110) bulk one.

1D Reconstruction

The 1DR of the second Cr/Nb(110) layer appears as a series of lines running along the $[1\bar{1}0]$ direction. The period of the lines is 2040 pm on average, but it can vary locally. The reconstruction lines sometimes deviate from the $[1\bar{1}0]$ direction locally by a few degrees. Both of these small variations can be observed in Fig. 5.3 (a). These variations reveal local strain changes in the layer. The Cr layer is observed to be pseudomorphic along the $[1\bar{1}0]$ direction (Fig. 5.3 (b)). This allows the modeling of the layer as a Moiré pattern using eq. 3.4 ($\delta p = \frac{p^2}{2d_m \pm p}$) along the $[001]$ direction. With this approach it is found that the layer is either expanded by 8.8% or compressed by 7.5%. For this the

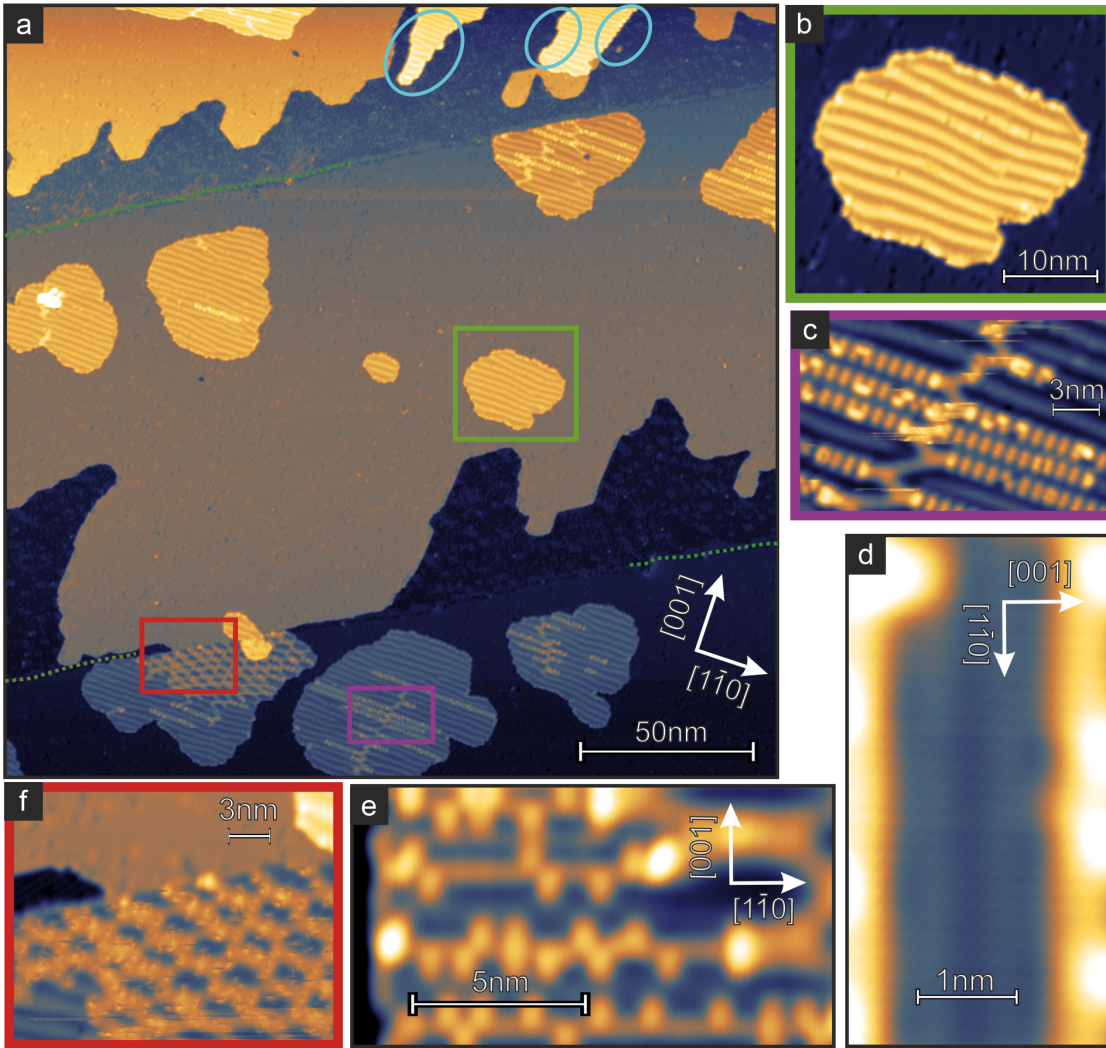


Figure 5.2: Second layer growth and its different phases. (a) Constant-current STM image of a Cr/Nb(110) preparation exhibiting both first and second layers. Green dotted lines indicate the location of the buried step edges. (b) Zoom-in in panel (a) showing a close-up of the 1D reconstruction. (c) Zoom-in in panel (a) showing a close-up of the train track adatom phase. (d) Constant-current STM close-up of the absorbed train track reconstruction. (e) Constant-current STM close-up of the music box adatom phase. (f) Zoom-in in panel (a) showing a close-up of the 2D reconstruction. (Measurement parameters: (a), (b), (c), (f) $U = +10$ mV, $I = 7.6$ nA, $T = 4$ K, (d), (e) $U = +5$ mV, $I = 2.5$ nA, $T = 4$ K).

average periodicity of the reconstruction ($d_m = 2040$ pm) and the distance between atoms of the bottom layer in the $[001]$ direction ($p = 330$ pm) are used.

Atomic resolution measurements of the reconstruction such as Fig. 5.3 (b) reveal that the layer is *compressed* along the $[001]$ direction by roughly 8% , confirming one of the Moiré cases. In these images it is also found that the layer is pseudomorphic along the $[1\bar{1}0]$ direction, i.e. the atomic distances along the $[1\bar{1}0]$ direction are the same ones as for Nb(110). This supports the one-dimensional Moiré characterization.

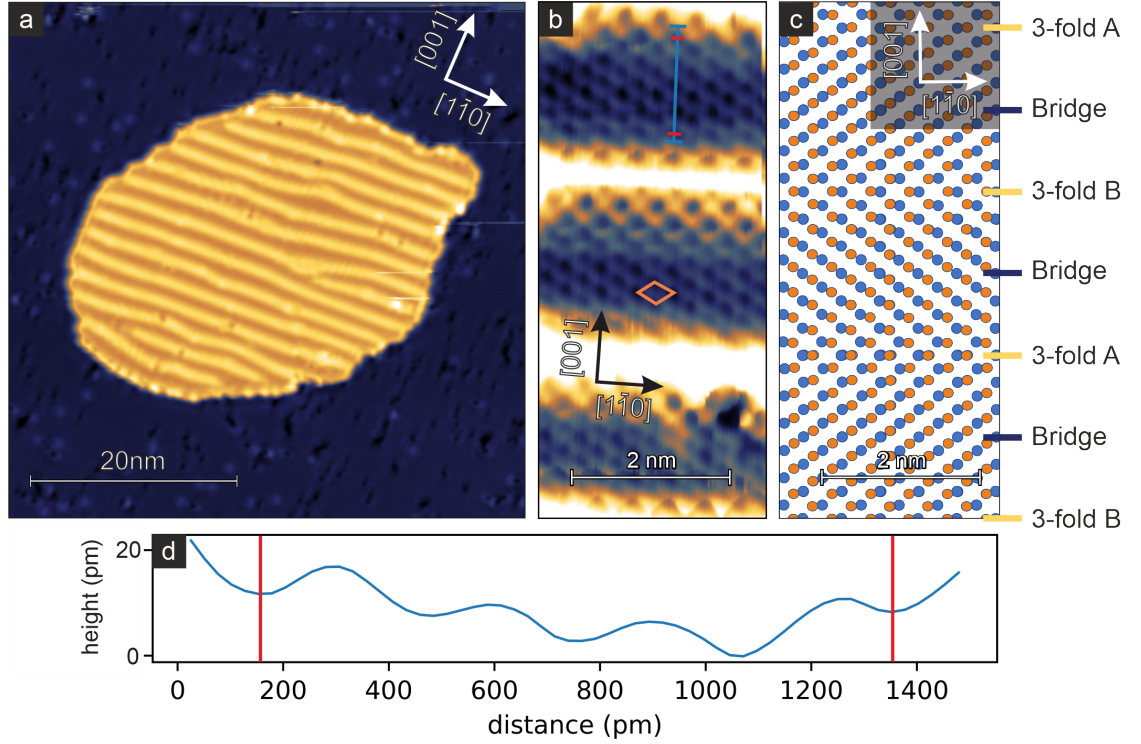


Figure 5.3: 1DR structure and Moiré model. (a) Constant-current STM image of a second layer Cr island exhibiting the one-dimensional reconstruction. It can be seen how the reconstruction lines run roughly perpendicular to the $[001]$ direction. (b) Constant-current STM close up of the one-dimensional reconstruction with atomic resolution. The orange diamond indicates the atomic unit cell and the blue line indicates the line profile shown in panel (d). (c) Atomistic Moiré model of the one-dimensional reconstruction. The blue circles represent the first layer Cr atoms with the bcc (110) symmetry. The orange circles represent the second layer Cr atoms with the 7.5% compression along the $[001]$ direction. The orange atoms are shifted along the $[1\bar{1}0]$ direction towards the three-fold hollow sites. (d) Line profile obtained along the blue line in panel (b). The distance between the points marked in red is approximately 1.2 nm versus the 1.32 nm expected for Nb, revealing the Cr compression. (Measurement parameters: (a) $U = +5$ mV, $I = 7.6$ nA, $T = 4$ K, (b) $U = +1$ mV, $I = 94$ nA, $T = 4$ K).

Once the 1DR is confirmed to be a compressed Moiré-like structure, a model is created in Fig. 5.3 (c). In this schematic model, blue atoms represent the bottom pseudomor-

phic Cr layer and orange atoms represent the top reconstructed Cr layer. In the model one can observe how the atomic rows along the [001] direction go from one three-fold hollow site (A) to bridge sites, to the other three-fold hollow site (B). This is taken into account by eq. 3.4. Knowing the compression the atom density of this reconstruction can be calculated, which is 14.12 atoms/nm². This model is a good approximation to the structure of the layer, but the atoms are additionally expected to relax laterally.

2D reconstruction

When more Cr is evaporated onto the 1DR, different intermediate phases appear (see Appendix 6) until the final structural reconstruction takes place. This is the 2DR. This reconstruction looks like a distorted hexagonal superstructure with high variability in size and direction (see Fig. 5.4 (a)). On the borders of the reconstruction it connects with either the 1DR, the ATTR or the MBR, sometimes all of them as shown in Fig. 5.4 (b).

This reconstruction can be characterized as a Moiré pattern, in particular as a bi-dimensional arbitrary strain Moiré pattern. To characterize it as such, eq. 3.3 ($\delta p = \frac{p^2}{d \pm p}$) is used. This time it is applied along the [001] and the $[1\bar{1}0]$ direction. For these directions, the average measured values of d and p are: $d_{[001]} = 2760$ pm, $p_{[001]} = 330$ pm, and $d_{[1\bar{1}0]} = 5940$ pm, $p_{[1\bar{1}0]} = 467$ pm. It is important to note that the high variability of the d values makes this general model a good first approximation, but may vary significantly locally. This analysis generates four possible compression-expansion combinations. From these options, just the compression-compression case increases the density towards the Cr(110) bulk one. This compression-compression case is confirmed by atomic resolution measurements. So the 2DR is characterized to be compressed along the $[1\bar{1}0]$ by 7%, and along the [001] direction by 11%, resulting in a surface atom density of 15.63 atoms/nm². With this information, a model is created in Fig. 5.4 (d). In both panels (c) and (d) the different regions of the reconstruction are indicated. Red ellipses indicate the on-top positions of the reconstruction, green ellipses represent the bridge sites, and the black ellipse indicates the four-fold hollow sites.

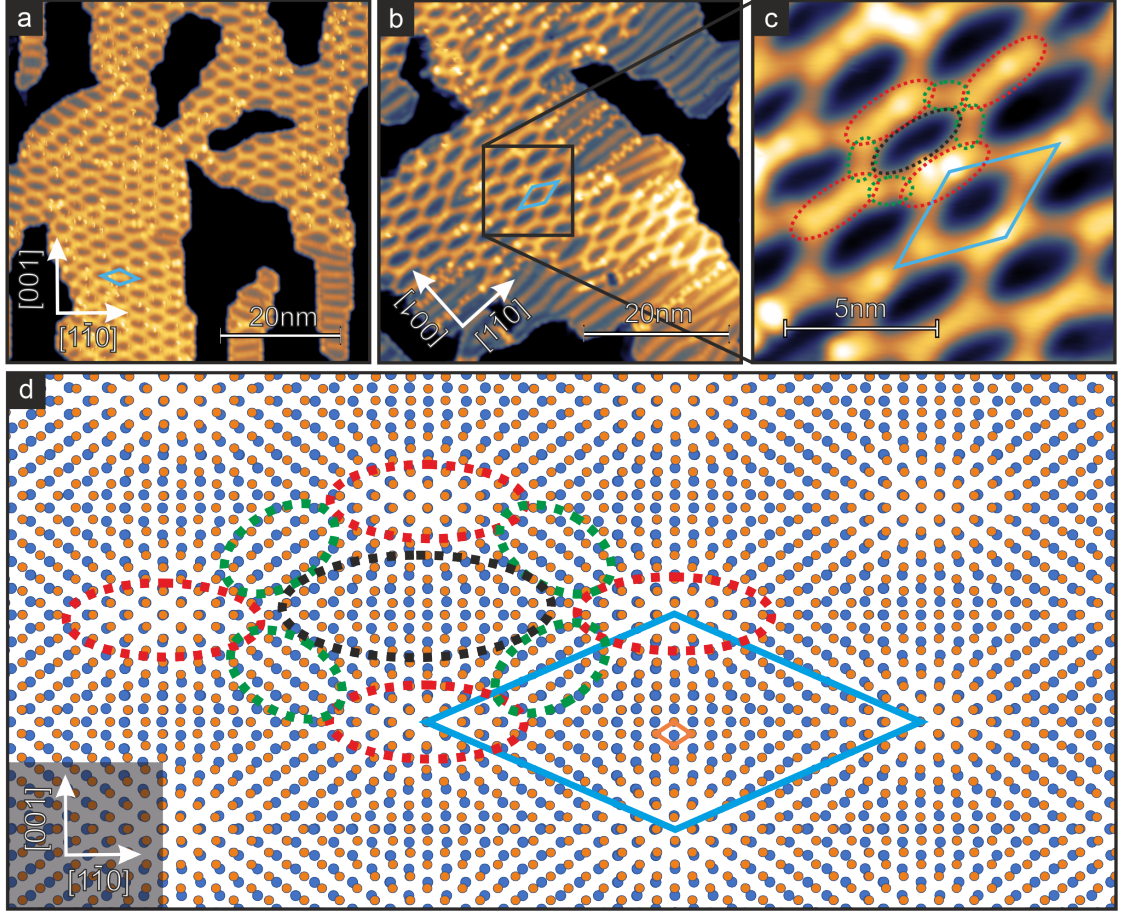


Figure 5.4: 2DR overview. (a) Constant-current STM overview of a second layer Cr region mostly populated by the 2DR. The unit cell of the 2DR is indicated in cyan. The bright moving particles on top of the reconstruction are hydrogen impurities. (b) Constant-current STM image of a second layer Cr region where different borders of the 2DR connect to both the 1DR and the MBP. The unit cell of the 2DR is indicated in cyan. (c) Zoom in panel (b). The same unit cell of panel (b) is indicated in cyan. The dotted ellipses indicate the different parts of the reconstruction and are color-coded the same way as in panel (d). (d) Atomistic Moiré model of the two dimensional reconstruction. The atomic unit cell is indicated in orange, while the Moiré unit cell is indicated in cyan. The blue circles represent the first layer Cr atoms with the bcc (110) symmetry. The orange circles represent the second layer Cr atoms. Red ellipses indicate the on-top positions of the reconstruction, green ellipses represent the bridge sites, and the black ellipse indicates the four-fold hollow sites. (Measurement parameters: (a) $U = +2$ mV, $I = 3.5$ nA, $T = 4$ K, (b) and (c) $U = +10$ mV, $I = 1.5$ nA, $T = 4$ K.

5.2.3 Cr third layer

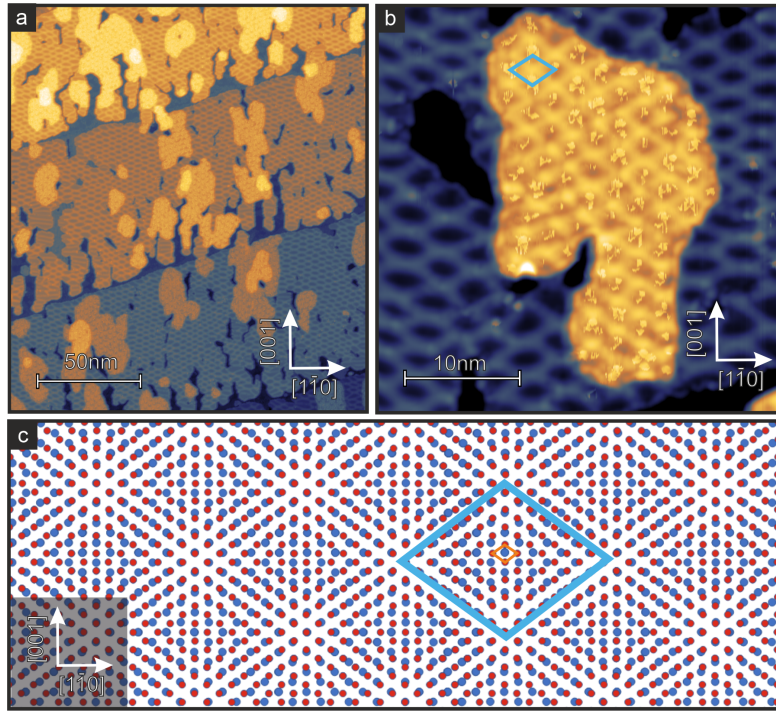


Figure 5.5: Third Cr layer reconstruction and model. (a) Constant-current STM overview image of a sample preparation with high second layer coverage and third layer islands. (b) Constant-current STM close-up of a third layer island exhibiting the third layer reconstruction. The unit cell of the reconstruction is indicated in cyan. Moving particles on top of the third layer are thought to be hydrogen atoms. (c) Atomistic Moiré model of the third layer reconstruction. The atomic unit cell is indicated in orange, while the Moiré unit cell is indicated in cyan. The blue circles represent the second layer Cr atoms with the bcc (110) symmetry. The red circles represent the third layer Cr atoms. (Measurement parameters: (a) $U = +2$ mV, $I = 3$ nA, $T = 4$ K, (b) $U = +2$ mV, $I = 4.5$ nA, $T = 4$ K).

Fig. 5.5 (a) shows how atoms deposited on the 2DR in the second layer give rise to the third Cr layer, in contrast to the previous adatom phases.

The third layer of Cr on Nb(110) exhibits once again a Moiré-like reconstruction, so it can be analyzed the same way as the 1DR and the 2DR were. When doing so, eq. 3.3 is applied in two dimensions, like for the 2DR case. The measured values for d along the $[001]$ and the $[1\bar{1}0]$ directions are: $d_{[001]} = 2300$ pm and $d_{[1\bar{1}0]} = 4140$ pm. These distances reveal the bcc(110) symmetry. As discussed in section 3.3.1, this means that both layers creating the Moiré pattern have the bcc(110) symmetry with different lattice constants. Additionally, as just one Moiré pattern is observed, there is exactly one

interlayer lattice mismatch from the Nb substrate to the Cr third layer. This would not be observed if there would be a bcc(110) layer on top of the 2DR, which would result in a combination of Moirés, which means that one of the layers forming the Moiré pattern must have the Nb(110) unit cell. If eq. 3.3 is solved for the observed reconstruction and the Nb(110) unit cell, one obtains that the other layer must be compressed by roughly 12% in both the $[001]$ and the $[1\bar{1}0]$ directions, i.e. it must have the Cr(110) structure.

To determine exactly which layers originate the Moiré pattern, all possibilities are considered: The first possibility is that the reconstruction appears in the interface between Nb and Cr first layer (Interface A in Fig. 5.6). This is unlikely, as the first layer is understood to remain pseudomorphic when the second layer grows on top with the different structural phases. So it is reasonable to assume that it remains stable when a third layer is added. The second possibility is that the reconstruction appears at the interface between Cr first layer and Cr second layer (Interface B in Fig. 5.6, highlighted in yellow). In this case, the Cr second layer would have to further compress from the 2DR to the Cr(110) bulk structure. This is the most probable situation. Finally, the third possibility is that the reconstruction appears at the interface between Cr second layer and Cr third layer (Interface C in Fig. 5.6). For that to occur, the second layer should be pseudomorphic, which means it would have to decrease its density from the 2DR instead of increasing it. This is highly unlikely.

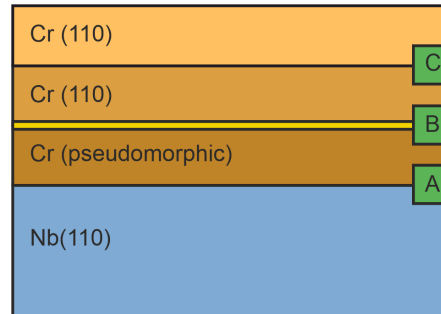


Figure 5.6: Interface origin of the Cr third layer reconstruction.

Therefore the third Cr layer structure can be understood as a Moiré pattern generated between the first and second layers of Cr. When the third layer starts growing, the second layer compresses by 12% along both axes with respect to the first layer below. Then, the third layer grows on top following the Moiré pattern below, also with the 12% compression, i.e. with the Cr(110) bulk structure. The atom densities of the third layer and the second layer below are therefore the ones of Cr(110) bulk: 16.7 atoms/nm². This Moiré pattern is exhibited in Fig. 5.5 (c), where the blue circles represent the first Cr layer with pseudomorphic growth, and the red circles represent the second Cr layer

atoms generating the Moiré pattern.

In reality, in a similar way as for the 1DR and 2DR, the Moiré pattern observed in the third layer exhibits local distortions. This means that the model is a first approximation to the whole structure of the layer, but may not be able to replicate precisely local structures.

5.3 Cr/Nb(110): Magnetism and superconductivity

The study of magnetism in the Cr/Nb(110) system has proven to be particularly challenging. The only magnetic state directly measured is the one of the pseudomorphic extended first Cr layer. And even this state exhibits extremely low corrugation and happened to be difficult to measure with Cr bulk tips, probably due to a small spin-polarization of the system or Nb contamination of the tip. Despite these complications addressing the magnetism of the system, several magnetism related phenomena can be discussed in the first and second monolayers of Cr on Nb(110). All the following data was measured with Cr bulk tips, sometimes with Nb clusters at the apex.

On the other hand, the superconducting properties of the sample were easier to measure. The interplay between superconductivity and magnetism leads to interesting topological phases and states such as topological nodal point superconductivity TNPSC, YSR bands and topologically protected edge states. But the apparent absence of magnetism for certain studied structures also results in interesting phenomena, like the recovery of superconductivity in higher layers or under certain constraints.

In this section I will discuss both magnetism and superconductivity.

5.3.1 Cr extended first layer

The magnetic and superconducting properties of the first layer of Cr on Nb(110) are comparable with the results of Bazarnik *et al.* [5]. They modeled a single layer of AFM material with bcc(110) symmetry in proximity to an s-wave superconductor. Their model predicts the existence of topological nodal points (TNP) in the superconducting band structure of the system. They predict the appearance of low energy edge modes along the FM and zigzag edges ([001] and $[1\bar{1}0]$ respectively in our case). This is confirmed in the same publication experimentally for the case of Mn/Nb(110). However, they claim that these predictions are general for AFM materials with bcc(110) symmetry in proximity to an s-wave superconductor, which is also the case for the first monolayer

of Cr on Nb(110).

Magnetism

The first layer of Cr on Nb(110) exhibits a $c(2 \times 2)$ AFM ground state (schematically depicted in Fig. 5.7 (c) inset). The structure of the Cr layer is the one of the underlying Nb(110) below, as discussed in section 5.2.1, which results in the appearance of the state as a row-like pattern when studied via SP-STM. This is shown in Fig. 5.7 (a), (b), (c) and (e). In panel (a) it is possible to see the FM rows of atoms along the [001] direction, highlighted in a section of the image via red and green lines. Different colors indicate opposite spin orientations of the magnetic moments of the sample. The magnetic contrast in the topography channel is very small, on the order of 0.5 pm to 1.5 pm when measured with low voltage (2 mV - 15 mV) and high current (3 nA - 10 nA). No higher corrugation than that was observed despite studying the system with different tips. Higher corrugation is obtained in the current channel with these same parameters, as shown in panels (b) and (c). The fact that the Cr first layer grows with straight edges along the [001] direction leads to FM edges. The less common, but still observed edges running along the close-packed rows are AFM edges.

In panel Fig. 5.7 (c) the current channel of a different first layer area is displayed. In the current channel it is easier to identify the ferromagnetic rows of the superstructure. The highly periodic nature of the structure makes the FFT analysis convenient to obtain their spatial frequency more precisely. Panel (d) shows the FFT of panel (c). The peaks corresponding to the magnetic corrugation are indicated via cyan circles. The FFT analysis reveals a periodicity of roughly 465 pm along the $[1\bar{1}0]$ direction, determining the structure as the already mentioned $c(2 \times 2)$ AFM superstructure. Panel (e) of Fig. 5.7 shows an image with atomic and magnetic resolution. The magnetic resolution appears as a slight increase in current in every other line along the [001] direction. This is better seen when a line profile is taken along the blue line in (e) (along the $[1\bar{1}0]$ direction), where panel (f) is obtained. Note that this line profile averages for almost 4 nm along the [001] direction to increase the signal to noise ratio of the measurement. In panel (f) each peak is separated from the next one by around 230 pm, i.e. atomic resolution, while high and low peaks alternate, as highlighted by the red and green lines that join every two peaks. This confirms with atomic resolution that the $c(2 \times 2)$ AFM superstructure is the magnetic ground state. This can be observed additionally in panel (g), where an FFT of the dotted rectangle in panel (e) has been calculated. Here it is possible to identify both the magnetic and atomic peaks of panel (e), highlighted in blue and orange respectively.

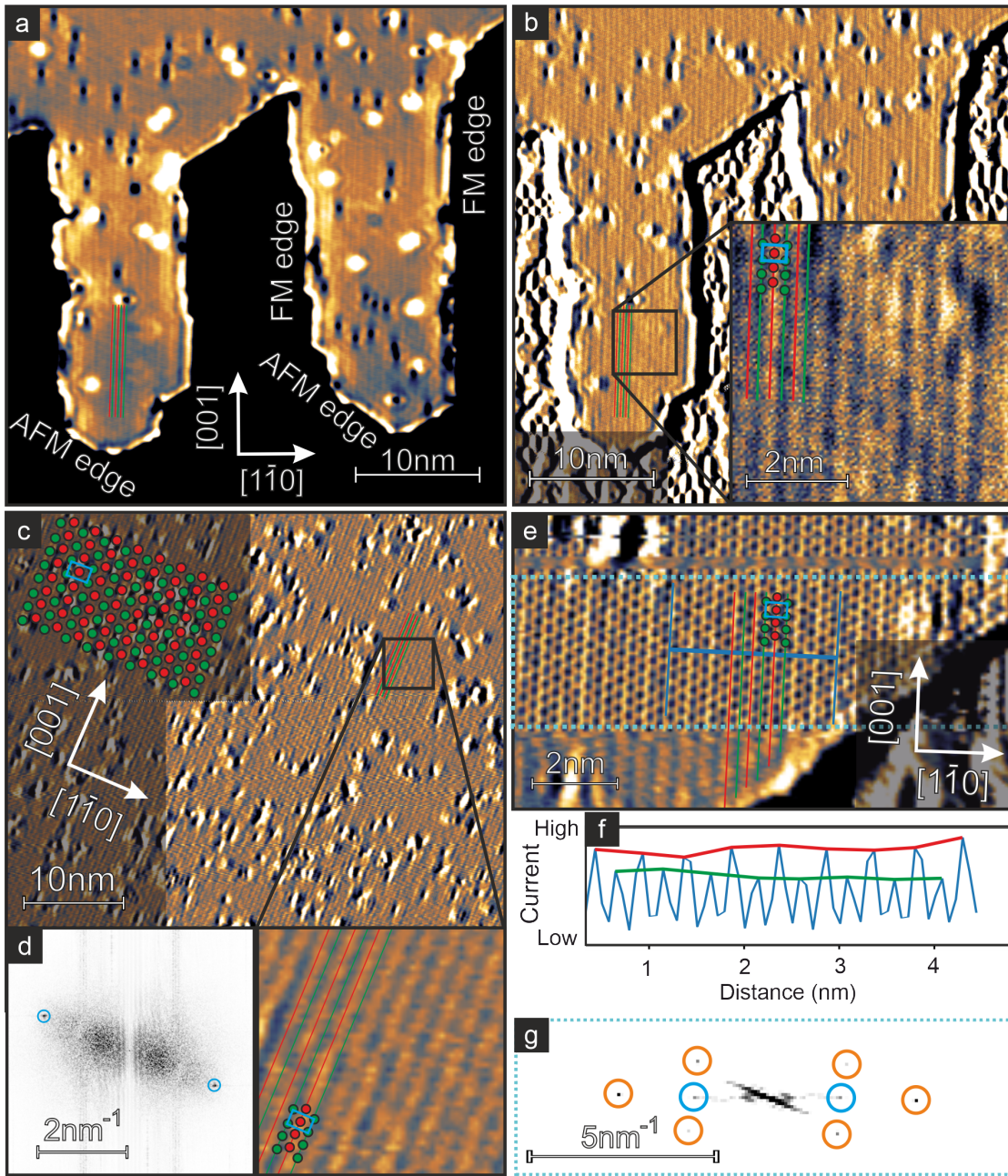


Figure 5.7: Cr first layer: magnetic ground state. (Caption next page.)

Figure 5.7 (previous page): Cr first layer magnetic ground state. (a) Constant-current SP-STM image of the first layer of Cr displaying the $c(2 \times 2)$ AFM ground state in the topography channel. (b) Current channel of panel (a). The inset reveals more clearly the magnetic resolution. Atoms with different spin orientation are sketched on top the image as red and green circles. The magnetic unit cell is represented with a cyan rectangle. (c) Current channel of a constant-current SP-STM image of an extended Cr first layer patch with magnetic resolution. The top left inset shows a sketch of the extended $c(2 \times 2)$ AFM ground state. The right bottom zoom-in exhibits more clearly the magnetic corrugation. (d) FFT of panel (c) with the magnetic peaks highlighted with cyan circles. (e) Current channel of a constant-current SP-STM close-up of Cr first layer with atomic and magnetic resolution. The bottom part of the image exhibits only magnetic resolution. The top part of the image exhibits both atomic and magnetic resolution simultaneously. (f) Profile obtained along the blue line in panel (e). The distance between peaks is the one for atomic resolution. Odd peaks are joined by a green line and even ones by a red one to highlight the alternating height levels of the peaks which reveal the magnetic contrast. (g) FFT of the cyan rectangle in panel (e) with the atomic peaks highlighted with orange circles and the magnetic peaks highlighted with cyan circles. (Measurement parameters: (a), (b) $U = +15$ mV, $I = 7$ nA, $T = 4$ K, (c) $U = +10$ mV, $I = 7.7$ nA, $T = 4$ K, (e) $U = +5$ mV, $I = 4$ nA, $T = 4$ K).

The magnetic superstructure is represented in most panels of Fig. 5.7 with red and green lines, sometimes also represented by red and green atoms. The magnetic unit cell is indicated in blue.

Further experiments are needed to determine the easy axis of the magnetic moments in the extended first layer of Cr. I propose to study the first Cr layer on Nb(110) by an Fe coated W tip with different applied magnetic fields to determine said easy axis.

Superconductivity

The Cr first layer exhibits a superconducting gap similar to the one of the Nb. The Cr gap is populated by in-gap states that arise from the presence of magnetic moments (Fig. 5.8 (b) blue curves for Cr vs black curves for Nb). These states are the 2D analogon of the YSR states, i.e. YSR bands. In Fig. 5.8 (b), several series of spectra of the Nb, Cr, and Cr edge states are shown. Different series are taken with different but comparable tips in different locations. The spectra in this panel were taken with a Cr bulk tip with Nb atoms at the apex, which leads to a doubling of the gap's size. This effect discussed in section 3.1, lets us obtain the Δ_{tip} value via eq. 3.1: $\Delta_{measured} = \Delta_{tip} + \Delta_{sample}$. In the case of a Nb sample, $\Delta_{sample} = 1.55$ mV [5]. With that information, Δ_{tip} is represented in Fig. 5.8 (b), having a value of ≈ 1.55 mV, by the gray rectangle around zero energy. The spectral weight inside Δ_{tip} is either created by thermal excitations or is a result of the thermal broadening of states outside Δ_{tip} , so it is not considered.

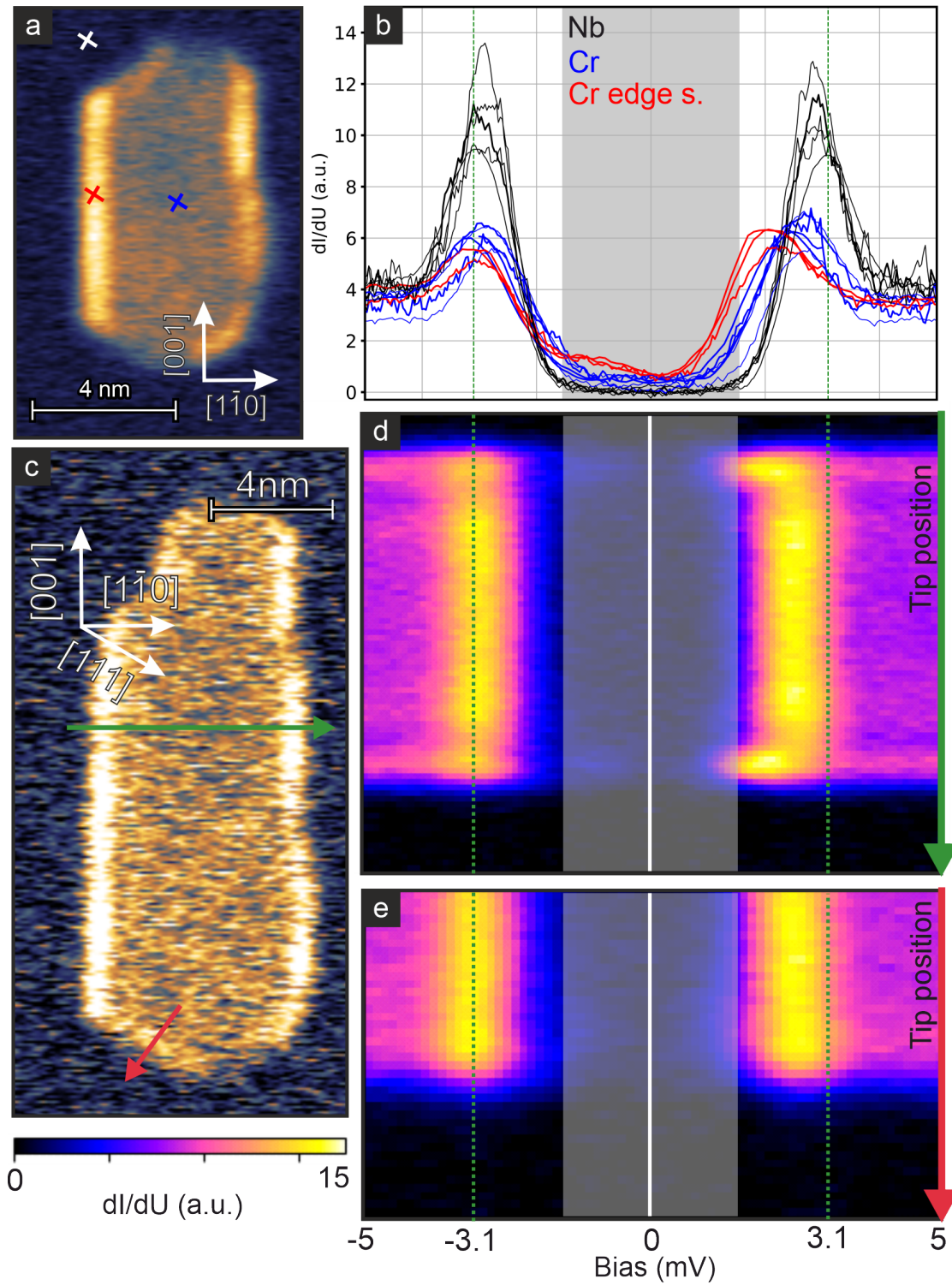


Figure 5.8: Cr first layer: zero energy edge state imaging and in-gap states. (Caption next page.)

Figure 5.8 (previous page): Cr first layer zero energy edge state imaging and in-gap states. (a) Constant-height STM close-up of a first layer Cr island measured at the sample's Fermi energy. This measurement reveals the existence of zero energy modes localized along the [001] step edges. The crosses are exemplary locations of the curves in (b). (b) Spectra taken over Nb, Cr extended layer and Cr edge state. The vertical dotted lines indicate the positioning of the Nb coherence peaks (± 3.1 mV) for an ideal Nb tip. The gray rectangle around $U = 0$ mV represents the tip gap (Δ_{tip}) for an ideal Nb tip. (c) Constant-height STM close-up of a first layer Cr island measured at the sample's Fermi energy. The measurement exhibits peaks in the dI/dU contrast at the edges that run along the [001] direction. (d) Waterfall plot representation of a series of constant height spectra taken along the green line in panel (c). (e) Waterfall plot representation of a series of constant height spectra taken along the red line in panel (c). (Stabilization parameters for waterfall plots and single spectra: $U = +5$ mV, $I = 1$ nA, $T = 4$ K. Measurement parameters: (a) and (c) $U = +1.5$ mV, $E \approx 0$ meV, $T = 4$ K. Modulation: all 50 μ V. Tip: all Cr bulk with Nb clusters in the tip).

Knowing Δ_{tip} allows us to sample the Cr at determined energies with respect to its Fermi energy: $\pm E = \pm |U_{applied}| \mp |\Delta_{tip}|$. For example, Fig. 5.8 (a) shows the dI/dU channel of a constant height measurement on a small Cr island, taken at 1.5 mV with the same tip as the spectra in panel (b). As $\Delta_{tip} \approx 1.55$ mV, then $E \approx 0$ meV. Therefore, the measurement is done at roughly zero energy for the sample. In the image it is possible to observe how the edges running along the [001] direction exhibit an increased conductance at zero voltage; these are edge modes or edge states. However, due to the limited energy resolution and approximate value for the tip gap, their exact energy cannot be determined.

In Fig. 5.8 (b), the red curves show the spectra corresponding to the edge states. The comparison of the three colors of curves in Fig. 5.8 (b) gives some information about the Cr in-gap states, but the lack of energy resolution prevents a complete characterization. The negative energy peaks barely move towards the inside of the gap. On the other hand, the positive peaks shift towards zero energy considerably. The modeling of a similar gap in Fig. 5.9 reveals that this can occur due to the lack of resolution and the different intensity of the in-gap states. The negative in-gap states can have a smaller intensity and not shift the observed position of the resultant peaks. The positive energy peaks of the in-gap states can have a bigger intensity, resulting in a shift of the resultant peaks. This effect could therefore explain the measurements. In Fig. 5.8 (b) it is observed how the Cr in-gap states away from the edges (Cr bulk) have a higher energy than the ones of the edge states. The positive energy peaks appear at roughly $E = 1.35$ meV for the Cr bulk states and $E = 0.7$ meV for the Cr edge state.

In Fig. 5.8 (c), the dI/dU channel of a constant height image at $E \approx 0$ meV of another Cr first layer island is shown. Across this island, constant height line profile spectroscopies

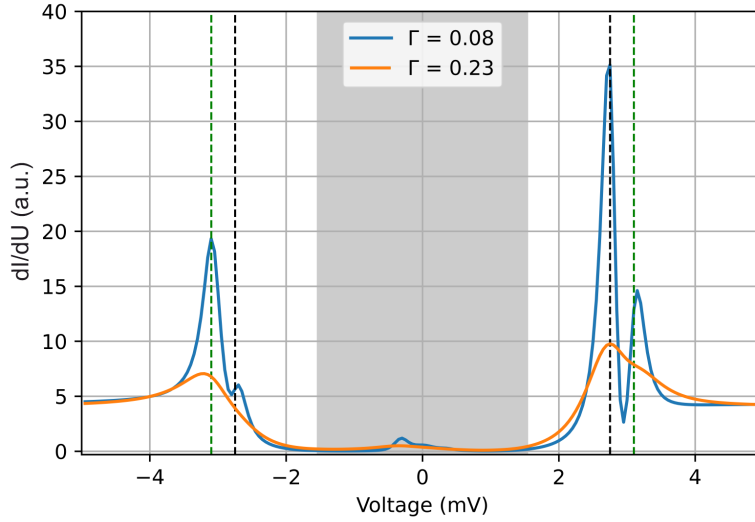


Figure 5.9: Modeling of a superconducting gap with two different broadening factors. In the modeled system, both tip and sample have a 1.55 meV gap. The sample exhibits in-gap states at ± 1.2 meV with very different intensities for exemplary purposes. When the broadening factor is small (better resolution) it is possible to observe both in-gap states in addition to the coherence peaks of the system. When the broadening factor is bigger (worse resolution), the coherence peaks and the in-gap states cannot be distinguished. This appears as a shift of either the in-gap state to the coherence peak (negative energy case) or vice versa (positive energy case).

were taken along the green and red arrows, i.e. perpendicular to a [001] edge (green) and a [111] edge (red). The obtained data are displayed in Fig. 5.8 panels (d) and (e) as waterfall plots. The spectra were taken at constant height. This measurement mode optimizes the resolution for the Cr island and avoids artifacts generated by the tip feedback. Due to that the Nb sections of the waterfall plots do not exhibit any features, as they are further away from the tip. This helps identifying the edge of the island in the waterfall plots. In Fig. 5.8 (d) two edge states can be seen, one per side of the island. In both cases it is possible to see how the Cr in-gap states shift from a position closer to the Nb peaks (dotted lines) inside the island towards zero energy at the edges. In panel (e) just one edge is shown. In this case the Cr in-gap states do not exhibit major changes when approaching the edge. Comparing these waterfall plots reveals the low energy edge state dependency on the crystallographic direction of the edge.

As a summary, low energy edge states are observed along the ferromagnetic edges of the Cr/Nb(110) system, as the theory by Bazarnik *et al.* predicts [5]. No STS measurements were done for the zigzag edges as they are much less common than the FM and AFM edges. Bulk in-gap states compatible with the ones reported in said publication are also observed (Fig. 5.8 (b), (d) and (e)). These observations inside the theoretical

frame established by Bazarnik *et al.* let us conclude that the first monolayer of Cr on Nb(110) is another example of a topological nodal point superconductor.

5.3.2 Cr worms

Observations

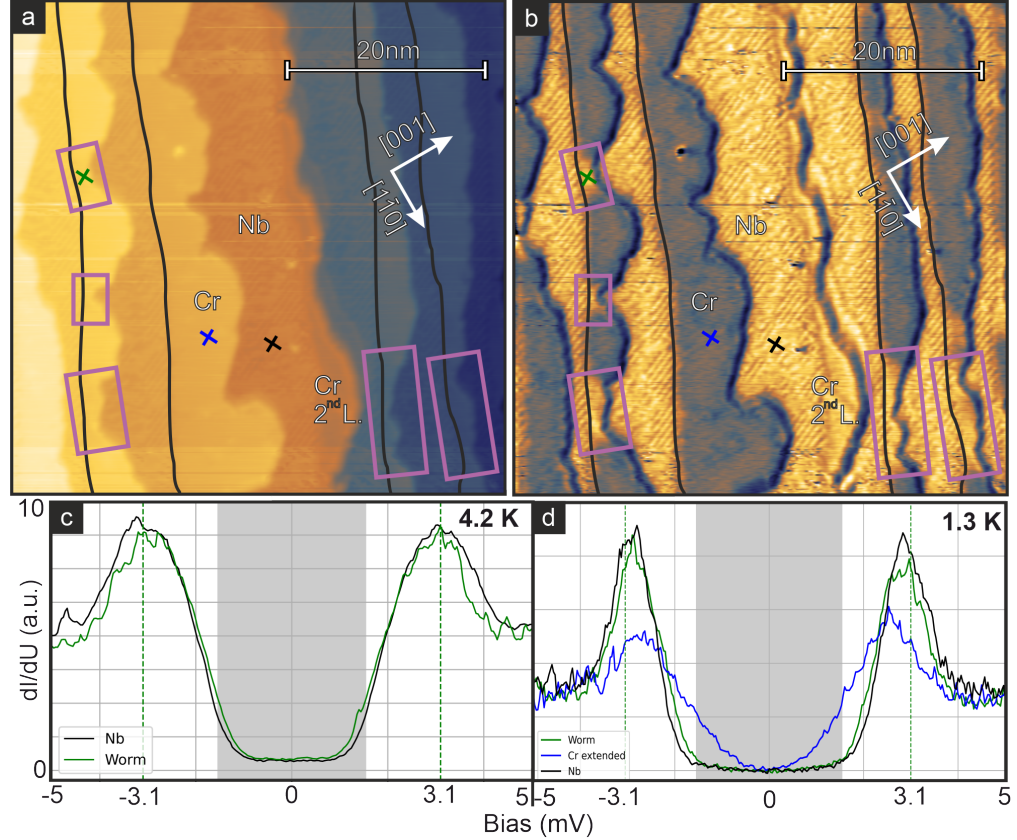


Figure 5.10: Worm characterization. (a) Constant-current STM image of a region displaying several buried Nb step edges. The crosses indicate exemplary positions of the curves in panels (c) and (d). (b) dI/dU channel of panel (a). There is a contrast difference between the Cr extended layer (blue) and Nb (yellow). Cr worms are highlighted by purple rectangles. In topography they look similar to the Cr extended layer, while in dI/dU they exhibit the same contrast as the Nb. (c) Nb-Cr worm spectroscopy comparison at 4.2 K. Both curves align almost completely inside the Nb gap. (d) Nb-extended Cr-Cr worm spectroscopy comparison at 1.3 K. The Nb and the worm curves align almost completely inside the gap again. The measurements are done with a tip different but comparable to the one in panel (c). (Stabilization parameters: (c), (d) $U = +5$ mV, $I = 1$ nA, (c) $T = 4.2$ K, (d) $T = 1.3$ K) (Measurement parameters: (a), (b) $U = +2$ mV, $I = 6.4$ nA, $T = 4.2$ K, modulation: (c), (d) $50 \mu\text{V}$, tip: (all) Cr bulk with Nb clusters at the apex).

The first Cr monolayer exhibits different properties than the ones discussed in section 5.3.1 when grown in very narrow strips. These Cr strips, called worms, exhibit the same superconducting properties as the Nb with different tips and variable temperatures (see Fig. 5.10 (c) and (d)). In particular, the Cr thin strips do not exhibit in-gap states, whereas the broader Cr regions do. As these in-gap states are indicative of magnetic moments, this suggests that thin Cr strips do not have magnetic moments. Additionally, no magnetic contrast has been obtained when performing SP-STM measurements. A convenient way to identify these worms is via dI/dU images inside the superconducting gap, such as at 2 mV when taken with a superconducting tip. In Fig. 5.10 (a) a region with a high density of terraces is shown. Due to the morphology of the region, thin strips of Cr grow in a step-flow growth fashion. In the image, some of the Nb buried step edges are drawn with black lines for clarity. The dI/dU channel of the same image is shown in panel (b), where the worms can be identified (regions highlighted in purple). These structures exhibit a maximum width (perpendicular to the step edge) but are not limited in length (along the step edge). It is unclear why these worms behave in a different way compared to the extended Cr. One possibility could be that they are magnetic domain walls between phase shifted AFM regions that nucleate in constrictions to reduce their energy. However, the worms occur in *all* constrictions where the width of the Cr layer is thin enough. It is very unlikely that the number of domain walls is exactly equal to the number of constrictions, so this possibility is ruled out.

When measuring worms in different areas and preparations, no worms were observed at step edges running along the [001] direction. On the other hand, when the step edges run along the $[1\bar{1}0]$, a maximum worm width of approximately 2 nm is found. In other words, if the angle between the step edge and the [001] direction is called θ , it is possible to observe a maximum worm width for $\theta = 90^\circ$, and no worms for $\theta = 0^\circ$. This means that when the angle between the step edge and the [001] direction is $\theta = 0^\circ$, the Cr layer displays in-gap states. In the following the maximum measured worm width is evaluated as a function of worm angle θ with respect to the [001] direction. Due to the structural symmetry of the system, with two orthogonal mirror planes, only $0^\circ < \theta < 90^\circ$ is considered. When measuring the maximum width of the worms for the different observed angles one obtains the graphs in Fig. 5.11 (a) and (b). This data is plotted as a 360° polar plot in panel (c) to highlight the symmetries of the system. It can be seen that there is a continuous decrease of the maximum worm width when the angle changes from the $[1\bar{1}0]$ direction to the [001] direction.

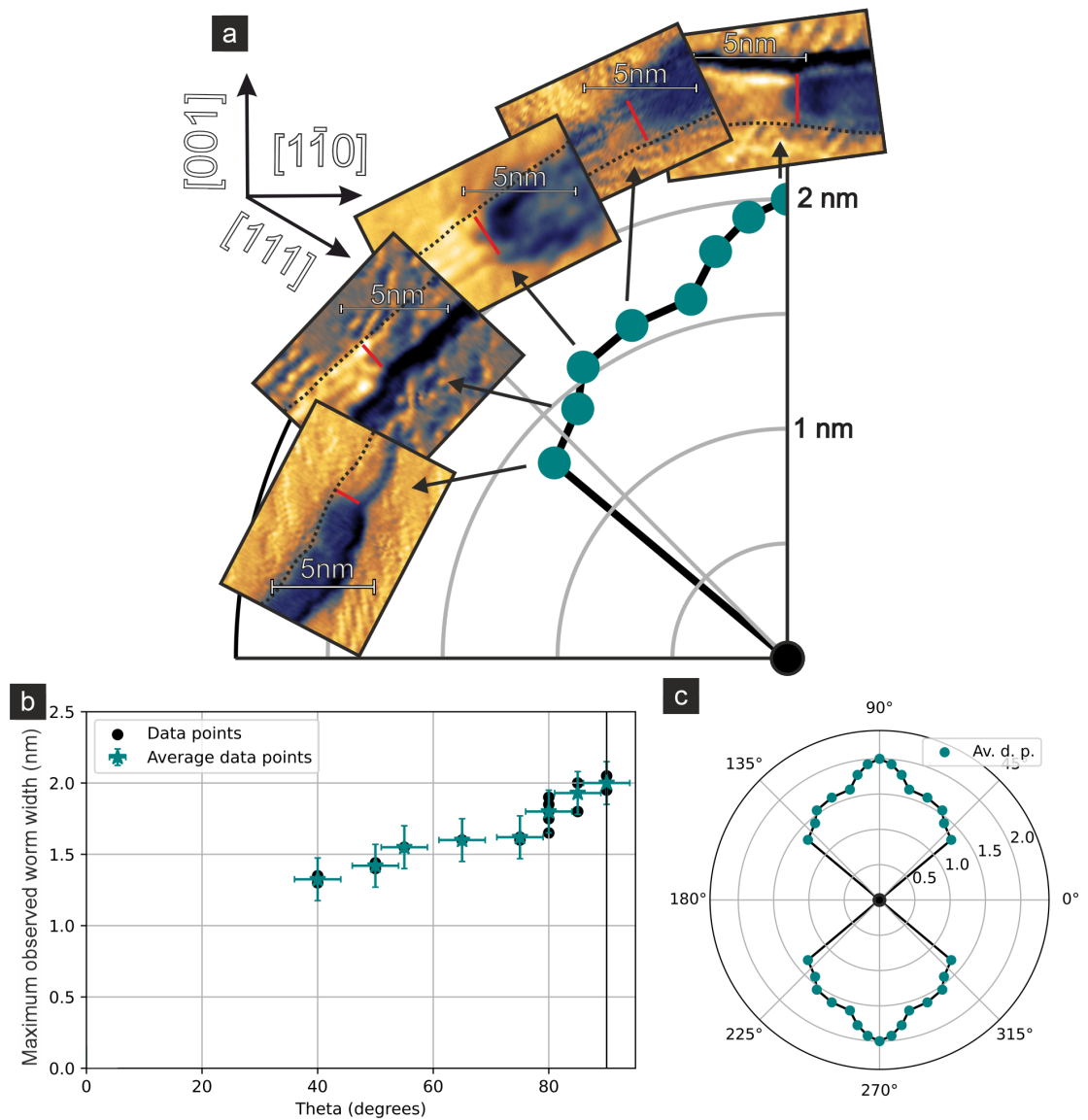


Figure 5.11: Maximum worm width angle dependency. (a) Representation of the average maximum worm widths for different angles in a quadrant of a polar plot. Some examples of the measured widths are shown along the graph with the same crystallographic orientation. (b) Maximum worm width vs. θ . Black points represent the widest measured worms for that angle, while teal points represent the average worm width for that angle. The error bars are 4° in the x-axis and 150 pm for the y-axis. (c) Generalization of panel (a) to the four equivalent quadrants.

Heisenberg exchange model

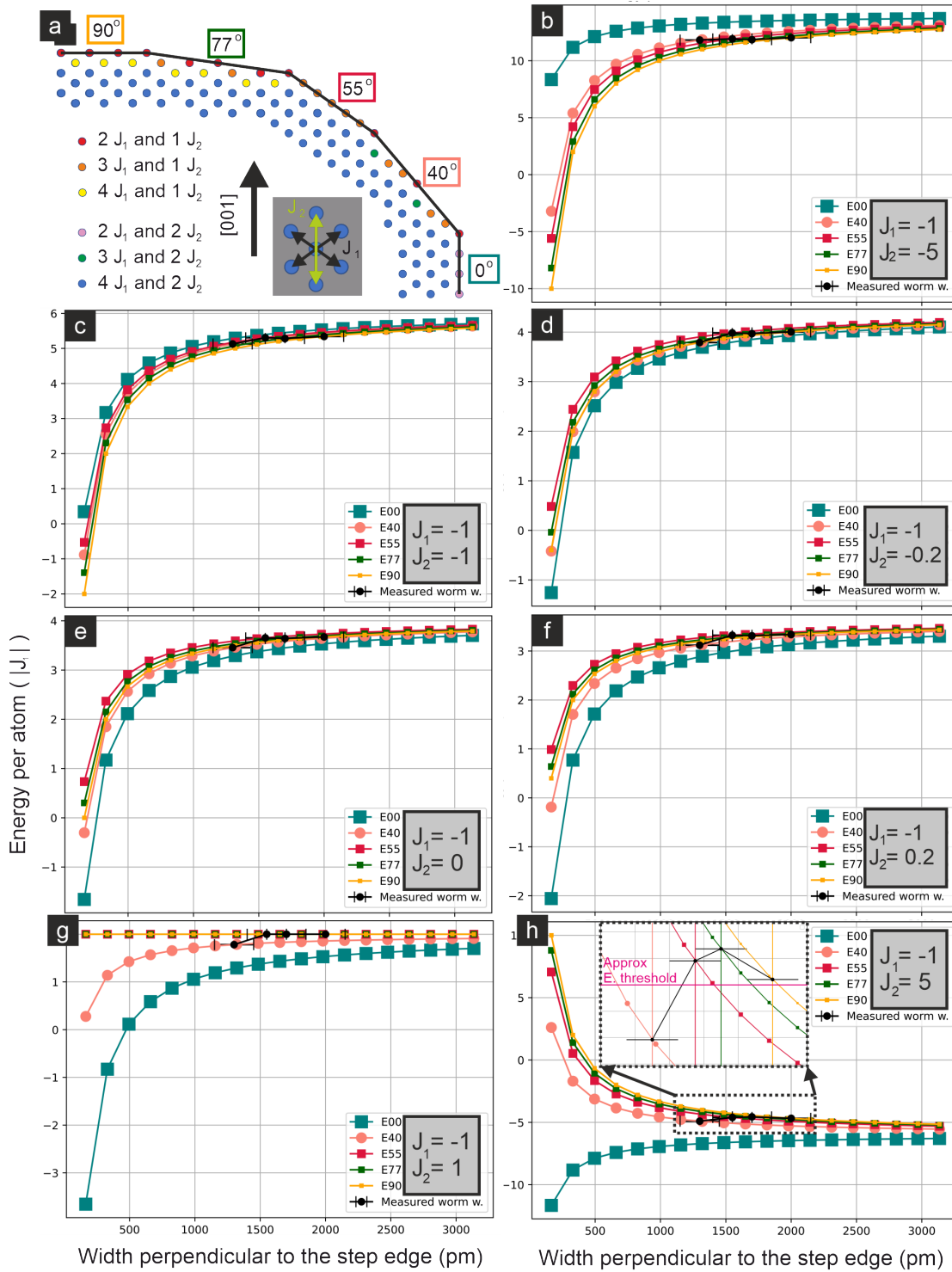


Figure 5.12: Heisenberg exchange model: edge anisotropy schematic and Heisenberg energy as function of Cr width for different J_2 values. (Caption next page.)

Figure 5.12 (previous page): Heisenberg exchange model: edge anisotropy schematic and Heisenberg energy as function of Cr width for different J_2 values. (a) Schematic showing different edges in a bcc(110) surface indicated by the black lines along the atoms. Different colored atoms indicate atoms with different combination of first and second nearest neighbors, and therefore different energy contributions indicated below. (b-h) Energy per atom as a function of width of the Cr layer. For these panels, $J_1 = -1$ (normalizing the energy with respect to J_1) and $J_2 = -5, -1, -0.2, 0, 0.2, 1$ and 5 respectively. The colors of the curves are the ones of the rectangles around the angles in panel (a). The black points mark the experimentally measured maximum worm widths for the different modeled angles.

The question arises why the maximum worm length depends on the angle. One possible explanation is the contribution of the edge to the energy of the magnetic systems. The symmetry of the bcc(110) surface results in different types of edges along different directions. For example, in the publication by Bazarnik *et al.* [5] they discuss the FM edge (along the [001] direction), the AFM edge (along the [111] direction) and the zigzag edge (along the $[1\bar{1}0]$ direction). This implies that different edges can be energetically different from a magnetic point of view. This type of study was already done by Spethmann *et al.* [87] for a RW-AFM on a hexagonal atomic lattice. Different edges can be named by the angle they form with the [001] direction. This way the FM edge is called the 0° edge, the AFM edge is the 55° edge and the zigzag edge is the 90° edge. It is possible to generalize this nomenclature for other measured intermediate edges such as the 40° edge or the 77° edge. All these edges are represented schematically in Fig. 5.12 (a). These edges differ in the number and type of neighbors that each of their atoms have. In the following only nearest and next-nearest neighbors (J_1 and J_2) are considered. In Fig. 5.12 (a) different colors for the atoms represent different neighbor configurations as explained in the label. For example, red colored atoms have two first nearest neighbors and one second nearest neighbor, while blue atoms have four first nearest neighbors and two second nearest neighbors, i.e. blue atoms are bulk-like. These edge differences define the Heisenberg exchange energy that these atoms contribute to the total energy in a certain Cr layer. Then it is possible to calculate the energy of a Cr strip growing along these edges as a function of width. For that equation 2.10 ($\mathcal{H}_{exchange} = -\sum_{ij} J_{ij} S_i \cdot S_j$) is used. But to use this equation the values of J_1 and J_2 are needed.

As it is known that the extended Cr layer exhibits a $c(2 \times 2)$ AFM structure, J_1 must be negative. Then the model can be normalized to J_1 , i.e. $J_1 = -1$. With that information seven qualitatively different J_2 possibilities can be found. These are represented in Fig. 5.12 (b-h): $J_2 < J_1$, $J_2 = J_1$, $0 > J_2 > J_1$, $J_2 = 0$, $0 < J_2 < |J_1|$, $J_2 = |J_1|$ and $J_2 > |J_1|$. In Fig. 5.12 (b-h) the energy per atom of a Cr strip along different angles (color-coded) is plotted against the width of the strip. It is possible to see how all curves converge to the

same energy value for an infinitely wide Cr layer. This occurs because the differences in the curves come from the edge differences, which become negligible for extended Cr layers. For this model it is assumed that a certain minimum energy per atom due to magnetic exchange is necessary to form a collective AFM state in the Cr layer. If the energy is not enough, no magnetism evolves. In this case the moments are quenched. If the energy exceeds this threshold, antiferromagnetically coupled magnetic moments appear, i.e. magnetism is nucleated. It is important to note that no other interactions are considered for this model.

Energy minimization simulations neglecting the spin dynamics of our lattice reveal that $J_2 > J_1/2$ to nucleate the observed AFM structure, which indicates that the system is not represented by panels (b) or (c). Additionally, it is observed that magnetism is not nucleated for small worm widths except for 0° edges, so the Heisenberg exchange energy per atom must be higher than the bulk value. In the model, just $J_2 > |J_1|$ reproduces this observation. This is consistent with the simulations, as a negative J_1 and a positive J_2 both stabilize the observed $c(2 \times 2)$ magnetic state. Fig. 5.12 (h) shows an example of the modeled energies per atom in units of $|J_1|$ as a function of the strip width for different edges and a chosen $J_2 = 5$. In the graph it is possible to see for the modeled edges 40° , 55° , 77° and 90° , that the wider the Cr layer is, the lower is the Heisenberg exchange energy per atom, i.e. when the layer grows it favors the nucleation of magnetism. This is not the case for the 0° edge whose energy increases with width. However, the 0° energy is always lower than any of the other cases, so it always nucleates magnetism. This is compatible with the experiments, in which the 0° Cr strips never exhibit worms, i.e. they are always magnetic.

In Fig. 5.12 (b-h), on top of the modeled energies for different edge strips, the observed maximum worm widths are placed as black points. If the system requires a certain energy per atom to nucleate magnetism, these black points should align roughly in a horizontal line (inside the error of the measurements). This would mean that once the energy curves are below this energy threshold, they should nucleate magnetism. If the values of J_2 are sampled to flatten the black curve, the bigger the J_2 values the better the flattening of the curve. This result could be different with more precise measurements, and just a high enough J_2 could explain the observations. With a reasonable J_2 inside these possibilities, such as the already discussed $J_2 = 5$, it is possible to obtain a threshold energy for which the magnetism nucleates. In this case the threshold energy is roughly $-4.7 J_1$. If this energy is used as an input for the model to obtain the maximum worm width as a function of θ , the model roughly reproduces the experimental data. This is shown in Fig. 5.13.

In Fig. 5.13 (a) one can see that the model reproduces the observations. For the 0°

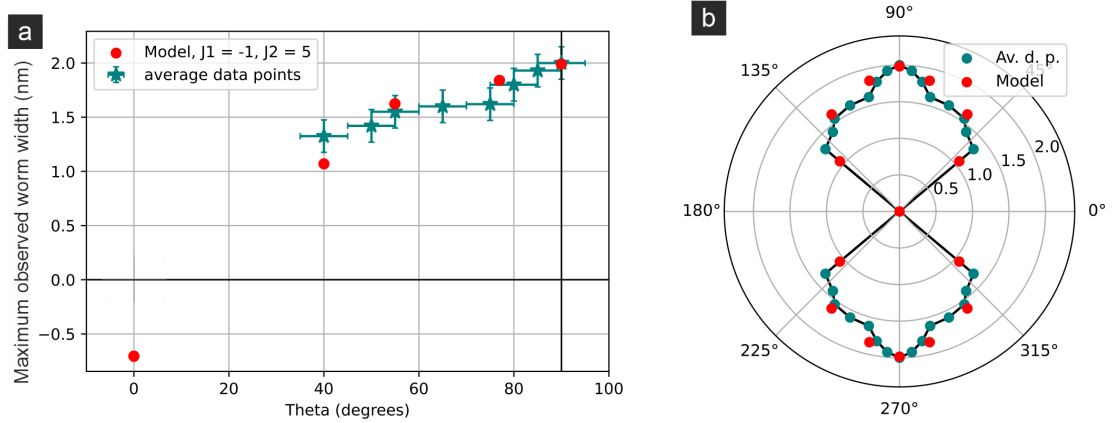


Figure 5.13: Heisenberg model comparison with experimental data. (a) The blue points represent the maximum measured worm widths, while the red ones represent the modeled points via the Heisenberg model. (b) Representation of the points in panel (a) in a polar plot, repeating the data for the four equivalent quadrants.

edge the model predicts a negative length, which has no physical meaning. The way to understand this is that the 0° edge is always magnetic, and it would require a certain amount of energy to make it non-magnetic. The amount of energy is equal to the Heisenberg exchange energy of a 0° edge of that length. One can then limit the lowest value for the width to 0. Then, if the data is represented in the polar plot, as in Fig. 5.11 (c), Fig. 5.13 (b) is obtained.

This simplistic model using only J_1 and J_2 can capture the angle dependence of the worm critical width. However, also other magnetic interactions can differ from bulk atoms to edge atoms, such as the MAE which is not included here. Including more interactions in the model might lead to a better fit to the experimental data, but without knowledge of the interaction parameters they will not lead to a better understanding of the system.

Cr magnetic moment quenching

DFT calculations from Tim Drevelow in Kiel [88] suggest that the Cr/Nb(110) system may be prone to quenching its magnetic moments, i.e. to reduce the magnitude of the spins to almost zero or zero [89]. The calculations predict that this moment quenching can originate from local spin non-collinearity. It is also possible that other small perturbations in the system have similar effects. Some further potential small perturbations include thermal excitations or interactions with Cooper pairs. These phenomena could be responsible for the threshold energy that must be overcome to nucleate magnetism,

leading to the appearance of the worms.

Regarding thermal excitations, the worms were studied at two different temperatures, 4.2 K and 1.3 K. During these experiments, a wedge shaped worm was found (see Fig. 5.14). If thermal excitations would play a role in quenching the moments, lower temperature should result in smaller maximum worm width (less moments quenched). This would result in this particular worm shrinking along the step edge. The comparison between Fig. 5.14 (a) and (b) reveal that the worm does not change despite the different temperature. This indicates that thermal excitations are not the dominant mechanism that leads to a quenching of the magnetic moments of the Cr worms, or at least it plays a minor role for the moment quenching.

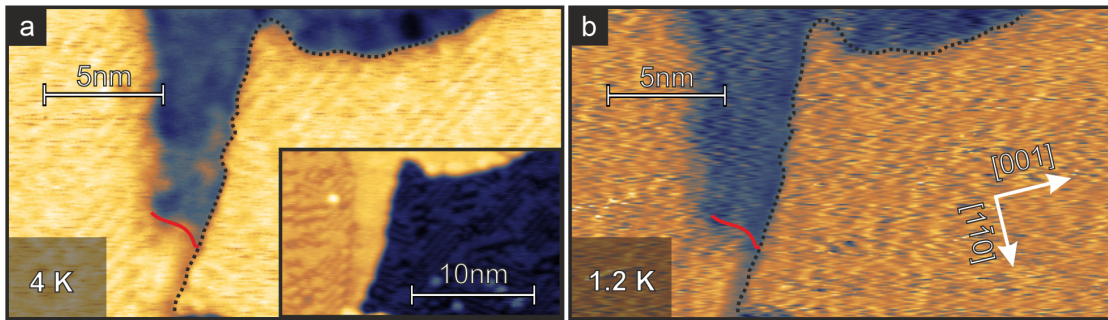


Figure 5.14: Worm size comparison at different temperatures. The dotted lines are placed as a reference in both images following the step between Cr and Nb. The red lines indicate roughly the border between the worm-like Cr and the extended Cr layer. **(a)** dI/dU channel of a constant-current STM close-up of a worm measured at 4.2 K. The inset is the topography channel of the image. **(b)** dI/dU channel of a constant-current STM close-up of a worm measured at 1.3 K. (Measurement parameters: **(a)** $T = 4$ K, **(b)** $T = 1.3$ K, **(all)** $U = +2$ mV, $I = 1.1$ nA).

Local spin non-collinearity has been calculated by Tim Drevelow in Kiel [88] to result in the quenching of the spins. As the moments prefer a collinear spin orientation in the extended Cr layer, any perturbation towards non-collinearity should come from its edges. This is a possibility due to edge magnetic anisotropy which could favor different moment orientations in the edges. If the edge magnetic anisotropy or any other edge effect (such as DMI) quench the moments of the edges, some edges should exhibit no magnetic contrast even in the extended layers. With the current data, this is not observed for any edge (see Fig. 5.7 (a) and (c) around the edges). Even, if the local moment quenching is localized to the last atomic row of the edges, it cannot be the only perturbation generating the worms, which consist in up to seven rows of atoms (depending on the direction). On the other hand, this effect could be responsible for part of the energy needed to nucleate magnetism. The quenching of the edge moments could explain by itself the existence of worms of two rows of atoms. Therefore it is concluded that the

non-collinearity possibly localized in some Cr edges cannot fully explain the existence of the observed worms. Further studies are required to discern if this perturbation is even present at the edge of the islands.

Another perturbation that could lead to the moment quenching in the worms is the interaction with Cooper pairs. This would be a case of superconductivity quenched magnetism. I have not realized experiments to prove this scenario, but I propose SP-STM measurements of the worms across the T_c of Nb. If the worms exhibit no magnetic contrast below T_c and they recover the magnetic moments above T_c , then superconductivity must be the perturbation leading to the moment quenching in the worms. This measurement could also be done applying a magnetic field to quench the superconductivity instead of using an increased temperature.

5.3.3 Cr second layer

The second Cr layer on Nb(110) is a structurally complex system with three reconstructed phases and two adatom phases on top, as discussed in section 5.2.2. Despite of this structural variety the second Cr layer always exhibits the same behavior regarding magnetism and superconductivity. That is why in this section I will mostly show data of the 1DR and the 2DR structural phases, as they are the most extended and well known.

Observations and discussion

Fig. 5.15 (b) shows the dI/dU channel of a STM image measured at 2 mV (which corresponds to $E \approx 0.5$ meV) where the second layer Cr patch with the 2DR displays the same signal intensity as the Nb surface. In Fig. 5.15 (d), a similar phenomenon occurs between the second layer 1DR and the Cr in the top right part of the image. This time the image is the dI/dU channel of a multipass image at 0 energy and the contrast is inverted. Additionally, the presence of in-gap states along the [001] edges is observed. These in-gap states are not observed along any other edge direction or when the edge goes to the first Cr layer. They are also visible in Fig. 5.15 (a) - (d) indicated by yellow rectangles. In panel (d) it is possible to see how they exhibit the same modulation as the 1DR present in the island. In Fig. 5.15 (e) a series of spectroscopy measurements taken with the same tip as panels (a) and (b) is displayed. It is clear that the Nb curve is identical to the ones obtained over the hollow site and the on-top site in the 2DR. In contrast, the second layer in-gap states located at the edge look more similar to the in-gap states observed in the first Cr layer. The absence of in-gap states (and therefore

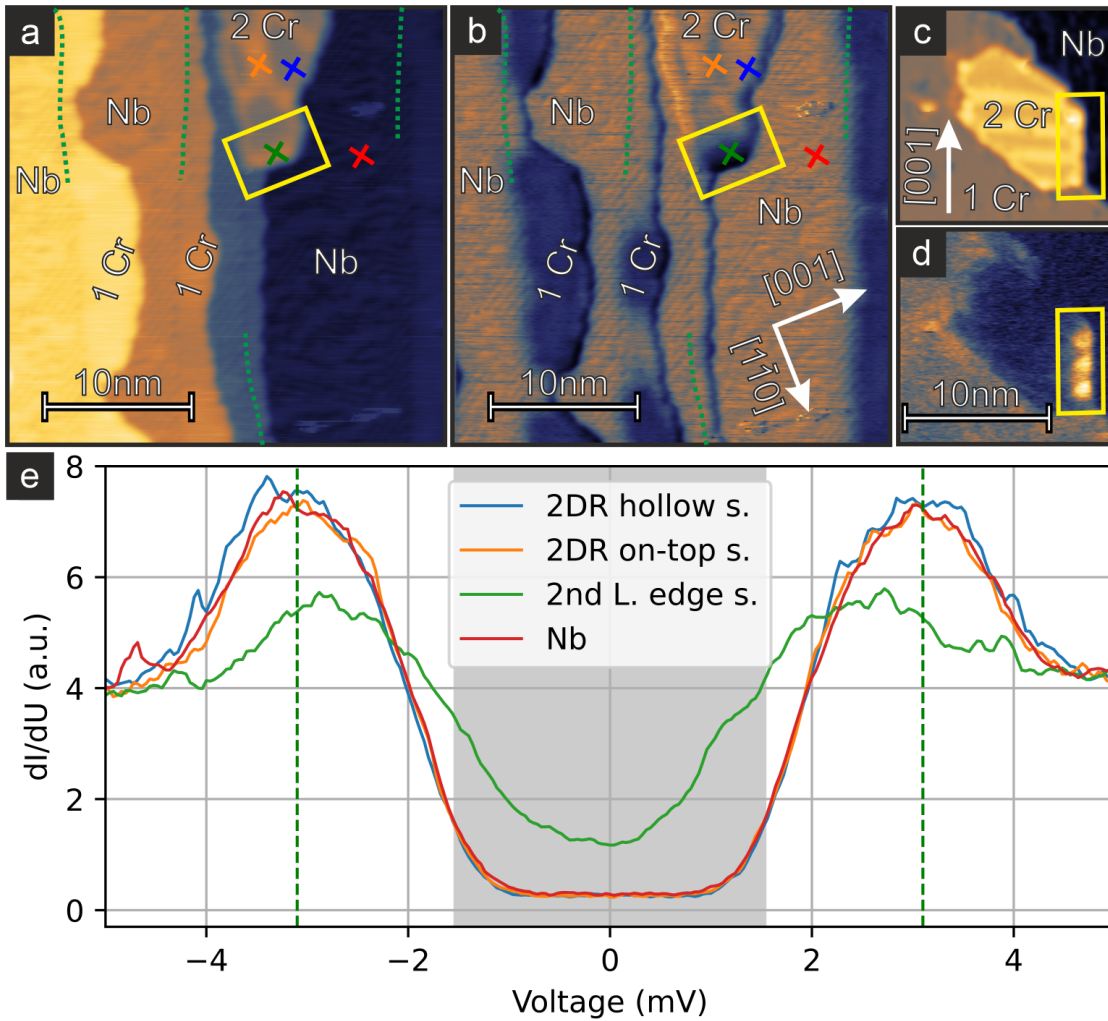


Figure 5.15: Second layer in-gap states imaging and spectra. (a) Constant-current STM image displaying the Nb surface, extended first Cr layer, first layer Cr worms and the second Cr layer with the 2DR. (b) dI/dU channel of panel (a). (c) Constant-current STM close-up of a second layer Cr exhibiting the 1DR. (d) Multipass of panel (c) at 1.5 mV (≈ 0 real mV). (e) Series of spectra taken around the location in panel (a) with the same tip. Example locations are placed in (a) and (b). (Measurement parameters: (a) and (b) $U = +2$ mV, $I = 3.1$ nA, $T = 4$ K, (c) $U = +5$ mV, $I = 1$ nA, $T = 4$ K, (d) $U = +1.5$ mV, $T = 4$ K. Stabilization parameters: (e) $U = +5$ mV, $I = 1$ nA, $T = 4$ K).

magnetism) in the second layer indicates the absence of in-gap states (and therefore magnetism) in the first layer below. No magnetic resolution has been obtained in any of the reconstructions of the second layer, including situations when first and second layers have been measured next to each other and the first layer has shown SP-STM contrast. This supports the absence of magnetic moments indicated by the absence of in-gap states.

The general absence of in-gap states and magnetic contrast in the extended Cr second layer is reminiscent of the case of the first layer worms. In the case of the second layer it is proposed that the magnetic inter-layer frustration created by the reconstructions may lead to the magnetic moment quenching of both first and second layer and therefore the absence of in-gap states. A schematic representation of how the system could look like if the moments were present is shown in Fig. 5.16. In the schematic it is assumed that the bottom layer exhibits a perfect AFM state and that the top strained layer has the same AFM state. One can see how sections with effective FM and AFM configurations between the layers alternate going through frustrated magnetic sections in between. The magnetic unit cell of both layers together is indicated in blue.

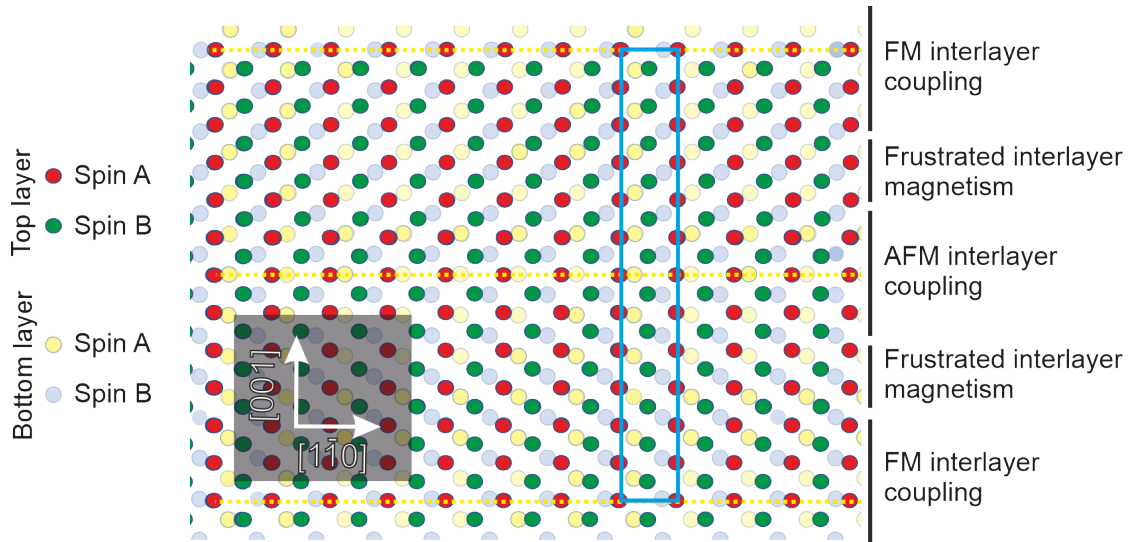


Figure 5.16: Schematics of the possible magnetic state in the reconstructed second layer. The half transparent blue and yellow circles represent the first layer Cr atoms with the $c(2 \times 2)$ AFM state. The green and red circles represent the second layer Cr atoms with the 1DR and the $c(2 \times 2)$ AFM state. The horizontal yellow lines represent the three-fold hollow sites of the atoms in the 1DR.

In conclusion, this schematic shows how the structural strain of the Cr second layer results in thin strips of both interlayer coupling possibilities. The favorable interlayer coupling regions (for example AFM) have a small width along the $[1\bar{1}0]$ direction,

which could result in the impossibility to generate a collective AFM state (similar to the worms).

Regarding the in-gap states localized at certain second layer edges, the possibility of them being edge states is excluded, as the second Cr layer does not show signs of magnetism. It is proposed that the second layer edge in-gap states are localized magnetic patches in the second layer edges or the first layer edges below. As discussed in section 5.2.2, the Cr second layer structure varies significantly from one point to another locally. This leads to the possibility of locally more pseudomorphic second layer areas where the AFM interlayer coupling regions shown in Fig. 5.16 could be capable of developing magnetism. In particular, this can be the case for the edges along the $[001]$ direction, where the second layer Cr atoms may be able to relax into three-fold hollow sites due to the absence of neighbors in one direction (see fig. 5.17 edges). Another possibility could be local patches with smaller strain, where the three-fold hollow site regions are extended, and, similar to the worms, can generate a collective magnetic state.

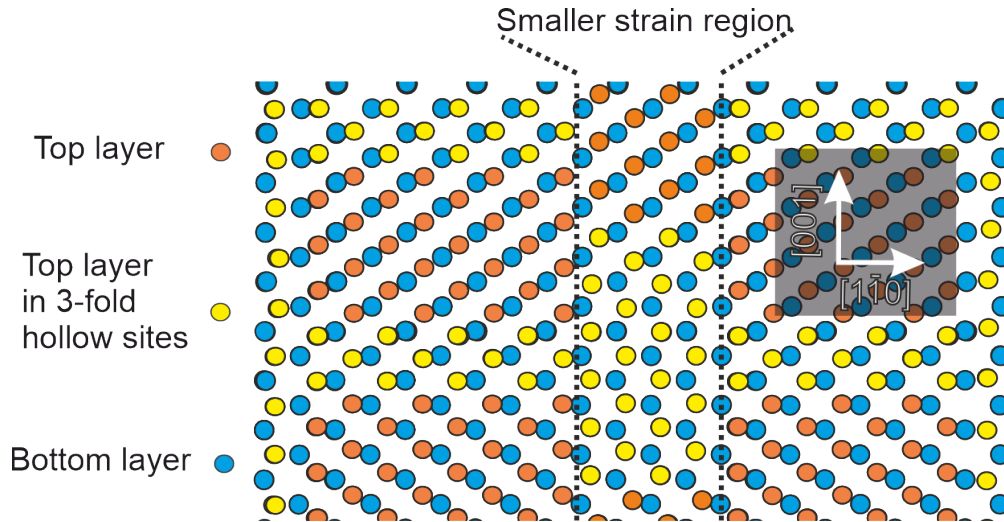


Figure 5.17: Schematics of possible magnetism nucleation points in the Cr second layer. Orange circles represent second layer Cr atoms outside three-fold hollow site positions. Yellow circles represent second layer atoms roughly positioned at three-fold hollow sites, i.e. pseudomorphic-like. Blue circles represent first layer Cr atoms positioned pseudomorphically on top of the Nb substrate.

This explanation is consistent with the observation of patches with in-gap states inside the 1DR of the second layer of Cr shown in Fig. 5.18 (a) and (b). Here one can see that in-gap state patches appear in slightly wider (less dense, i.e. more pseudomorphic) sections of the hollow site positions of the second layer (purple ellipses). No spectroscopy has been performed to characterize them, so their spectra cannot be directly related to

the ones obtained for the edge in-gap states. However, in Fig. 5.18 (c) - (e) the similarities of one of these patches (purple rectangles) and the edge in-gap states (yellow rectangles) are shown in the topography, dI/dU at 2 mV, and constant height map at ≈ 0 meV.

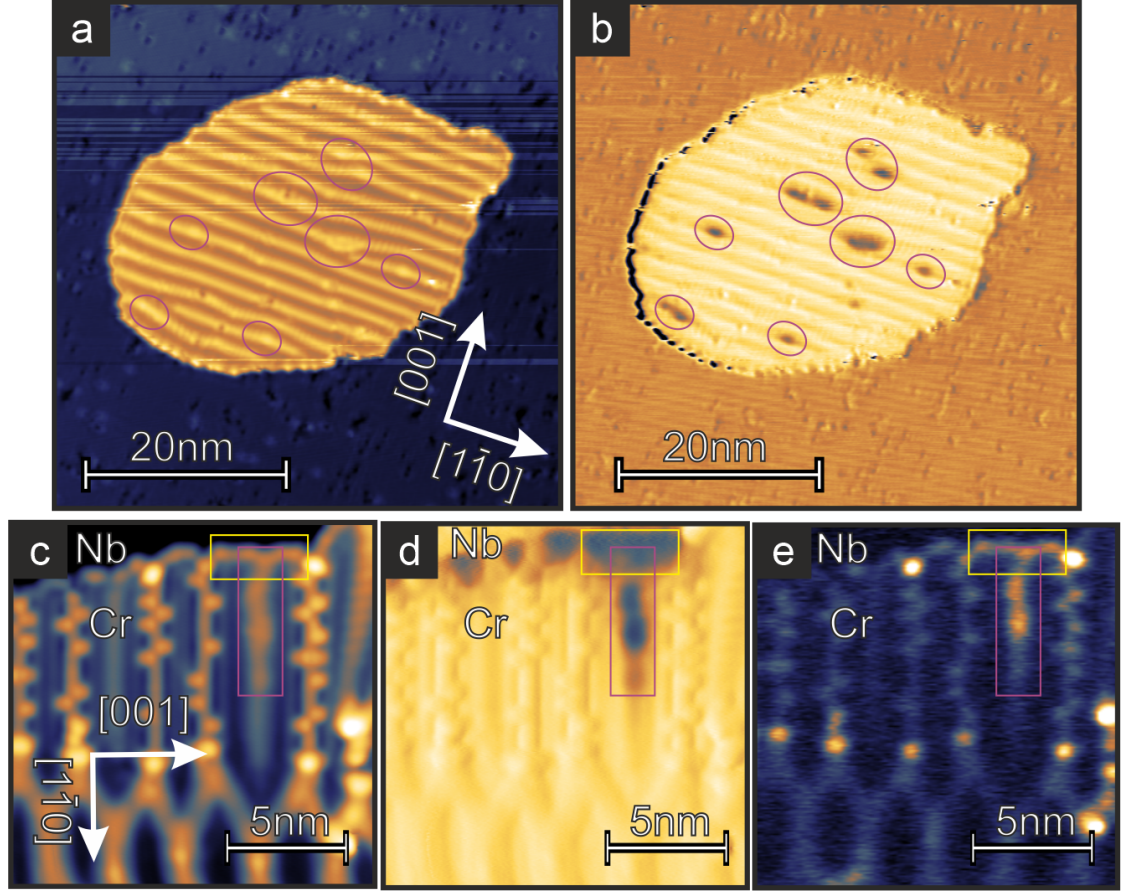


Figure 5.18: Patches with in-gap state and edge in-gap states. (a) Constant-current STM image displaying a second layer Cr island with the 1DR. (b) dI/dU channel of panel (a) where the patches can be observed. (c) Constant-current STM close-up of a second layer Cr island exhibiting the 2DR, the MBP, the ATTR and two 1DR lines. At the top of the right 1DR line, a patch can be found. (d) dI/dU channel of panel (c) where the patch and the edge in-gap states can be observed. (e) Constant height measurement of the region in (c) and (d) at ≈ 0 real mV (Measurement parameters: (a) and (b) $U = +2$ mV, $I = 7.6$ nA, $T = 4$ K, (c) and (d) $U = +2$ mV, $I = 3.5$ nA, $T = 4$ K, (e) $U = +0.5$ mV, $T = 4$ K).

I propose further measurements of these patches and the edge in-gap states both via STS and SP-STM imaging to determine the nature and possible relation between these objects.

5.4 Cr/Nb(110) conclusions and outlook

Cr/Nb(110) is a system where many different interactions compete to determine the local features of the layers. The structure evolution of the Cr layers is generally understood and can be used as a solid platform to understand other phenomena. The first Cr layer grows pseudomorphically, while the second one grows with a series of reconstructions depending on the Cr density. Finally, the third layer grows with the Cr bulk structure. The system exhibits the TNPSC phase in the first layer, but minor perturbations seem to disrupt it. One example for this are the worms, which do not display TNPSC characteristics. In the case of the second layer, perturbations such as inter-layer magnetic frustration could be responsible for the absence of TNPSC, and local perturbations (such as edge magnetic anisotropy) may be the ones helping to nucleate it. The structure variability of the second Cr layer appears as a promising candidate to study the TNPSC phase. This could be realized evaporating new materials on the sample that could force the second layer to change its structure. One example could be Mn, which is known to grow pseudomorphically on Nb(110) in both the first and second layers [90]. This could result in STM-accessible pseudomorphic second layer Cr islands. A non-magnetic material instead of Mn could also be useful to avoid its magnetic state to affect the one of the Cr. This Mn approach is schematically represented in See Fig. 5.19.

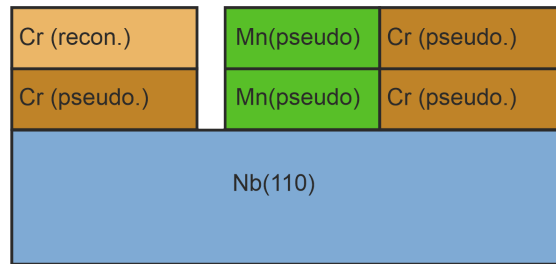


Figure 5.19: Schematic representation of how the second layer of Mn/Nb(110) could potentially help obtaining a pseudomorphic second layer of Cr on Nb(110).

Further studies are required to understand in detail some of the magnetic and superconducting properties of the system. Additionally, the already started collaboration with theory is necessary to fully understand the observed phenomena.

6 Appendix A: Further considerations about the growth of Cr/Nb(110)

"There is only one thing in the world worse than being talked about, and that is not being talked about."

— Oscar Wilde, *The Picture of Dorian Gray*

In this appendix, I will discuss the intermediate growth phases between the 1DR and the 2DR in the second layer of Cr on Nb(110). I will additionally summarize the whole growth of Cr/Nb(110) from the first layer to the third layer.

6.1 Cr second layer: intermediate growth phases

6.1.1 Train track adatom phase

The TTP appears when more Cr is evaporated on the 1DR (Fig. 6.1 (a)). This reconstruction consists of adatoms partly embedded in the second Cr layer, located at both sides of the 1DR elevated reconstruction lines. Line profiles over the adatoms along the $[1\bar{1}0]$ direction reveal the details of the reconstruction. Once one adatom is placed on one side of a 1DR line, another adatom can be placed on that side of the 1DR at a minimum distance of 934 pm, i.e. twice the periodicity along the $[1\bar{1}0]$ direction. This minimum distance is attributed to the local lattice distortion generated by the existing Cr adatom. This means that there are two possibilities between the sides of the TTP: The sides are either in phase (purple rectangles in Fig. 6.1 (a)) or out of phase (green rectangles in Fig. 6.1 (a)). In general, the in-phase arrangement is preferred. In rare occasions, some adatoms on the same side of the same line may place themselves at 467 pm from each other. This generates a higher corrugation, see Fig. 6.1 (b).

The Moiré structure of the 1DR results in the three-fold hollow sites of the second Cr layer not being equivalent. This leads to a preferred nucleation site for the TTP adatoms. We assume that the preferred stacking is the A-B-A stacking without loss of generality to portray the model.

The distance between adatoms on opposite sides of the same line along the $[001]$ direction is measured to be roughly 550 pm. This is determined between two out-of-phase

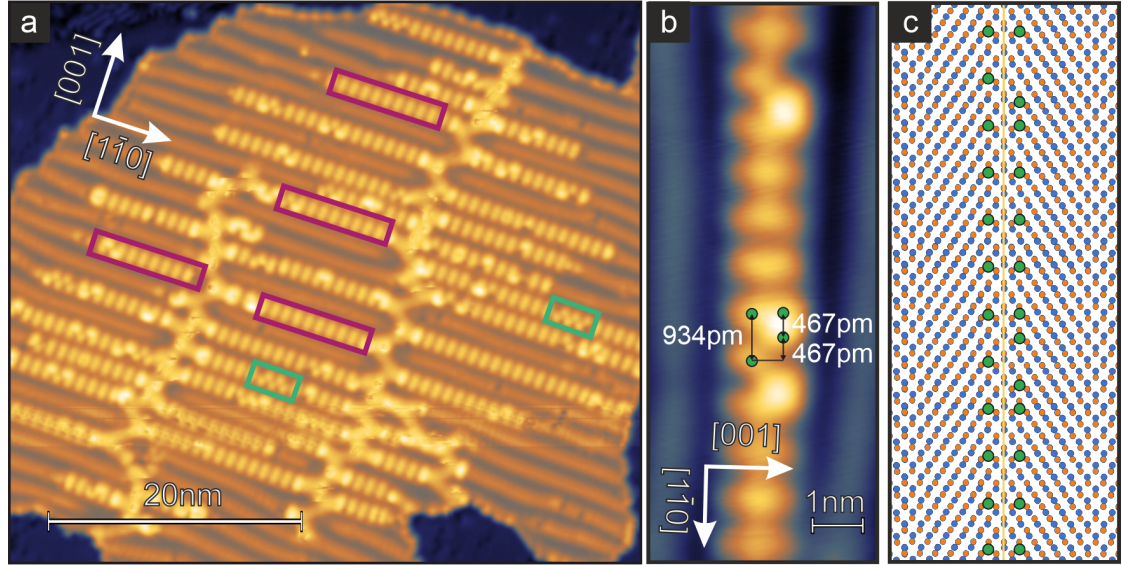


Figure 6.1: Train track adatom phase overview and model. (a) Constant-current STM image of a second layer Cr island exhibiting the TTP. The adatoms appear tightly packed over the 1DR. (b) Constant-current STM close-up of a TTP line. Some atoms and their relative distances are highlighted. (c) Atomistic model representing the structure in panel (b). The vertical yellow line represents the symmetry axis of the TTP line. The blue circles represent the first layer Cr atoms with the BCC (110) symmetry. The orange circles represent the second layer Cr atoms with the 7.5% compression along the $[001]$ direction. The two different three-fold hollow sites of the second Cr layer are not equivalent if we take into account the first Cr layer. This leads to a preferred one for the adatoms to nucleate. (Measurement parameters: (a) $U = +10$ mV, $I = 7.6$ nA, $T = 4$ K, (b) $U = +100$ mV, $I = 6$ nA, $T = 4$ K).

adatoms to increase the resolution of the measurement (like the ones in the green rectangle in Fig. 6.1 (a)). If we take into account that the second layer is compressed along the measurement direction, we would expect a distancing of around 600 pm. We propose that the local distortion of the second layer created by the TTP adatom can further reduce this distance towards the observed 550 pm. This distance is then compatible with the positioning of the adatoms at two atomic distances in a compressed layer with a small further distortion. With this knowledge and the HCP assumption, an atomistic model capable of reproducing any TTP line can be developed. An example of this is shown in Fig. 6.1 (c), where Fig. 6.1 (b) is schematically represented. The vertical yellow line represents the symmetry axis of the TTP line. These are the perfect three-fold hollow sites of the 1DR. The blue circles represent the first layer Cr atoms, and the orange circles represent the second layer Cr atoms with the compression along the [001] direction. The Moiré of the second Cr layer forms a template of available three-fold hollow sites for the adatoms to nucleate. The green circles represent the TTP adatoms observed in Fig. 6.1 (b).

We can calculate the maximum atom density of the TTP adatoms. For that we consider the minimum adatom distance of 934 pm and the full occupation of all 1DR lines. This results in a TTP density of 1.06 atoms/nm^2 .

6.1.2 Absorbed train track reconstruction

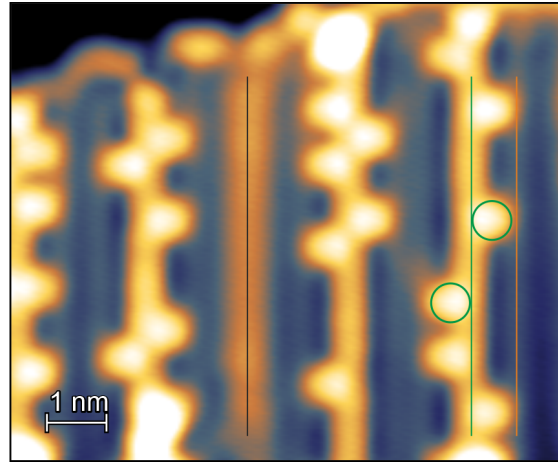


Figure 6.2: Absorbed train track reconstruction. Constant-current STM image of a second layer Cr island exhibiting the ATTR. One of the ATTR lines is marked in green, with two atoms of the MBP attached to it also marked in green. One of the secondary ATTR lines is marked in orange. The only 1DR line is marked in black. (Measurement parameters: $U = +2 \text{ mV}$, $I = 3.4 \text{ nA}$, $T = 4 \text{ K}$).

When no more TTP adatoms can be placed over the 1DR, the adatoms are absorbed by the second Cr layer. This gives rise to the ATTR (Fig. 6.2). The ATTR is a very localized reconstruction that can be understood as a local atom density increase around the 1DR lines, not modifying the general 1DR periodicity. Its confined nature does not allow its study as a Moiré structure. It appears similar to the 1DR but with thinner, brighter and more straight lines than the previous reconstruction. This difference can be seen in Fig. 6.2 between the line marked in green (ATTR line) and the line highlighted in black (1DR line). At very low bias voltage (2 mV), the ATTR also displays extra sets of less bright lines in between the main ones, highlighted in Fig. 6.2 by an orange line. These lines appear roughly at 800 pm from each other, but with certain variability depending on the boundary conditions. The ATTR is always observed with the next adatom phase (the MBP) on top, marked in Fig. 6.2 by the green circles. As the ATTR is surrounded by two adatom phases, it can be understood as just a milestone on the way from the 1DR to the 2DR in which the surface atom density of the second Cr layer is well defined. As it is created by the addition of the TTP to the 1DR, its atom density is the one of the 1DR plus the one of the TTP adatoms, i.e. $14.12 + 1.06 = 15.18 \text{ atoms/nm}^2$.

6.1.3 Music box adatom phase

The music box adatom phase (MBP) is the adatom phase formed over the ATTR. It consists of further Cr atoms evaporated over the ATTR, and possibly remanent ones from the TTP. In this case, the underlying reconstruction lines are not completely covered by the adatom phase. The analysis of the adatoms along the $[1\bar{1}0]$ direction reveals the same minimum distance as observed in the TTP, i.e. 934 pm. On the other hand, the distance between adatoms on different sides of the same reconstruction line along the (001) direction is decreased. In the previous adatom phase, this distance was about 550 pm, while in this reconstruction it is measured to be roughly 500 pm. This is compatible with the further compression along the (001) axis generated by the absorption of the TTP. This small difference does not change qualitatively the structure of this adatom phase with respect to the previous one, making it possible to apply the same type of model now.

Constant-current STM measurements with low voltages and high currents, such as the ones of Fig. 6.3 (b), are capable of moving the MBP adatoms, confirming their nature. This movement is limited to hopping along the ATTR lines or from side to side of them. The atom manipulation movement allows positions between adatoms that are not commonly observed naturally (distances smaller than 934 pm).

If the position of the adatoms is compared along two MBP lines, sometimes it is possible

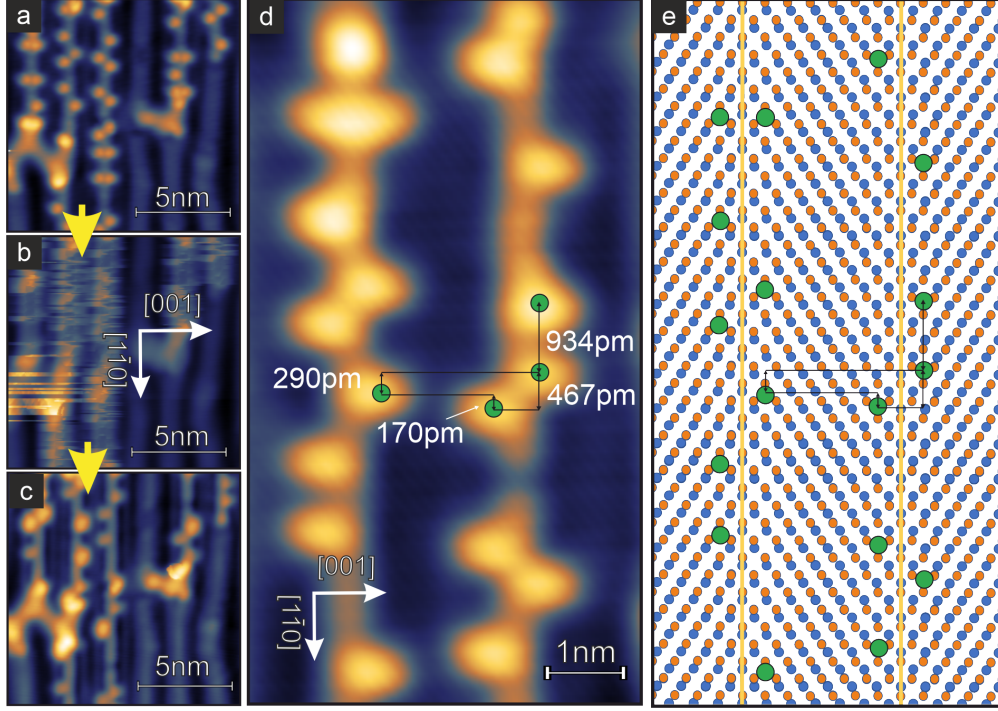


Figure 6.3: MBP adatom manipulation and model. (a) - (c) Series of constant-current STM images over a region with the MBR. The measurement in panel (b) at 40 nA is able to move the adatoms from side to side of the 1DR lines and along them. (d) Constant-current STM close-up of two MBP lines. The lines exhibit a phase shift between them and are not saturated of adatoms. (e) Atomistic model showing the structure in panel (d). The two different three-fold hollow sites of the second Cr layer are not equivalent if we take into account the first Cr layer. This leads to the 170-290 pm phase shift between MBP lines due to the template-behaving Moiré reconstruction. (Measurement parameters: (a) $U = +2$ mV, $I = 20.5$ nA, $T = 4$ K, (b) $U = +2$ mV, $I = 40.5$ nA, $T = 4$ K, (c) $U = +2$ mV, $I = 3.5$ nA, $T = 4$ K, (d) $U = +10$ mV, $I = 7.6$ nA, $T = 4$ K).

to observe a phase change of ≈ 170 pm or ≈ 290 pm (depending on the measurement direction). This 170-290 pm shift arises from the 1DR, and therefore the ATTR, sitting above the three-fold hollow sites of the first Cr layer. The two MBR lines shown in Fig. 6.3 (d) exhibit the 170-290 pm phase difference. This means that their adatoms are in equivalent, but shifted, three-fold hollow sites. Four of the adatoms are highlighted in panel (d), including the distances between them along the $[1\bar{1}0]$ direction. For those adatoms, most of the characteristic distances of the MBP can be observed: Two adatoms on the same side of the same MBR line cannot be closer than 934 pm. Two adatoms on different sides of the same line can be closer than that, in particular 467 pm or side by side (top left corner). When there is a shift between lines, adatoms from one line to another line can be shifted by roughly 170 pm or 290 pm depending on the measurement direction. In 6.3 (e) the whole MBP structure of panel (d) is modeled. The vertical yellow lines represent the symmetry axes of the MBP lines. These are the perfect three-fold hollow sites of the ATTR. The blue circles represent the first layer Cr atoms, and the orange circles represent the second layer Cr atoms with the compression along the $[001]$ direction. Once again, the Moiré of the second Cr layer forms a template of available three-fold hollow sites for the adatoms to nucleate. The green circles represent the MBR adatoms observed in Fig. 6.3 (d).

6.2 Cr growth: holistic structure model

Once the first layer, the five structural phases of the second layer and the third layer are independently understood, we can get a complete picture. Crystalline Cr forms a bcc structure with a lattice constant of 291 pm and a surface atom density of 16.7 atoms/nm² along the $[110]$ direction. When evaporated on another bcc structure such as Nb(110), it grows following the bcc(110) facet. The lattice constant difference, from 330 pm of the Nb to the preferred 291 pm of the Cr, generates strain that leads to different atomic structures in the layers. When directly in contact with the Nb surface, the Cr interlayer bonding energy cannot be overcome by the intralayer one, which leads to the atoms strictly following the structure of the Nb, i.e. they grow pseudomorphically. This forces a surface density of Cr atoms equal to the density of Nb atoms below: 12.98 atoms/nm².

The interlayer bonding energy between the first and second Cr layers is smaller than the Nb-Cr one, leading to extended first layer terraces. Once the second layer is nucleated, the smaller bonding energy makes the growth of the second layer possible with a non pseudomorphic structure, the 1DR. This reconstruction makes the second layer

energetically more favorable than the first one, as it resembles better the Cr(110) bulk interatomic distances. This results in a small amount of large-sized second layer islands. It also explains why the second layer growth often reaches the first layer edges, as the second layer growth is faster once nucleated. At this stage, the surface density of the second Cr layer increases to 14.12 atoms/nm^2 , approaching the Cr (110) one.

When Cr atoms are evaporated on the 1DR, they find new nucleation sites on the three-fold hollow sites of the reconstruction. These new arrays of adatoms are the TTP. They locally distort the 1DR, as revealed by their minimum observed distance. When a sufficient number of them populate the reconstruction lines of the 1DR, the distortions are high enough to restructure the second Cr layer and the adatoms are absorbed by it. This new phase is the ATTR, where the second layer density increases to 15.18 atoms/nm^2 . The ATTR reconstruction is more favorable than the 1DR, as it is closer to the Cr (110) density, but it requires the distortion of the previous adatom phase to appear. The local nature of this reconstruction, and the fact that it is just an intermediate stage in the density path from the 1DR to the 2DR makes the ATTR reconstruction less well understood structurally than any of the other phases.

Further evaporated Cr atoms generate a new, less dense adatom phase on top of the second Cr layer, the MBP. This phase is modeled almost in the same way as the TTP. The adatoms still find nucleation points in the second Cr layer, probably in locally less dense spots. Once again, these adatoms are absorbed by the second layer. In this case they distort the layer along the $[1\bar{1}0]$ direction, creating the 2DR. The analysis of this reconstruction reveals its unit cell to be 294 pm along the $[001]$ direction and 434 pm along the $[1\bar{1}0]$ direction. This is much closer to the Cr unit cell of 291 pm along the $[001]$ direction and 411 pm along the $[1\bar{1}0]$ direction than any of the previous reconstructions. This can also be conclude from the surface atom density, with a value of 15.63 atoms/nm^2 . However, the second layer Cr surface density is still smaller than the Cr(110) bulk surface density of 16.7 atoms/nm^2 .

To bridge this final density gap between the Nb(110) density and the Cr(110) density, it is necessary to take into account the third layer. Our current model indicates that when a third layer of Cr is nucleated on the Nb, the second layer changes its structure to the Cr(110) bulk one. The relaxation of the second layer strain appears as an isotropic compression of roughly 12%, leading to a moiré pattern that can be seen through the third layer. The third layer grows following the layer below, i.e. also with the Cr(110) bulk structure.

This whole density evolution is shown in Fig. 6.4. Here, each of the closed layer phases are represented by a point, while the adatom phases are represented by purple and

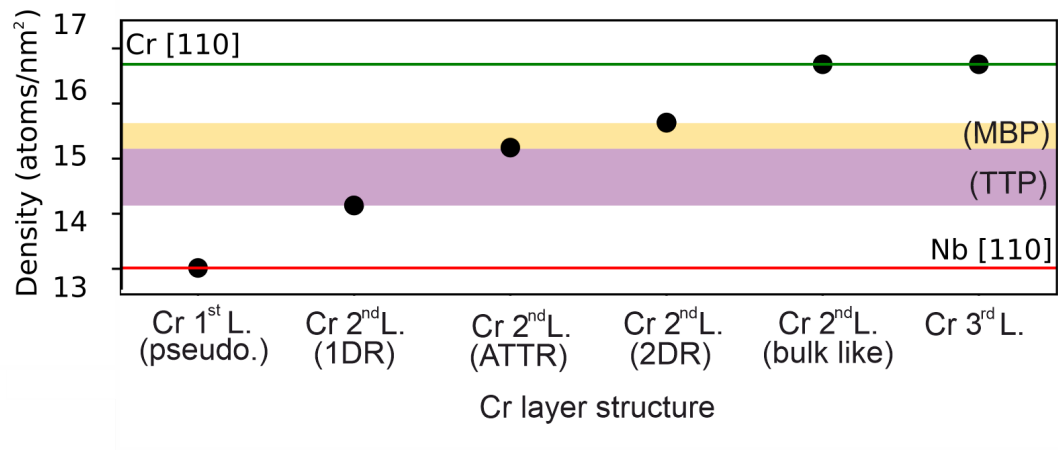


Figure 6.4: Density comparison for the different Cr layer structures. The different closed layer phases are represented by the points in the graph and named below. The Nb(110) and Cr(110) densities are represented by a red and a green line respectively. The adatom phases bridging the gaps between the reconstructions are represented by the purple and orange bands.

orange bands in the regime they appear, bridging the space between points. In this representation it is clear how the evaporated Cr strives for reaching the Cr(110) bulk density with each different structural phase until it finally reaches it in the second layer once the third layer grows on top.

7 Summary and outlook

"It is good to have an end to journey toward; but it is the journey that matters, in the end."

— Ursula K. Le Guin, *The left hand of darkness*

AFM materials exhibit a wide range of complex and interesting physical properties, many of them useful for the development of new spintronic technologies. In this thesis, two AFM ultra-thin layer systems have been investigated via SP-STM and STS. One of them keeps its magnetic properties despite of a structural phase change, while the other one displays a completely different set of features when its structure changes. These findings highlight how the structure can protect, enhance, or dismiss magnetic properties of a system and with them other more exotic features such as superconductivity.

The first of these systems is the monolayer of Mn on Ir(111). This system exhibits three different structural phases, two of which coexist in the submonolayer regime. The co-existing phases include a closed Mn film with an expanded Moiré-like reconstruction and a self-assembled, monodisperse Mn cluster phase. The addition of Mn atoms to the system increases the cluster phase density. Until this density is high enough, some clusters join the Moiré phase. If a complete monolayer of coverage is reached, a structural transition occurs, leading to the third phase: a pseudomorphic layer of Mn. The clusters have been characterized as trimers that can appear in five different configurations. It is possible to switch the configuration of the clusters unidirectionally from some types to others. The magnetic ground state of both the reconstructed Mn layer and the pseudomorphic one is the frustrated Néel state contained in the plane of the surface. For the trimer phase no magnetism was detected; however, we propose a superparamagnetic ground state with thermal fluctuations between different Néel-state-like configurations.

The second studied system is Cr on Nb(110). The first Cr layer grows pseudomorphically on the Nb(110) and it exhibits a $c(2 \times 2)$ AFM ground state. STS measurements of this first layer show the presence of YSR bands inside the superconducting gap of the system. Comparison of these results with previous work ([5]) reveals the realization of a topological nodal point superconductor for the extended monolayer of Cr on Nb(110). Small first layer Cr patches (called worms) do not display the YSR states observed on the extended first Cr layer, i.e. they exhibit the same superconducting properties as the Nb. Theoretical calculations [88] indicate that the Cr is susceptible to quench its

magnetic moments, potentially leading to the observed non-magnetic Cr worms. One possible scenario is that a minimum threshold of Heisenberg exchange energy per atom is required to counteract these perturbations and stabilize the $c(2 \times 2)$ magnetic state, which is only achieved in extended Cr layers. The second layer of Cr on Nb(110) exhibits three different structural phases separated by two adatom phases between them. Each structural phase has a higher surface atom density than the previous one. None of these phases exhibit magnetic contrast via SP-STM, nor do they display YSR states inside the gap. It is suggested that the reconstructions act as perturbations that induce magnetic moment quenching, leading to the second Cr layer exhibiting the same superconducting properties as Nb and the first-layer Cr worms. Additional experiments are required to further characterize the Cr/Nb(110) system, particularly in three areas. First, lower temperature STS measurements of the superconducting gaps should be performed to improve the energy resolution. Second, SP-STM measurements with known tip polarization are needed to characterize the quantization axis of the Cr first layer's magnetic ground state. Finally SP-STM images of the worms and their surroundings inside and outside the superconducting regime could give information about the nature of the worms and the origin of the moment-quenching perturbations. In addition, the second Cr layer presents an opportunity to study TNPSC as a function of the structure due to its malleability.

"Acta est fabula, plaudite!"

— Gaius Julius Caesar Augustus

Bibliography

1. Spethmann, J. *et al.* Discovery of magnetic single-and triple-q states in Mn/Re (0001). *Physical Review Letters* **124**, 227203 (2020).
2. Okubo, T., Chung, S. & Kawamura, H. Multiple-q States and the Skyrmion Lattice of the Triangular-Lattice Heisenberg Antiferromagnet under Magnetic Fields. *Physical Review Letters* **108**, 017206 (2012).
3. Rodríguez-Sota, A. *et al.* Phase Coexistence of Mn Trimer Clusters and Antiferromagnetic Mn Islands on Ir (111). *ACS nano* **18**, 3699–3706 (2024).
4. Kawagoe, T. & Suga, S. Antiferromagnetic domain formation and spin frustration induced by adjacent paired screw dislocations in 10 monolayer-thick Cr (001) films. *Japanese Journal of Applied Physics* **62**, 045003 (2023).
5. Bazarnik, M. *et al.* Antiferromagnetism-driven two-dimensional topological nodal-point superconductivity. *Nature Communications* **14**, 614 (2023).
6. Brüning, R. *et al.* The Non-collinear Path to Topological Superconductivity. *arXiv preprint arXiv:2405.14673* (2024).
7. Wiesendanger, R. *Scanning probe microscopy and spectroscopy: methods and applications* (Cambridge university press, 1994).
8. Wolf, S. *et al.* Spintronics: a spin-based electronics vision for the future. *Science* **294**, 1488–1495 (2001).
9. Jungwirth, T., Marti, X., Wadley, P. & Wunderlich, J. Antiferromagnetic spintronics. *Nature nanotechnology* **11**, 231–241 (2016).
10. Baltz, V. *et al.* Antiferromagnetic spintronics. *Reviews of Modern Physics* **90**, 015005 (2018).
11. Jungwirth, T. *et al.* The multiple directions of antiferromagnetic spintronics. *Nature Physics* **14**, 200–203 (2018).
12. Huang, G.-Y. & Xu, H. Majorana fermions in topological-insulator nanowires: From single superconducting nanowires to Josephson junctions. *Physical Review B* **95**, 155420 (2017).
13. Gao, C., Wulfhekel, W. & Kirschner, J. Revealing the 120° Antiferromagnetic Néel Structure in Real Space: One Monolayer Mn on Ag (111). *Physical Review Letters* **101**, 267205 (2008).
14. Binnig, G. & Rohrer, H. Scanning tunneling microscopy. *Surface science* **126**, 236–244 (1983).

15. Binnig, G., Rohrer, H., Gerber, C. & Weibel, E. Surface studies by scanning tunneling microscopy. *Physical Review Letters* **49**, 57 (1982).
16. Bardeen, J. Tunnelling from a many-particle point of view. *Physical Review Letters* **6**, 57 (1961).
17. Tersoff, J. & Hamann, D. R. Theory of the scanning tunneling microscope. *Physical Review B* **31**, 805 (1985).
18. Wiesendanger, R., Güntherodt, H.-J., Güntherodt, G., Gambino, R. & Ruf, R. Observation of vacuum tunneling of spin-polarized electrons with the scanning tunneling microscope. *Physical Review Letters* **65**, 247 (1990).
19. Julliere, M. Tunneling between ferromagnetic films. *Physics letters A* **54**, 225–226 (1975).
20. Slonczewski, J. C. Conductance and exchange coupling of two ferromagnets separated by a tunneling barrier. *Physical Review B* **39**, 6995 (1989).
21. Blundell, S. *Magnetism in condensed matter* (2003).
22. Waśniowska, M., Schröder, S., Ferriani, P. & Heinze, S. Real space observation of spin frustration in Cr on a triangular lattice. *Phys. Rev. B* **82**, 012402 (1 July 2010).
23. Gao, C. L., Wulfhekel, W. & Kirschner, J. Revealing the 120° Antiferromagnetic Néel Structure in Real Space: One Monolayer Mn on Ag(111). *Phys. Rev. Lett.* **101**, 267205 (26 Dec. 2008).
24. Palacio-Morales, A., Kubetzka, A., von Bergmann, K. & Wiesendanger, R. Coupling of coexisting noncollinear spin states in the Fe monolayer on Re (0001). *Nano Letters* **16**, 6252–6256 (2016).
25. Getzlaff, M. *Fundamentals of magnetism* (Springer Science Business Media, 2007).
26. Munkres, J. R. *Topology: international edition* (Pearson Prentice Hall, 2000).
27. Thouless, D. J., Kohmoto, M., Nightingale, M. P. & den Nijs, M. Quantized Hall conductance in a two-dimensional periodic potential. *Physical Review Letters* **49**, 405 (1982).
28. Hasan, M. Z. & Kane, C. L. Colloquium: topological insulators. *Reviews of modern physics* **82**, 3045–3067 (2010).
29. Fu, L., Kane, C. L. & Mele, E. J. Topological insulators in three dimensions. *Physical Review Letters* **98**, 106803 (2007).
30. Qi, X.-L. & Zhang, S.-C. Topological insulators and superconductors. *Reviews of modern physics* **83**, 1057–1110 (2011).

31. Kitaev, A. Y. Unpaired Majorana fermions in quantum wires. *Physics-uspekhi* **44**, 131 (2001).
32. Nagaosa, N. & Tokura, Y. Topological properties and dynamics of magnetic skyrmions. *Nature nanotechnology* **8**, 899–911 (2013).
33. Akhmerov, A. *Topology in condensed matter: The Quantum dot* https://topocondmat.org/test/w1_topointro-0d.html.
34. Kitaev, A. *Periodic table for topological insulators and superconductors* in *AIP conference proceedings* **1134** (2009), 22–30.
35. Tinkham, M. *Introduction to superconductivity* (Courier Corporation, 2004).
36. Bardeen, J., Cooper, L. N. & Schrieffer, J. R. Theory of superconductivity. *Physical review* **108**, 1175 (1957).
37. Dynes, R. C., Narayanamurti, V. & Garno, J. P. Direct measurement of quasiparticle-lifetime broadening in a strong-coupled superconductor. *Physical Review Letters* **41**, 1509 (1978).
38. London, F. & London, H. The electromagnetic equations of the supraconductor. *Proceedings of the Royal Society of London. Series A-Mathematical and Physical Sciences* **149**, 71–88 (1935).
39. Ginzburg, V. L. On the theory of superconductivity. *Il Nuovo Cimento* (1955-1965) **2**, 1234–1250 (1955).
40. Abrikosov, A. A. On the magnetic properties of superconductors of the second group. *Soviet Physics-JETP* **5**, 1174–1182 (1957).
41. Prozorov, R. & Giannetta, R. W. Magnetic penetration depth in unconventional superconductors. *Superconductor Science and Technology* **19**, R41 (2006).
42. Larbalestier, D., Gurevich, A., Feldmann, D. M. & Polyanskii, A. High-T_c superconducting materials for electric power applications. *Nature* **414**, 368–377 (2001).
43. Kobayashi, S. & Sato, M. Topological superconductivity in Dirac semimetals. *Physical Review Letters* **115**, 187001 (2015).
44. Yu, L. Bound state in superconductors with paramagnetic impurities. *Acta Physica Sinica* **21**, 75 (1965).
45. Shiba, H. Classical spins in superconductors. *Progress of theoretical Physics* **40**, 435–451 (1968).
46. Rusinov, A. Theory of gapless superconductivity in alloys containing paramagnetic impurities. *Sov. Phys. JETP* **29**, 1101–1106 (1969).

47. Ji, S.-H. *et al.* High-resolution scanning tunneling spectroscopy of magnetic impurity induced bound states in the superconducting gap of Pb thin films. *Physical Review Letters* **100**, 226801 (2008).
48. Yazdani, A., Jones, B., Lutz, C., Crommie, M. & Eigler, D. Probing the local effects of magnetic impurities on superconductivity. *Science* **275**, 1767–1770 (1997).
49. Ruby, M., Peng, Y., von Oppen, F., Heinrich, B. W. & Franke, K. J. Orbital picture of yu-shiba-rusinov multiplets. *Physical Review Letters* **117**, 186801 (2016).
50. Choi, D.-J. *et al.* Mapping the orbital structure of impurity bound states in a superconductor. *Nature communications* **8**, 15175 (2017).
51. Zhang, G. *et al.* Yu-Shiba-Rusinov bands in ferromagnetic superconducting diamond. *Science Advances* **6**, eaaz2536 (2020).
52. Schneider, L. *et al.* Topological Shiba bands in artificial spin chains on superconductors. *Nature Physics* **17**, 943–948 (2021).
53. Schlenhoff, A., Krause, S., Herzog, G. & Wiesendanger, R. Bulk Cr tips with full spatial magnetic sensitivity for spin-polarized scanning tunneling microscopy. *Applied Physics Letters* **97** (2010).
54. Bode, M. Spin-polarized scanning tunnelling microscopy. *Reports on Progress in Physics* **66**, 523 (2003).
55. Homberg, J., Weismann, A., Markussen, T. & Berndt, R. Resonance-enhanced vibrational spectroscopy of molecules on a superconductor. *Physical Review Letters* **129**, 116801 (2022).
56. Odobesko, A. B. *et al.* Preparation and electronic properties of clean superconducting Nb (110) surfaces. *Physical Review B* **99**, 115437 (2019).
57. Dai, S., Xiang, Y. & Srolovitz, D. J. Twisted bilayer graphene: Moiré with a twist. *Nano letters* **16**, 5923–5927 (2016).
58. Escudero, F., Sinner, A., Zhan, Z., Pantaleón, P. A. & Guinea, F. Designing moiré patterns by strain. *Physical Review Research* **6**, 023203 (2024).
59. Kögl, M. *et al.* Moiré straintronics: a universal platform for reconfigurable quantum materials. *npj 2D Materials and Applications* **7**, 32 (2023).
60. Cooley, J. W. & Tukey, J. W. An algorithm for the machine calculation of complex Fourier series. *Mathematics of computation* **19**, 297–301 (1965).
61. Hardrat, B. *et al.* Complex magnetism of iron monolayers on hexagonal transition metal surfaces from first principles. *Physical Review B—Condensed Matter and Materials Physics* **79**, 094411 (2009).

62. Arthur, J. R. Molecular beam epitaxy. *Surface science* **500**, 189–217 (2002).
63. Herman, M. A. & Sitter, H. *Molecular beam epitaxy: fundamentals and current status* (Springer Science & Business Media, 2012).
64. Durston, P., Schmidt, J., Palmer, R. & Wilcoxon, J. Scanning tunneling microscopy of ordered coated cluster layers on graphite. *Applied physics letters* **71**, 2940–2942 (1997).
65. Li, J.-L. *et al.* Spontaneous assembly of perfectly ordered identical-size nanocluster arrays. *Physical Review Letters* **88**, 066101 (2002).
66. Wang, Y., Saranin, A., Zotov, A., Lai, M. & Chang, H. Random and ordered arrays of surface magic clusters. *International Reviews in Physical Chemistry* **27**, 317–360 (2008).
67. Förster, D. F., Wehling, T. O., Schumacher, S., Rosch, A. & Michely, T. Phase coexistence of clusters and islands: europium on graphene. *New Journal of Physics* **14**, 023022 (2012).
68. Henry, C. R. 2D-arrays of nanoparticles as model catalysts. *Catalysis Letters* **145**, 731–749 (2015).
69. Jena, P. & Sun, Q. Super atomic clusters: design rules and potential for building blocks of materials. *Chemical reviews* **118**, 5755–5870 (2018).
70. Varykhalov, A. *et al.* Ir (111) surface state with giant Rashba splitting persists under graphene in air. *Physical Review Letters* **108**, 066804 (2012).
71. Pietzsch, O., Kubetzka, A., Bode, M. & Wiesendanger, R. Spin-polarized scanning tunneling spectroscopy of nanoscale cobalt islands on Cu (111). *Physical Review Letters* **92**, 057202 (2004).
72. Von Bergmann, K. *et al.* Complex magnetism of the Fe monolayer on Ir (111). *New Journal of Physics* **9**, 396 (2007).
73. Spethmann, J., Vedmedenko, E. Y., Wiesendanger, R., Kubetzka, A. & von Bergmann, K. Zero-field skyrmionic states and in-field edge-skyrmions induced by boundary tuning. *Communications Physics* **5**, 19 (2022).
74. Bode, M., Pietzsch, O., Kubetzka, A. & Wiesendanger, R. Shape-dependent thermal switching behavior of superparamagnetic nanoislands. *Physical review letters* **92**, 067201 (2004).
75. Prada, E. *et al.* From Andreev to Majorana bound states in hybrid superconductor–semiconductor nanowires. *Nature Reviews Physics* **2**, 575–594 (2020).
76. Beenakker, C. Search for Majorana fermions in superconductors. *Annu. Rev. Condens. Matter Phys.* **4**, 113–136 (2013).

-
77. Nadj-Perge, S., Drozdov, I. K., Bernevig, B. A. & Yazdani, A. Proposal for realizing Majorana fermions in chains of magnetic atoms on a superconductor. *Physical Review B—Condensed Matter and Materials Physics* **88**, 020407 (2013).
 78. Li, J. *et al.* Two-dimensional chiral topological superconductivity in Shiba lattices. *Nature Communications* **7**, 12297 (2016).
 79. Mascot, E., Bedow, J., Graham, M., Rachel, S. & Morr, D. K. Topological superconductivity in skyrmion lattices. *npj Quantum Materials* **6**, 6 (2021).
 80. Brüning, R. *Topology of magnetism and superconductivity in non-collinear spin textures* (Universitaet Hamburg (Germany), 2024).
 81. Sato, M. Nodal structure of superconductors with time-reversal invariance and \mathbb{Z}_2 topological number. *Physical Review B—Condensed Matter and Materials Physics* **73**, 214502 (2006).
 82. Béni, B. Topologically stable gapless phases of time-reversal-invariant superconductors. *Physical Review B—Condensed Matter and Materials Physics* **81**, 134515 (2010).
 83. Schnyder, A. P. & Brydon, P. M. Topological surface states in nodal superconductors. *Journal of Physics: Condensed Matter* **27**, 243201 (2015).
 84. Zhu, G.-Y., Wang, Z. & Zhang, G.-M. Two-dimensional topological superconducting phases emerged from d-wave superconductors in proximity to antiferromagnets. *Europhysics Letters* **118**, 37004 (2017).
 85. Nayak, A. K. *et al.* Evidence of topological boundary modes with topological nodal-point superconductivity. *Nature physics* **17**, 1413–1419 (2021).
 86. Meyer, S., Schmitt, M., Vogt, M., Bode, M. & Heinze, S. Dead magnetic layers at the interface: Moment quenching through hybridization and frustration. *Physical Review Research* **2**, 012075 (2020).
 87. Spethmann, J., Grünebohm, M., Wiesendanger, R., von Bergmann, K. & Kubetzka, A. Discovery and characterization of a new type of domain wall in a row-wise antiferromagnet. *Nature Communications* **12**, 3488 (2021).
 88. Drevelow Tim, U. o. K. Private communication. (2025).
 89. Kurz, P., Bihlmayer, G., Hirai, K. & Blügel, S. Three-dimensional spin structure on a two-dimensional lattice: Mn/Cu (111). *Physical review letters* **86**, 1106 (2001).
 90. Lo Conte, R. *et al.* Coexistence of antiferromagnetism and superconductivity in Mn/Nb (110). *Physical Review B* **105**, L100406 (2022).

List of publications

"El que lee mucho y anda mucho, ve
y sabe mucho."

— Miguel de Cervantes, *El ingenioso
hidalgo Don Quijote de la Mancha*.

Articles

Phase Coexistence of Mn Trimer Clusters and Antiferromagnetic Mn Islands on Ir(111)

Arturo Rodríguez-Sota, Vishesh Saxena, Jonas Spethmann, Roland Wiesendanger, Roberto Lo Conte, André Kubetzka, Kirsten von Bergmann.

ACS Nano **18**, 3699-3706 (2024).

Strain-driven domain wall network with chiral junctions in an antiferromagnet

Vishesh Saxena, Mara Gutzeit, Arturo Rodríguez-Sota, Soumyajyoti Haldar, Felix Zahner, Roland Wiesendanger, André Kubetzka, Stefan Heinze, Kirsten von Bergmann.

arXiv preprint arXiv:2408.12580 (2024)

Contributed talks

Peculiar growth of Mn on Ir (111) investigated by SP-STM

Arturo Rodríguez-Sota, Vishesh Saxena, Jonas Spethmann, Roland Wiesendanger, Roberto Lo Conte, André Kubetzka, Kirsten von Bergmann.

DPG Spring meeting, Regensburg, 2022

Phase Coexistence of Mn Trimer Clusters and Antiferromagnetic Mn Islands on Ir(111)

Arturo Rodríguez-Sota, Vishesh Saxena, Jonas Spethmann, Roland Wiesendanger, Roberto Lo Conte, André Kubetzka, Kirsten von Bergmann.

2D-SPM, San Sebastian, 2024

A box of surprises: Mn/Ir(111) studied via SP-STM

Arturo Rodríguez-Sota, Vishesh Saxena, Jonas Spethmann, Roland Wiesendanger, Roberto Lo Conte, André Kubetzka, Kirsten von Bergmann.

Columbia University, New York (virtual), 2024

Invited talks

Peculiar growth of Mn on Ir (111) investigated by SP-STM

Arturo Rodríguez-Sota, Vishesh Saxena, Jonas Spethmann, Roland Wiesendanger, Roberto Lo Conte, André Kubetzka, Kirsten von Bergmann.

Martin Luther Universität Halle-Wittenberg, Halle (Saale), 2022

Peculiar growth of Mn on Ir (111) investigated by SP-STM

Arturo Rodríguez-Sota, Vishesh Saxena, Jonas Spethmann, Roland Wiesendanger, Roberto Lo Conte, André Kubetzka, Kirsten von Bergmann.

Max Planck Institute of Microstructure, Halle (Saale), 2023

Cr/Nb(110): Structure, magnetism and superconductivity studied by STM

Arturo Rodríguez-Sota, Felix Zahner, Roland Wiesendanger, André Kubetzka, Kirsten von Bergmann.

Spin & orbit, San Sebastian, 2025

Contributed posters

Magnetism and growth of a Mn monolayer on Ir (111) investigated by SP-STM

Arturo Rodríguez Sota, Vishesh Saxena, Jonas Spethmann, André Kubetzka, Roberto Lo Conte, Roland Wiesendanger, and Kirsten von Bergmann

JEMS, Warsaw, 2022

Different Antiferromagnetic States in Mn/Ir(111) studied by SP-STM

Arturo Rodríguez Sota, Vishesh Saxena, Jonas Spethmann, André Kubetzka, Roberto Lo Conte, Roland Wiesendanger, and Kirsten von Bergmann

Skymionic retreat, Annweiler am Trifels, 2022

Sub-monolayer Mn/Ir(111) studied by SP-STM

Arturo Rodríguez Sota, Vishesh Saxena, Jonas Spethmann, André Kubetzka, Roberto Lo Conte, Roland Wiesendanger, and Kirsten von Bergmann

ESM, Madrid, 2023

Sub-monolayer Mn/Ir(111) studied by SP-STM (Best poster prize award winner)

Arturo Rodríguez Sota, Vishesh Saxena, Jonas Spethmann, André Kubetzka, Roberto Lo Conte, Roland Wiesendanger, and Kirsten von Bergmann

Dutch SPM day, Groningen, 2024

Acknowledgements

"If I have seen further, it is by
standing on the shoulders of giants."

— Sir Isaac Newton

I have many people to thank for helping me become the one that I am now. I will be glad to thank you all in the order I met you, so we all can enjoy the trajectory of a life that you all have helped to shape. Thank you, my giants.

I will start thanking my parents for everything. Detailing the particular thanks would be too tedious and not make honor to their efforts.

Still, I would like to thank my mother for asking me the lesson so many times, always with all the love and care necessary. She was born a teacher (and a learner).

I would also like to thank my father for planting in my young mind the marvels of the universe, having always the proper answers to my very inquisitive questions. He was born a scientist (and a lover).

I will continue thanking my brother, for what we are and what we can be.

I thank María José, for showing me that it is possible (and magical) to leave our roots.

I thank Ana, for being an indefatigable receptor of Arturo's stories and a great companion in many of them.

I thank Loren, for so many nights of AoE II and durums escaping the world.

I thank Santos, for being. And with his existence, letting me be.

I thank Jose Antonio, for being a friend to my soul.

I thank Roberto, for showing me all the physics that matter. The rest are second order approximations.

I thank Ana for being someone to look upon while studying. For proving that you can be good while being the best.

I thank Celia for letting herself be, and showing me how to do it. It doesn't matter if it rains or hails. Celia prevails, and no one can extinguish her.

I thank Madrid because *de Madrí' al cielo, y un agujerito pa' verlo*.

I thank Guille, because we started together, and he made sure we also finished together.

I thank Aarón for those nights in which we made the other one know that he was loved. I thank him for every single one of his hugs every time we meet.

I thank Fidel for reminding me that being a scientist has a lot to do with love and care for others.

I thank Fer for being a real physicist and a real friend. Because when Fer says something, I know it is worth thinking through it.

I thank Jaime for being my voice of reason. For being lawful to himself and virtuous while so. For being my hero.

I thank Belén for the music she brings to my life. Sad, cozy, piercing, packed with emotions I didn't know I could have together.

I thank Vera for helping me understand what games my mind is playing on me. For all those calls when one of us was shivering.

I thank Inés because she is happy. And that reminds me what I want to be.

I thank Rubén for teaching me how to teach with the care and humanity that such a personal activity requires.

I thank Hamburg for showing me that *wir sind nicht aus Zucker*.

I thank Olga for being there when the first plane landed. For showing me that I had a friend in Hamburg before I could place the city in a map. And for being my personal Cosmo.

I thank Homero for being a *Diosa*, and for never letting me forget that I am one too. For every hug that made me feel more accepted than any word. And of course, for being my personal Wanda.

I thank Kirsten for all the patience that she has had with me. For her way of working, teaching and caring. For her smiles. I thank her because I could have never wished for a better PhD supervisor.

I thank Vishesh for being my companion in this adventure from the beginning. For being the hero I needed, but not the hero I deserve.

I thank André because of his seemingly indefatigable enthusiasm, capable of lifting my whole day. I thank him for the way he listens, the way he respects, and his sharpness.

I thank Roland Wiesendanger for his advices and his hard work running the immense complexities of this group.

I thank Roberto for never understanding (or wanting to understand) any of my points

during the lunch conversations. Also for believing in me from his picture every day.

I thank Jonas for taking a little first step to form a friendship. I thank him for all the support and guidance that he has given to me these last years, which is invaluable. I thank him for his patience and respect. *Oh! Jonas! There's one more thing I have to mention!... I love you :)*

I thank Jannis for bringing me to great plans every time I was in need of a great plan.

I thank Tim for being so relatable. For being a spark of light in a muddy world. For making me feel so comfortable with him.

I thank Felix for opening his heart a little for me. For his nervous laughs and his reliability.

I thank Arved because it is a pleasure to work with him. Because today is a good day if he comes to the lab.

I thank the whole coffee crew: Khai, Christian, Elena, Eva, Harim, Jinkyung, Bianca and Jannik for discussing with so much passion so many incredibly fundamental topics. For example, and as an exercise for the reader: Is the sea soup?

I thank Alina for bringing peace and action to my life. I thank her for being herself and encouraging me to do so. For our super fun adventures! For being *dumm aber glücklich* with me. For knowing what is love.

I would like to finish by thanking the most important person in my life: Me.

Enhorabuena Arturo, estoy orgulloso de ti. Gracias por traernos por este camino, está siendo increíble. Estoy deseando ver a dónde nos lleva ahora. Te quiero mucho, nunca lo olvides.

"Murió el poeta lejos del hogar.
Le cubre el polvo de un país vecino.
Al alejarse, le vieron llorar.
Caminante, no hay camino,
se hace camino al andar"

— Joan Manuel Serrat, Cantares

Declaration on oath

I hereby declare and affirm that this doctoral dissertation is my own work and that I have not used any aids and sources other than those indicated.

If electronic resources based on generative artificial intelligence (gAI) were used in the course of writing this dissertation, I confirm that my own work was the main and value-adding contribution and that complete documentation of all resources used is available in accordance with good scientific practice. I am responsible for any erroneous or distorted content, incorrect references, violations of data protection and copyright law or plagiarism that may have been generated by the gAI.

Date: 19.05.2025 Signature of doctoral candidate: 